Abstract

WANG, LEI. Vibration Energy Harvesting by Magnetostrictive Material for Powering Wireless Sensors. (Under the direction of Dr. Fuh-Gwo Yuan).

Wireless Sensor Networks (WSN) have been increasingly applied to Structural Health Monitoring (SHM). For WSN to achieve full potential, self-powering these sensor nodes needs to be developed. A promising approach is to seamlessly integrate energy harvesting techniques from ambient vibrations with the sensor to form a self-powered node. The objective of this study is to develop a new magnetostrictive material (MsM) vibration energy harvester for powering WISP (Wireless Intelligent Sensor Platform) developed by North Carolina State University. Apart from piezoelectric materials which currently dominate in low frequency vibration harvesting, this new method provides an alternate scheme which overcomes the major drawbacks of piezoelectric vibration energy harvesters and can operate at a higher frequency range.

A new class of vibration energy harvester based on MsM, Metglas 2605SC, is deigned, developed, and tested. Compared to piezoelectric materials, Metglas 2605SC offers advantages including ultra-high energy conversion efficiency, high power density, longer life cycles, lack of depolarization, and high flexibility to survive in strong ambient vibrations. To enhance the energy conversion efficiency and shrink the size of the harvester, Metglas ribbons are transversely annealed by a strong magnetic field along their width direction to alleviate the need of bias magnetic field.

Governing equations of motion for the MsM harvesting device are derived by Hamilton's Principle in conjunction with normal mode superposition method based on Euler-Bernoulli beam theory. This approach indicates the MsM laminate wound with a

pick-up coil can be modeled as an electro-mechanical gyrator in series with an inductor. Then a generalized electrical-mechanical circuit mode is obtained. Such formulation is valid in a wide frequency range, not limited to below the fundamental natural frequency. In addition, the proposed model can be readily extended to a more practical case of a cantilever beam element with a tip mass. The model resulting in achievable output performances of the harvester powering a resistive load and charging a capacitive energy storage device, respectively, is quantitatively derived.

An energy harvesting circuit, which interfaces with a wireless sensor, accumulates the harvested energy into an ultracapacitor, is designed on a printed circuit board (PCB) with plane dimension 25mm×35mm. It mainly consists of a voltage quadrupler, a 3F ultracapacitor, and a smart regulator. The output DC voltage from the PCB can be adjusted within 2.0~5.5V which is compatible with most wireless sensor electronics. In experiments, a bimetallic cantilever beam method is developed to determine the piezomagnetic constant d from the measured λ-H curve. The maximum output power and power density on the resistor can reach 200 μW and 900 μW/cm^3, respectively. For a working prototype, the average power and power density during charging the ultracapacitor can achieve 576 μW and 606 μW/cm^3 respectively, which compete favorably with the piezoelectric vibration energy harvesters.

VIBRATION ENERGY HARVESTING BY MAGNETOSTRICTIVE MATERIAL FOR POWERING WIRELESS SENSORS

by

LEI WANG

A thesis submitted to the Graduate Faculty of
North Carolina State University
in partial fulfillment of the
requirements for the Degree of
Doctor of Philosophy

MECHANICAL ENGINEERING

Raleigh, NC

2007

APPROVED BY:

Dr. Kara J. Peters

Dr. Gregory D. Buckner

Dr. Gianluca Lazzi

Dr. Fuh-Gwo Yuan
Chair of Advisory Committee

Dedication

To my parents

and

my wife Zhenzi Liu

Biography

Lei Wang was born in Dongying, Shandong Province, the People's Republic of China on July 1, 1977. After completing his elementary and secondary education, he graduated from the No. 2 Middle School of Shengli Oil Field in 1995. He received his Bachelor of Science degree in Detecting Technology and Instruments from Nanjing University of Aeronautics and Astronautics in 1999. Since then he continued his graduate study in The Aeronautical Science Key Laboratory for Smart Materials and Structures at NUAA for three years. In 2004, he received his Master of Science degree in Aerospace Engineering at North Carolina State University. Then he has been working on his Doctor of Philosophy degree in Mechanical Engineering at NCSU. In the summer of 2006, he interned with ExxonMobil Upstream Research Company on microseismic wave modeling, signal processing and structural health monitoring for drilling wells.

Lei Wang is a member of American Society of Mechanical Engineering (ASME), American Institute of Aeronautics and Astronautics (AIAA), the Institute of Electrical and Electronics Engineers (IEEE), The Society of Photo-optical Instrumentation Engineers (SPIE), Sigma Gamma Tau National Honor Society of Aerospace Engineering (ΣΓΤ), and the Horner Society of Phi Kppa Phi (ΦΚΦ). He was the 2nd place winner of 2007 SPIE/ASME Best Student Paper/Presentation Award at San Diego, California.

Acknowledgements

I would like to thank Dr. Fuh-Gwo Yuan for suggesting the following work and serving as my graduate advisor over the past fives years. I appreciate very much his warm guidance and enthusiastic encouragement throughout the work. Especially, his insight into crossing-disciplines, keen apperception on academia trend, passion of exploring frontiers, and commitment to excellence impress me greatly.

I like to thank Dr. Kara Peters, Dr. Gregory D. Buckner and Dr. Gianluca Lazzi for providing help and advice in completing this research. Help from Dr. Shaorui Yang on theoretical modeling of the energy harvester is also gratefully acknowledged. Thanks also goes to Mr. Christopher Page for machining the art-like device for my design.

This research is supported by the National Science Foundation under grant No. CMS-0329878 and CMMI-0654233. I owe thanks to Dr. R. Hasegawa of Metglas®, Inc. for generously providing Metglas ribbons and valuable technical support. A special thanks goes to Advanced Circuits, Inc. for sponsoring the printed circuit board.

Thanks also goes to all the members in our research team of Smart Structures and Materials Laboratory including Dr. Jun Jin, Dr. Lei Liu, Dr. Saeed Nojovan, Mr. Nate Pringle, Mr. Feng Zhang, Mr. Shuntao Liu, and Mr. Angelo Cristobal for their care and help. Besides, I would like to express my sincere thanks to all the people from whom I have received help and advice during my M.S. and Ph.D. programs at NCSU.

I should thank my father, mother, and brother. Without their considerable understanding and strong support, I could never reach this joyful moment. Above all, my deepest gratitude and love go to my wife, Zhenzi Liu.

Table of Contents

List of Tables viii

List of Figures ix

List of Symbols and Abbreviations xii

1 Introduction 1

1.1 Energy Harvesting Principles 2

1.1.1 Why energy harvesting? 2

1.1.2 Architecture of energy harvesting based wireless sensors 3

1.1.3 Materials for energy conversion 6

1.1.4 Energy storage 8

1.2 Summary of Potential Energy Sources 12

1.2.1 Solar energy 12

1.2.2 Thermal energy 13

1.2.3 Vibration energy 14

1.2.4 RF energy 15

1.3 Vibration Energy Harvesting Techniques 16

1.3.1 Electromagnetic energy harvesting 17

1.3.2 Electrostatic energy harvesting 18

1.3.3 Piezoelectric energy harvesting 20

1.3.4 Magnetostrictive energy harvesting 22

1.3.5 Comparison of different techniques 24

1.4 Objective and Scope 25

2 Principle of MsM 27
2.1 Materials Overview 27
2.1.1 Giant MsM 27
2.1.2 Metallic glass 30
2.2 Magnetostrictive Effects 33
2.2.1 Joule effect 35
2.2.2 Villari effect 35
2.2.3 Other magnetostrictive effects 36
2.3 Annealing Treatment 38
3 Modeling of MsM-based Energy Harvesting 41
3.1 Prototype of the MsM Harvesting Device 41
3.2 Linearized Material Constitutive Equation 42
3.3 Modeling the MsM Harvesting Device 45
3.3.1 Energy approach modeling of governing equations 45
3.3.2 Modal analysis of the cantilever beam element 51
3.3.3 Governing equations of the MsM harvesting device 54
3.3.4 Model extension for a cantilever beam with a tip mass 58
3.4 Power Analysis 64
3.4.1 Power analysis for a resistive load 64
3.4.2 Charging performance for a capacitive load 67
4 Experimental Studies 69
4.1 Joule Effect Measurement 69
4.2 Circuit Design 75

4.2.1 Voltage quadrupler 76
4.2.2 Smart voltage regulator 78
4.2.3 PCB design for energy harvesting circuit 80
4.3 Experimental Setup 82
4.4 Experimental Results 82
4.4.1 Powering a resistive load 82
4.4.2 Charging the ultracapacitor 85
5 Conclusions 88
5.1 Conclusions 88
5.2 Future Work 89
6 References 91
Appendix 106
A.1 Equivalent Circuit for the Coil Wound around the Metglas Laminate 107
A.2 Governing Equations of Piezoelectric Vibration Energy Harvester 109
A.3 List of Publications at NCSU 114

List of Tables

Table 1.1 Energy density and voltage of batteries 9

Table 1.2. Comparison of battery, standard, and ultra capacitors (NESSCAP Co., 2006). 11

Table 1.3 Summary of the comparison of the different type of mechanisms 24

Table 2.1 Magnetoelastic properties of some MsMs. Unless otherwise specified, all measurements where performed at room temperature (Dapino, 2004; Du Trâemolet de Lacheisserie, 1993; Meeks and Hill, 1983) 32

Table 2.2 Comparison of Metglas and PZT 33

Table 2.3 Summary of magnetostrictive effects 37

Table 3.1 Mode shape constants of λ_i and η_i for a cantilever beam 53

Table 4.1 Pin functions of MAX1795/1796/1797 79

Table 4.2 Electrical components on the PCB 81

List of Figures

Figure 1.1 Power consumption of common wireless sensor nodes at different modes..... 3

Figure 1.2 Architecture of an energy harvesting based wireless sensor 4

Figure 1.3 Power vs. energy characteristics of energy-storage devices (Kim, 2003) 10

Figure 1.4 Schematic of a typical electromagnetic harvester (Amirtharajah and Chandrakasan, 1998)..... 18

Figure 1.5 Schematic of a typical electrostatic harvester vibrating horizontally (Roundy *et al.*, 2004)..... 19

Figure 2.1 Commercial products of Terfenol-D in: (a) solids and (b) powders 28

Figure 2.2 Commercial product of Metglas 2605SC ribbon (Metglas, 2007). 30

Figure 2.3 The motion of electron generates magnetic moment (Schwartz, 2002)..... 34

Figure 2.4 (a) spontaneous magnetism and random orientation of magnetic moments without external field (b) the alignment of moments under an external magnetic field (Du Trâemolet de Lacheisserie, 1993) 34

Figure 2.5 Illustrations of magnetic moments in unannealed and transverse field annealed Metgals ribbon: (a) unannealed ribbon with external load (b) unannealed ribbon under axial strain load; (c)annealed ribbon without external load; (d) annealed ribbon under axial load..... 38

Figure 2.6 Relative coupling coefficient of Metglas 2605SC, $k(T_a)/k(389°C)$, versus annealing temperature, T_a (Modzelewski *et al.*, 1981)..... 39

Figure 3.1 (a) Prototype of MsM energy harvesting device, (b) MsM layer (Metglas 2065SC) and laminate 42

Figure 3.2 (a) Geometry of the beam element in side view, (b) equivalent 1-DOF mass-spring-damper element model..... 45
Figure 3.3 Equivalent circuit model of the MsM harvesting device 50
Figure 3.4 A generalized four-terminal, two-port system for a vibration energy harvester ... 51
Figure 3.4 First five mode shapes of a cantilever beam..... 54
Figure 3.5 Uniform cantilever beam with a tip mass 58
Figure 3.6 First five mode shapes of a cantilever beam with different tip-to-beam mass ratios 62
Figure 3.7 Effect of tip-to-beam mass ratio, M_0/M, on the structural natural frequencies..... 63
Figure 3.8 The volt-ampere characteristic of the harvesting device..... 65
Figure 4.1 Bimetallic cantilever beam consisting of aluminum substrate and Metglas ribbon 70
Figure 4.2 Experimental set-up for measuring magnetostriction of Metglas 73
Figure 4.3 Experimental waveforms of the DC voltage and the deflection of the bimetallic beam..... 74
Figure 4.4 λ-H magnetostriction curves of annealed Metglas 2605SC..... 75
Figure 4.5 Energy harvesting circuit 75
Figure 4.6 Voltage multiplication: (a) doubler; (b) quadrupler 77
Figure 4.7 AC input voltage, output voltages from doubler and quadrupler simulated by PSpice. 78
Figure 4.8 Pin configuration of step-up DC-DC converter MAX1795/1796/1797..... 79
Figure 4.9 Actual PCB of the MsM harvesting circuit..... 81
Figure 4.10 Experimental set-up..... 82

Figure 4.11 Comparison of theoretical and experimental results on output voltage under 58.1 Hz and 1g acceleration 84
Figure 4.12 Comparison of theoretical and experimental results on output power under 58.1 Hz and 1g acceleration 84
Figure 4.13 Tip displacement of the MsM harvester, AC voltage from pick-up coil and DC output from the voltage quadrupler 86
Figure 4.14 Experimental results of the charging/discharging of the ultracapacitor and output performance of the smart voltage regulator 87
Figure A.1 Top view of Metglas laminate wound by pick-up coil..... 107
Figure A.2 Equivalent circuit model of the piezoelectric harvester..... 113

List of Symbols and Abbreviations

Greek Symbols

α , β	Coefficients in Raleigh damping matrix **C**
δ	Variation operator
$\mathcal{E}$	Internal energy
ε	Mechanical strain
$\boldsymbol{\phi}$	Modal vector
ϕ_i	The i^{th} normal mode shape function
φ	The electrical potential
η_i , λ_i	Coefficients in the i^{th} normal mode shape function
λ	Magnetostriction strain
μ^T	Permeability of MsM under constant stress
ρ	Mass density
σ	Mechanical stress
ω	Angular frequency
ω_i	Natural frequency associated with the i^{th} mode
$\boldsymbol{\Theta}$	Effective electromechanical transformer coefficient vector
ζ	Damping ratio
ψ_j	Electrical potential distribution function

Roman Symbols

B	Magnetic flux density
b	Width of the beam element
$\mathbf{C}$	Raleigh damping matrix
C	External capacitive load
c^E	Young's modulus of PZT under constant electrical field
C_p	Equivalent capacitor of piezoelectric harvester
d, d^*, e, e^*	Piezomagnetic coefficients of MsM
EI	Equivalent weighted area moment inertia of the substrate and MsM laminate
E^H	Young's modulus of MsM at constant magnetic field intensity
$\mathbf{F}$	Effect forcing vector due to the base excitation
$\boldsymbol{f}$	External point force vector
$\mathbf{G}$	Effective electromechanical gyrator coefficient vector
G	Element in effective electromechanical gyrator coefficient vector
H	Magnetic field intensity
h	Distance between centroidal axis to neutral axis
I	Second moment of area
i	Electrical current in time domain
J	Mass moment of inertia
$\mathbf{K}$	Effective modal stiffness matrix
K	Element in effective modal stiffness matrix
k	Coupling coefficient
k_g	Global coupling coefficient of the MsM harvesting device
L	Effective inductance of the pick-up coil with the MsM laminate

l	Length
$\mathbf{M}$	Effective modal stiffness matrix
M	Element in effective modal mass matrix
m	Mass per unit length
N	Number of coil turns
N_f	Number of external forces
N_r	Number of normal vibration modes
R	External resistive load
$\mathbf{r}$	Generalized coordinate vector
r	Generalized coordinate
s	Laplace variable
s^H	Elastic compliance under constant magnetic field
T	Kinetic energy
T_c	Curie temperature
t	Time variable
t_M	Thickness of the Metglas laminate
t_s	Thickness of the substrate
t_p	Thickness of the piezoelectric layer
$\mathbf{u}$	Displacement vector
U	Strain energy
v	Electrical voltage in time domain
W	External work
W_e	Internal electrical energy

W_M	Internal magnetic energy
w	Transverse displacement of the beam element
w_B	Transverse displacement of the base vibration
x, y, z	Cartesian coordinates
Z_m	Mechanical impedance of the MsM harvesting device

Subscripts

e	Related to electrical energy
i	The i^{th} normal mode
M	Related to magnetic energy, or MsM
m	Related to mechanical energy
o	Related to tip mass
p	Related to piezoelectric harvester
s	Related to substrate

Superscripts

T	Transpose operator
$'$	Derivative with respect to the axial position x

Caps

$\sim$	Frequency domain
$-$	Laplace domain
$\wedge$	Nondimensional parameter
$\cdot$	Derivative with respect to time

Abbreviations

AC	Alternating Current
DC	Direct Current
DOF	Degree of Freedom
DSP	Digital Signal Processing
EDLC	Electric Double Layer Capacitors
IC	Integrated Circuit
MEMS	Micro-Electro-Mechanical Systems
MsM	Magnetostrictive Material
ODE	Ordinary Differential Equation
PCB	Printed Circuit Board
PVDF	Polyvinylidene Fluoride
PZT	Lead Zirconate Titanate
RF	Radio Frequency
SHM	Structural Health Monitoring
SSDI	Synchronized Switching Damping on Inductor
SSHI	Synchronized Switch Harvesting on Inductor
VLSI	Very Large Scale Integration
WISP	Wireless Intelligent Sensor Platform
WSN	Wireless Sensor Networks

1 Introduction

Recent research and development efforts have led to an increasing deployment of wireless sensors and networks in the area of SHM. The WSN can remotely access the health status of structures, simplify the configuration by eliminating wire connection, and also significantly reduce the maintenance cost. Furthermore the advantages of WSN over traditional wired sensors include the sensor node communication, network scalability, and significantly increasing deployability of the sensors under a wide range of environmental conditions. Therefore, it holds the promise in the future for monitoring the structural integrity of aircrafts and infrastructures, measuring wheel pressure in automobile, tracking animal migration, and monitoring building securities, and *etc*.

Reliable power supply is becoming a critical issue in the applications of WSN. External chemical battery is not an appropriate solution because of its bulky size and limited life-span. For WSN to achieve full potential, self-powering these autonomous sensors needs to be developed depending on its specific application. Ultimate long-lasting solution should be independent of the limited energy available; a self-renewable energy source from the environment continually replenishing the energy consumed in the wireless sensor. This energy from the environment that is typically lost or dissipated in the environment is therefore recovered and used to power the wireless sensor, significantly extending the operational lifetime of the sensor or achieving nearly everlasting life of the sensor (Beeby *et al.*, 2006; Paradiso and Starner, 2005; Roundy *et al.*, 2004).

1.1 Energy Harvesting Principles

Energy harvesting, sometimes referred to as “power scavenging” or “energy extraction”, can be defined as “converting ambient energies such as vibration, temperature, light, RF energy, *etc*. to usable electrical energy by using energy conversion materials or structures, and subsequent storage of the electrical energy for powering electric devices”.

1.1.1 Why energy harvesting?

The lack of cables induces a constraint on power supply for each individual wireless sensor. Batteries wear out with time, thus regular replacement is an integral and inevitable part of maintenance. As the dense network is employed in structures, replacing batteries becomes a major time-consuming task that is uneconomical and unmanageable, ironically contradictory to the original objective of SHM. In addition, another constraint of battery-powered sensors is the bulky dimension of the batteries, typically occupying more than one-third of volume in the wireless sensor node.

Advances in low power Very Large Scale Integration (VLSI) design along with the low duty cycles of wireless sensors have reduced power requirements of 100 ~ 1000s of μW in MICA with projections into 10s of μW. Such trend enhances the feasibility of energy harvesting techniques. Figure 1.1 illustrates a summary on power consumption of common wireless sensor nodes at different operating modes, where the data is obtained from (BTnode Project, 2005). The maximum power for most wireless nodes is typically 200 mW, which strongly depends on sampling rate, transmission range and transmission speed of the sensor node.

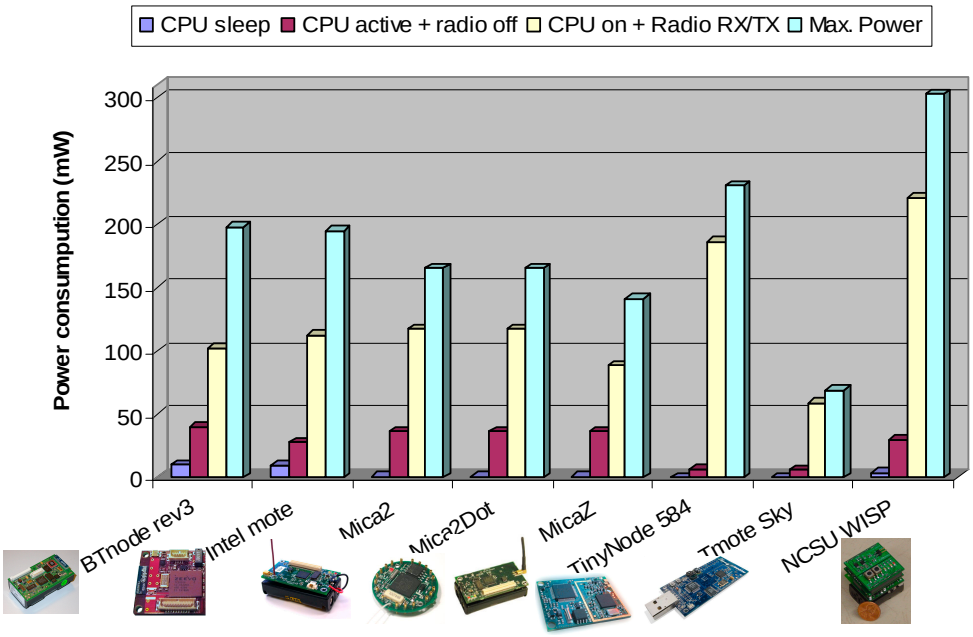

Figure 1.1 Power consumption of common wireless sensor nodes at different modes

1.1.2 Architecture of energy harvesting based wireless sensors

Compared to battery-powered sensors, the energy harvesting based sensors need an architecture to form energy harvesting modules. The module is composed of a harvesting device and an energy harvesting circuit. To better utilize the harvested energy, two additional submodules, power switching and power management modules, should be implemented with the wireless sensor node as shown Figure 1.2. The *harvesting device* generates usable electrical energy from environment. It can be implemented by two mechanisms: one is based on materials for energy conversion such as piezoelectric material, thermo-coupler, solar cell, *etc*; the other relies on structures for energy conversion such as electromagnetic harvesters and electrostatic harvesters. Those approaches will be further discussed in Session 1.3.

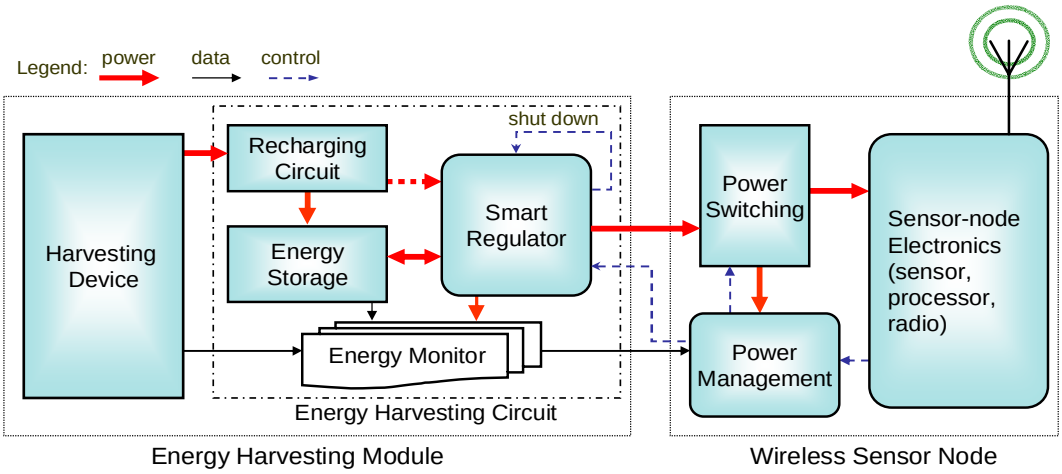

Figure 1.2 Architecture of an energy harvesting based wireless sensor

In the energy harvesting circuit board, the *Recharging circuit*, which is a condition circuit for energy storage device, has at least two functions. One is rectification converting AC voltage from harvesting device into DC voltage implemented by a diode bridge. Because of the forward voltage drop, one implicit requirement is that the amplitude of AC output voltage from the harvesting device must be higher than the voltage drop of the diodes. The other function is to match the charging profile of the energy storage device. For instance, a rechargeable battery must be charged by a voltage greater than its output, and an ultracapacitor may be broken if the charging voltage is higher than its rated voltage. Rechargeable batteries and ultracapacitors are commonly used as *energy storage devices*, which will be discussed in detail in Session 1.1.4.

The *smart regulator* is the key component with multiple functions in the energy harvesting circuit board. It resembles a valve with capability of adjusting the output power from the board to the wireless sensor node. The regulator can automatically shutdown when stored energy can not afford the consumption of the wireless sensor. To enhance the energy utilization for the wireless sensor, the smart regulator can bypass the

energy storage device and directly connect to the recharging circuit as long as the amount of power is sufficient to drive wireless sensors. Furthermore, the performance of smart regulator can be optimized through adjusting output voltage from control signals via power management module built in the wireless sensor.

The *energy monitor* tracks the available energy from environment, as well as the state of the energy storage device. Such data will be fed into the power management algorithms for learning the energy environment. As for circuit design, a voltage follower with low power consumption is suited for implementation.

In addition to usual wireless sensor components, two new submodules referred to as *power switching* and *power management* need to be integrated with the wireless sensor for establishing a compatible interface with energy harvester circuit board. The power from the harvester board, which is controlled by the power switching, drives all the electronics of the wireless sensor board. This submodule is useful for turning on or off various components as the amount of environmental availability varies. The *power management* submodule is a unique and essential component with at least two reasons. First, the environmental energy source highly varies. Unlike battery supply, which is simply characterized by the amount of residual energy and reliably available, the characterization of environmental energy is time-dependent and more complicated. Second, the environmental energy has the potential to be used permanently. The energy monitor records the characterization of environmental energy and sends to the power management submodule. With the built-in power management algorithm, the power management module can make decision to turn on or off the power switching and control the smart regulator.

1.1.3 Materials for energy conversion

Smart materials are a class of materials that can be used for energy conversion. In this subsection, piezoelectric and magnetostrictive materials are described. Piezoelectric materials are probably the best developed and best understood of all smart materials. They exhibit physical deformation in the presence of an electric field, or conversely, produce an electrical charge when mechanically deformed. The former phenomenon is called *inverse piezoelectric effect* for actuation; the latter is referred to as *direct piezoelectric effect* for sensing. Piezoelectric materials are widely available in many forms including single crystal (e.g. quartz), piezoceramic (e.g. lead zirconate titanate or PZT), thin film (e.g. sputtered zinc oxide), screen printable thick-films based on piezoceramic powder, and polymeric materials (e.g. polyvinylidene fluoride or PVDF).

Piezoelectric materials have anisotropy, thus, the properties of the material differ depending upon the direction of forces and orientation of the polarization and electrodes. The anisotropic properties are defined by a system of symbols and notations (IEEE Standard, 1991). According to piezoelectricity convention, the polarization direction is always along 3-axis. Two common operating modes are distinguished by the piezoelectric strain constant d_{ij} indicating generated electric field in *i*-axis under stressed in *j*-axis. Piezoelectric harvesters that rely on a compressive strain applied perpendicular to the electrodes exploit the d_{33} mode, while those that apply a transverse strain parallel to the electrodes utilize the d_{31} mode.

Piezoelectric materials have been playing an important role as a class of smart materials in SHM for many decades due to the following reasons. First piezoelectric materials can act as either sensor or actuator. Second, there is no bulky configuration and

it is easy to be integrated with host structures either by surface mount or embedded setup. Third, it is compatible with Micro-Electro-Mechanical Systems (MEMS) technique by deposition on the surface of silicon. However, the piezoelectric properties vary with age, stress, and temperature. The aging process is accelerated by the amount of stress applied to the ceramic and this should be considered in cyclically loaded energy harvesting applications. Temperature is also a limiting factor due to the Curie temperature. In addition, the application of stress can lower this Curie temperature. Because the piezoelectric effect in most piezoelectric materials results from artificially high-voltage poling procedure except for single crystals, the depolarization occurs for long time usage. Last, piezoelectric materials except for PVDF are very brittle and can not endure large strains.

Magnetostrictive materials (MsM) are a class of compounds which deform when exposed to magnetic field. Magnetostrictive effect or *Joule effect* pertains to the case when deformation is induced along the applied magnetic field direction. Such effect is often employed in actuator design. Due to the reciprocal nature of magnetoelastic coupling, MsM responds with a change in their magnetic state when subjected to deformation. This phenomenon, referred to as *Villari effect* or inverse magnetostrictive effect, provides a mechanism for sensing and potential for energy harvesting. In summary, the bi-directional coupling between the magnetic and mechanical states of an MsM provides a transduction mechanism that is used in both sensing and actuation.

Most MsMs such as cobalt, iron, nickel, ferrite, and *etc.* exhibit Vallari effect, but their magnitudes are too low to be of consequence in sensing of energy harvesting. Thanks to the development of giant MsMs, two commercially available materials make

energy harvesting possible: Terfenol-D ($Tb_{0.3}Dy_{0.7}Fe_{1.9\text{-}2}$) crystalline alloy (ETREMA Products, 2007) and Metglas 2605SC ($Fe_{81}B_{13.5}Si_{3.5}C_2$) metallic amorphous (Metglas, 2007).

Compared to piezoelectric materials, MsM is not poled because magnetostriction is an inherent material property. Thus, MsM does not degrade over time and permits almost unlimited vibrational cycles, ideal for long-term SHM with significantly enhanced reliability. Metglas is very flexible such that it could endure strong vibration. It has a high coupling coefficient (>0.9 in Metglas versus 0.3~0.4 in PZT d_{31} bending mode), efficiently translating vibration into electrical energy (Dapino, 2004). In addition, MsM possesses a wider temperature range, for instance Curie temperature 370°C for Metglas vs. 230°C for PZT-5H (Du Trâemolet de Lacheisserie, 1993).

1.1.4 Energy storage

Primary and rechargeable batteries are the major storage devices applied in WSN because of common availability in the marketplace; these batteries have fairly stable output voltage without complex power electronics. According to Table 1.1, zinc-air batteries have the highest energy density among common primary batteries but their life time is limited (Roundy *et al.*, 2004). Although lithium batteries have excellent energy density and longevity, they are the most expensive ones. Rechargeable batteries are normally used in electronic products such as cell phones, PDAs, and laptop computer; however another primary power source must be used to charge them. Since each type of storage devices has its own charging condition such as rated voltage and maximum current, *etc*., electronics are required to control the charging profile of the rechargeable

batteries. The longevity would be repeatedly reduced from overcharging and undercharging, such phenomenon is also called memory effect.

Table 1.1 Energy density and voltage of batteries

	Primary battery			Rechargeable battery		
	Zinc-air	Lithium	Alkaline	Lithium-ion	NiMHd	NiCd
Energy density (J/cm^3)	3780	2880	1200	1080	860	650
Voltage (V)	1.4	3.0~4.0	1.5	3.0	1.5	1.5

The recent development of electrochemical thin film rechargeable batteries holds the promise for energy storage of WSN (Arms *et al.*, 2005). They have similar structure as ultracapacitors and consist of anode, non-volatile electrolyte film as a separator, and cathode. Several layers can be connected in parallel and laminated together to increase capacity. Major advantages include no memory effect, small thickness 0.011~0.35mm, high flexibility, relatively high density (~1080 J/cm^3), superior cycle life (~70,000), low leakage (<1% per month), and commercial availability (Cymbet™, 2006; Infinite Power Solutions, 2006; Solicore, 2005). However, they need electronics to regulate the charging voltage in the same range of the open circuit voltage of thin film batteries. They are more expensive than the normal batteries and ultracapacitors.

The main difference between battery and capacitor is that a battery stores energy in chemical form, while a capacitor stores energy in an electric field. A capacitor holds the accumulated opposite charges apart to store energy in terms of electric potential energy, so there are no chemical changes of state or reaction. Thus capacitors can achieve instant charging and have higher power density than batteries; however energy density of standard capacitors is lower by 2~3 orders of magnitude than that of batteries.

Ultracapacitors also called as super-capacitors, Electric Double Layer Capacitors (EDLC), or pseudo-capacitors, have significantly higher energy density than standard capacitors, but retain many of the favorable characteristics of capacitors as well. Figure 1.3 shows a comparison of power vs. energy characteristics between different batteries, standard and ultra-capacitors (Kim, 2003).

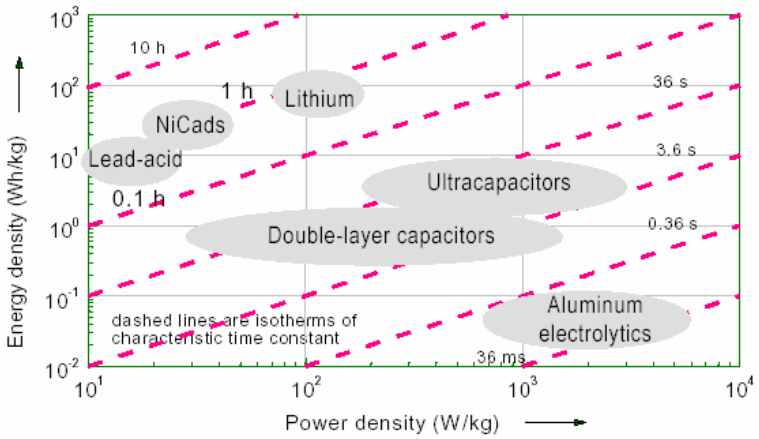

Figure 1.3 Power vs. energy characteristics of energy-storage devices (Kim, 2003)

An ultracapacitor consists of two metal-foiled electrodes coated with highly porous activated carbons, a paper separator that prevents the electrodes from touching each other and conducting current, and a liquid electrolyte. Unlike standard capacitors storing charges across a dielectric material, ultracapacitors store ionic charge in highly porous activated carbons. When the ultracapacitor is charged, positive and negative ions of the electrolyte are attracted to the activated carbons of two individual electrodes, respectively. Both kinds of ions migrate freely through the paper separator to get to the appropriately charged carbon, and they insinuate themselves into the porous carbons' many nooks and crannies. Therefore, this arrangement provides the two features for high

capacitance: electrodes with huge surface areas, and charges separated by very small distances. Note that the so-called capacitor is actually a pair of capacitors connecting in series with each other. Thus at each electrode there are two layers of charge, which is why ultracapacitors are also known as EDLC (Zorpette, 2005).

Ultracapacitors are now commercially available in the market (Maxwell Technologies, 2006; NEC Co., 2006; NESSCAP Co., 2006). They have been successfully applied as power supplies and energy storage devices in hybrid-electric vehicles, solar tiles, portable devices, and copier machines (Zorpette, 2005).

Table 1.2. Comparison of battery, standard, and ultra capacitors (NESSCAP Co., 2006).

Parameters	**Electrostatic Capacitor**	**Ultra-capacitor**	**Battery**
Discharge Time	10^{-6}~10^{-3}sec	1~30 sec	0.3~3 hrs
Charge Time	10^{-6}~10^{-3}sec	1~30 sec	1~5 hrs
Energy Density (Wh/kg)	< 0.1	1~10	20~100
Power Density (W/kg)	< 10,000	10,000	50~200
Charge / Discharge Efficiency	~ 1.0	~10	0.7~0.85
Cycle Life	Infinite	> 500,000	500~2,000

According to Figure 1.3 and Table 1.2, several advantages of ultracapacitors are summarized as: (1) instant charging within a few seconds; (2) at least one order of magnitude higher power density than batteries; (3) at least one order of magnitude higher charge/discharge efficiency than batteries; (4) semi-permanent life cycles; (5) compact size (10F in 1 cm^3, 20F in 2.4 cm^3); (6) cost-effective (20F costs less than $2.5). Although one disadvantage is lower energy density that that of batteries, it is still acceptable in the applications of energy harvesting for WSN because WSN has very low

duty cycle and the energy storage device can be replenished with time. Therefore, those features make ultracapacitors as alternate storage devices in place of rechargeable batteries in WSN.

1.2 Summary of Potential Energy Sources

The potential ambient sources for energy harvesting include solar, thermal gradient, vibration, and ambient RF energy.

1.2.1 Solar energy

Solar or other light energies can be converted into electrical power using solar cells, which are commercially mature and well characterized. The magnitude of energy generated varies from ~15 $\mu W/cm^2$ in noon-time sunlight to 10 $\mu W/cm^2$ in indoor, incandescent lighting (Bulusu and Jha, 2005). The output energy depends on the material used. For example, crystalline materials such as silicon and gallium arsenide have moderated absorption efficiency and high conversion efficiency about 15% ~ 30%; while thin film materials such as cadmium telluride have high absorption efficiency and lower conversion efficiency ($\leq$10%). The choice of materials also relies on its spectral response and the light source of interest (Bulusu and Jha, 2005).

A thin film solar cell to power MEMS electrostatic actuators was developed (Lee *et al.*, 1995). The array contained 100 single cells connected in series with total area of only 1 cm^2. Under incandescent lighting situations, an area of 1 cm^2 produced around 60 μW of power (van der Woerd *et al.*, 1998). A prototype solar powered directional hearing aid was integrated into a pair of spectacles. The current variation due to light intensity was overcome by a power converter integrated circuit (van der Woerd *et al.*, 1998).

In circuit design, the standard solar cell can be modeled as a voltage source in series with an internal resistor. A single solar cell has an open-circuit voltage of ~0.6 V, but panels with series and parallel combinations of such cells can generate any required voltage for circuit. Although the output voltage is fairly constant in the rated range, the current varies with light intensity. Solar power is still more expensive than conventional methods. Moreover, daily weather variations cause the greatest irregularity in the amount of irradiation that reaches the ground. The variation in the quantity of light energy that reaches the ground due to seasonal impact and daily weather makes reliable solar power virtually impossible in many geographic locations.

1.2.2 Thermal energy

Thermal gradients in the environment are directly converted to electrical energy through the Seebek or thermoelectric effect. Temperature differential between opposite segments of a conducting material results in heat flow and consequently charge flow. Thermoplies consisting of *n*- and *p*-type materials electrically jointed a the high-temperature junction are therefore constructed, allowing heat flow to carry the dominant charge carriers of each materials to the low temperature end, establishing in the process a voltage difference across the base electrodes.

A micro-thermoelectric harvester capable of producing 15 $\mu W/cm^2$ from a 10°C temperature differential was demonstrated by Stordeur and Stark (1997). The device provided relatively high output voltages of 100 mV/°C. A thermoelectric harvester by MEMS was also reported to offer 1.5 μW from a 10 °C temperature differential (Glosch *et al.*, 1999). Recently the thermoelectric harvester has become relatively mature. For example, Applied Digital Solutions Co. released a commercial product that could

generate 40 μW of power from a 5°C temperature differential using 0.5 cm^2 area with a thickness of a few millimeters. The output voltage was about 1 V (Pescovitz, 2002). Another more mature product could output 2.5 W power with 3 V in 8.4 cm^2 area cells from a 200°C temperature differential and it has been employed in several actual applications (Hi-Z Technology, 2005).

In brief, the generated voltage and power is proportional to the temperature differential and the Seebeck coefficient of the thermoelectric materials. Large thermal gradients are necessary to produce practical voltage and power level. Nevertheless, temperature differences greater than 10°C are rare in a micro-system, consequently producing low voltage and power level.

1.2.3 Vibration energy

Vibrations are available in many environments of interest including commercial buildings, highways, aircrafts, trains, industrial facilities (Roundy *et al.*, 2004). In general, frequency and acceleration are the key parameters to assess vibration sources. The higher those values, the larger provided power to the energy harvesters. Most of civil vibration sources such as truck engine, microwave oven, and kitchen blender have low frequency vibration up to 150 Hz and their accelerations are usually less than 0.5 g where 1g = 9.8 m/s^2 is gravitational acceleration. For long-span bridge, frequency and acceleration become even lower as < 0.1 Hz and 0.0001 ~ 0.1 g, respectively. On the contrary, there are significant ambient vibrations available on the aerospace structures: up to 1g between 300 Hz ~ 1 kHz (MIL-STD-810F, 2000).Thus one of motivations of this study is to propose new harvesting scheme for high frequency environments (up to 1 kHz) of

aircrafts and generate more power than the traditional harvesters operated in low frequency range (less than 200 Hz) of infrastructures.

1.2.4 RF energy

Another potential way of powering WSN is wireless energy transmission via electromagnetic waves for RF radiation. This concept utilizes two different RF energy sources: ambient and controlled RF sources. It has been shown that electronics could efficiently capture ambient RF radiation and convert them to useful electricity. Harrist (2004) tried to charge a cellular phone battery by collecting ambient 915 MHz RF energy. Although the battery could not be fully charged, he observed 4 mV/s charging rate. Only electronics with ultra-low power consumption may be driven by this approach, but the amount of harvested power is extremely low, typically in the range of a few μW.

Therefore the technique received the most attention is the controlled RF sources. One approach of controlled RF sources is based on RF link which consists of primary and secondary coils. When the two coils are close to each other and well center-aligned, the input AC power can be wirelessly transferred from primary coil to secondary coil via the inductive link. Yi *et al.* (2004) used RF link to drive a wireless temperature sensor for bearing monitoring. Several 10 mW could be transferred over 1~2 cm at 8.7 MHz frequency and the diameters of two coils were 7 cm and 6 cm, respectively. VanSchuylenbergh and Puers (1996) transferred 20 mW power for driving an implant strain sensor with transmission distance of 3~7 cm at 1 MHz RF. Vandevoorde and Puers (2001) demonstrated an inductive link with capability of transferring 20W power over a distance of 1cm. The major advantages include simple configuration, mature electronics, and adjustable transferred voltage on the secondary coil, but it has several limitations

such as short transmission distance <5 cm; variation of coupling efficiency on coil alignment, and bulky dimension due to two coils.

Another controlled microwave transmission, or so called beamed RF source, also holds the promise. A source antenna transmits microwaves across the atmosphere or space to a receiver, which can either be a typical antenna with rectifying circuitry to convert the microwaves to DC power or a rectenna (rectifying antenna) that integrates the technology to receive and directly convert the microwaves into DC power. With the usage of rectennas, efficiencies in the 50%–80% range for DC to DC conversion have been achieved. Significant testing has also been done across long distances and with kW power levels (Choi *et al.*, 2004). Briles *et al.* (2004) invented a RF wireless energy delivery system for underground gas or oil recovery pipes. The RF energy was generated on the surface and traveled through the conductive pipe, which acted as an antenna or a waveguide. The sensor module in the bottom of the pipe captured this energy and powered the electrical equipments. With a 100 W transmitted power from the surface, it was estimated that around 48 mW of instant power could be captured after traveling 1.6 km along the pipe. Mascarenas (2006) recently experimentally transferred 2.5mW power from X-band source horn antenna with 1W 10GHz radiation to a receiver horn antenna for driving piezo-sensor nodes over a distance of 0.61 m.

1.3 Vibration Energy Harvesting Techniques

Vibration energy harvesting techniques can be classified as electromagnetic, electrostatic, piezoelectric, and magnetostrictive approaches. The current status of investigations on the energy harvesting techniques is briefly reviewed as below. Four

common techniques will be discussed individually, and then a comparison table will be drawn to compare the features of different techniques.

1.3.1 Electromagnetic energy harvesting

As shown in Figure 1.4, the electromagnetic energy harvesting device employs relative motion of a conductor mass in a magnetic field, provided by a permanent magnet. Typically the mass is wound in a coil to form an inductor. Based on Faraday's Law, an AC voltage is induced by the relative motion between the mass and the pick-up coil. An analytical model was established (Williams *et al.* 2001; Williams and Yates 1996), and power densities of 1 μW at 70 Hz and 0.1 mW at 330 Hz were reported in experiments. Amirtharajah and Chandrakasan (1998) developed a more complicated harvesting device with a test chip, which integrated an ultra-low power controller regulating output voltage within 0.85~0.97 V and a low power sub-band filter digital signal processing (DSP) load circuit. The output power from the harvester could reach 400 μW. Recently an electromagnetic harvester was tested on a real automobile producing a peak power of 3.9 mW, however the average power was only 157 μW (Glynne-Jones *et al.*, 2004).

A micro-cantilever beam structure has been adopted to induce relative displacement between magnets and a coil bonded at free end of the beam (Torah, 2005). By using MEMS technique, the silicon beam thickness was only 50 μm. At a 0.06g acceleration and 58.5 Hz resonant frequency, its maximum power and power density could reach 10.8 μW and 900 $\mu W/cm^3$, respectively. Ching *et al.* (2002) discussed a micro-harvester fabricated on a PCB with total volume of ~$1cm^3$ comprising a laser-micromachined spiral copper spring and an NdFeB magnet and a coil. The peak-to peak

output voltage was up to 4.4V and maximum power could reach 830 μW when driven by a 200 μm displacement at its resonant frequency 110 Hz.

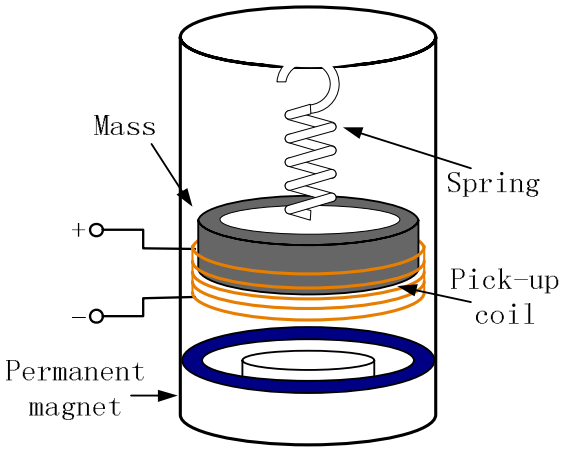

Figure 1.4 Schematic of a typical electromagnetic harvester (Amirtharajah and Chandrakasan, 1998)

The energy conversion mechanism is simple without the need of smart materials, but it has relatively larger volume because of the required permanent magnets and pick-up coil. Due to its inductive property, comparatively high output current levels are achievable at the expense of low voltage. Voltage multiplier may be a suitable solution to increase the voltage level. Wafer-scale systems, however, are quite difficult to achieve owing to the relatively poor properties of planar magnets, the limitations on the number of turns achievable with planar coils and the restricted amplitude of vibration.

1.3.2 Electrostatic energy harvesting

The electrostatic energy harvesting relies on the changing capacitance of vibration-dependant varactors, or variable capacitors whose electrodes are moveable to

each other and separated by a dielectric to form a capacitor as shown in Figure 1.5. By initially placing charge on the electrodes and moving the electrodes apart, mechanical motion can be converted into electrical energy (Roundy *et al.*, 2004). Energy density of the harvester can be increased by decreasing the capacitor spacing, facilitating miniaturization. The energy density, however, is also decreased by reducing the electrode surface area. Meninger *et al.* (2001) gave a good explanation of the merits of both charge and voltage constrained conversion. In theory slightly more power could be produced from a voltage constrained system. Furthermore, the electrostatic energy harvesting device attained power density of 0.23 $\mu W/cm^3$ at a vibration of 2.5 kHz. Roundy *et al.* (2004) optimized the electrostatic harvester and improved the output power density up to 110 $\mu W/cm^3$ at 120 Hz vibration.

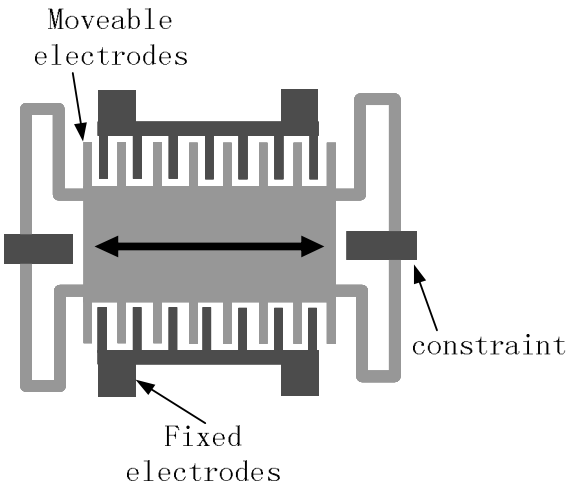

Figure 1.5 Schematic of a typical electrostatic harvester vibrating horizontally (Roundy *et al.*, 2004)

The electrostatic energy harvesting does not require smart materials and is feasibly integrated with MEMS by relatively mature silicon micro-machining techniques.

Due to capacitive-based device, it generates relative high voltage of 2~10 V and results in a limited current-supplying capacity (Roundy *et al.*, 2004). However, electrostatic harvesting requires an external voltage or charge source for initialization. Furthermore, mechanical constraints on the moving electrodes are indispensable to avoid electrode shorting.

1.3.3 Piezoelectric energy harvesting

The piezoelectric-based approach converts the strain energy to electrical energy by direct piezoelectric effect. It is the most popular one among all these vibration-based methods because of reasonable electro-mechanical coupling coefficient, no bulky accessories (such as coil or permanent magnet), and feasibility of being deposited on substrates for MEMS applications.

Starner (1996) might be one of the first researchers realizing the potential of piezo-based energy harvesting and proposing possible storage methods. Umeda *et al.* (1996) tested the abilities of a circuit comprising a rectifier and a storage capacitor, when a steel ball impacted a plate bonded with PZT. Shortly after this publication, the first US patent on energy harvesting was issued for a means of storing the rectified energy from a piezoelectric device in a capacitor (Kimura, 1998). Kymissis *et al.* (1998); Shenck and Paradiso (2001) developed a piezoelectric system to harvest the energy during human walking and power a 12 bit RFID at 310 MHz. The peak output power from PZT bimorph utilizing d_{31} bending mode under heal was 8.3 mW and from PVDF stave under toes was 1.3 mW.

Elvin *et al.* (2001) excited a 3 Hz bending vibration of a simply-supported beam with a surface-attached PVDF film to generate electrical power and drive a telemetry

circuit. A switch was added to the circuit to automatically discharge and charge the storage capacitor, which produced the output voltage range of 0.8~1.1 V for a RF transmitter. Pfeifer *et al.* (2001) applied a similar simply-supported piezo-bimorph to drive a PIC16C71 microprocessor (rated to 2.5V and <40 μW) and a RFID tag operating 13.56 MHz. The peak power density of this device could be 98 $\mu W/cm^3$ and the peak voltage was on the order of 1.5 V under 1 Hz manual excitation.

To dynamically optimize the power transfer efficiency, an adaptive AC-DC rectifier with an output capacitor, rechargeable battery, and switch-mode DC-DC converter was introduced by Ottman *et al.* (2002). A power density of 196 $\mu W/cm^3$ was obtained. However, if the voltage produced by the piezo-harvester was less than 10 V, then power flow into the battery was reduced because of loses in the additional circuit components. Roundy and Wright (2004) derived an equivalent electrical-mechanical circuit model to analyze the cantilever type of piezoelectric harvester; the maximum output power through a 300 kΩ resistor reached 375 $\mu W/cm^3$ subjected to a vibration of 2.5 m/s^2 at 120 Hz. To further improve the output power, Gao and Cui (2005) employed the same theoretical model but optimized geometry of the beam element. The maximum output power density of a triangular beam could achieve 790 $\mu W/cm^3$ with 43.5 kΩ resistor under a vibration of $9m/s^2$ at 72 Hz; while the maximum output power density from a rectangular beam under the same scenario was 520 $\mu W/cm^3$.

Recently, a new method of piezoelectric vibration energy harvesting called "Synchronized Switch Harvesting on Inductor" (SSHI) was developed (Badel *et al.*, 2005; Lefeuvre *et al.*, 2005; Makihara *et al.*, 2006). It was developed from a popular method of vibration suppression referred to as "synchronized switching damping on inductor"

(SSDI). It adopted an electrical circuit containing an inductor and an electrical switch to maximize charge extraction from PZT, and could enhance the output power four times (Badel *et al.*, 2006b; Lefeuvre *et al.*, 2005) or even more (Badel *et al.*, 2006a).

In brief, piezoelectric vibration energy harvesting offers a straightforward and simple approach, whereby structural vibrations are directly converted into a voltage as output. There is no requirement for having complex geometries, external supply, and bulky accessories. Furthermore, its transduction principle is practically well suited to MEMS. However, most piezoelectric materials no matter ceramics or crystals are very brittle, and this harvesting approach is required to be strained directly. Other disadvantages such as depolarization and charge leakage also exist in PZT. Thus their mechanical and physical properties limit overall performance and life time. Although PVDF film is flexible, it has low coupling efficiency. Due to the capacitive property, this method is capable of producing relatively high output voltage at the cost of low electrical currents.

1.3.4 Magnetostrictive energy harvesting

MsM has been recently considered in applications of vibration energy harvesting. It utilizes Villari effect, where vibration induced strain of an MsM produces a change in the magnetization of the material. Upon dynamic or cyclic loading, this change in magnetization is converted into electrical energy using a pick-up coil or solenoid surrounding the magnetostrictive layer according to Faraday's law.

Staley and Flatau (2005) attempted to apply a Terfenol-D alloy in vibration energy harvesting. The Terfenol-D rod was operated in axial mode rather than flexural bending mode. It had bulky dimension because of 1000-turn pick-up coil and 1500-turn

DC actuation coil for generating bias magnetic field. The maximum output power was up to 45 μW at resonant frequency of 45 Hz, and the amplitude of AC output voltage was less than 0.35 V which was inapplicable to voltage rectification. Although new developed giant Galfenol was tested in experiments, the output performance was not significantly enhanced and still unlikely to output any DC voltage (Staley, 2005).

Due to the giant magnetostriction of Terfenol-D up to 2000μ , Terfenol-D has been used as a medium to provide large extensional strains in a PZT layer for energy harvesting. A thin PZT layer sandwiched by two Terfenol-D layers is placed under time-varying magnetic field. Since the outer Terfenol-D layers will induce higher strains than the traditional d_{31} bending mode in the PZT layer, the PZT layer will generate more charge. The time-varying magnetic field could be induced from ambient vibrations by a permanent magnet attached to either a cantilever beam or a spring. Huang *et al.* (2003) developed a Terfenol-D/PZT/Terfenol-D composite harvester could achieve 1.2 mW of power at resonant frequency of 30 Hz at acceleration of 5 m/s^2. They claimed that more than 10 mW could be harvested from a volume of 1 cm^3 laminate at 5 m/s^2 acceleration. Bayrashev *et al.* (2004) also fabricated a diameter of 0.5 mm thick PZT disc sandwiched between two Terfenol-D discs with thickness of 1.5mm. When the laminate was exposed to low frequency (<100 Hz) varying magnetic field, the output from PZT layer was found to be in a range of 10~80 μW.

Wang and Yuan (2006) first proposed the feasibility of using amorphous metallic glass Metglas 2605SC harvesting energy from ambient vibrations. They introduced an equivalent electrical-mechanical circuit model to analyze the output performance of the harvester, and optimized the configuration of bias magnets and output performance. The

max output power reached 200 μW. Lately they completed the system integration design and enhanced the output performance by utilizing transversely annealing treatment to Metglas (Wang and Yuan, 2007).

Compared to piezoelectric based harvesters, Metglas-based harvesters have higher coupling efficiency (>0.9), higher Curie temperature, higher flexibility to be integrated with curved structures, and no depolarization problem. It is suitable to work in hash and high frequency environments. However, it has relatively large dimension, which is hard to be integrated with MEMS, because of the pick-up coil and permanent magnets.

1.3.5 Comparison of different techniques

Table 1.3 summarizes and compares the common vibration energy harvesting techniques.

Table 1.3 Summary of the comparison of the different type of mechanisms

Type	Advantages	Disadvantages
Electromagnetic	• no need of smart material • no external voltage source	• bulky size: magnets and pick-up coil • difficult to integrate with MEMS • max voltage of 0.1V
Electrostatic	• no need of smart material • compatible with MEMS • voltages of 2~10V	• external voltage (or charge) source • mechanical constraints needed • capacitive
Piezoelectric	• no external voltage source • high voltages of 2~10V • compact configuration • compatible with MEMS • high coupling in single crystal (SiO_2)	• depolarization and aging problems • brittleness in PZT • poor coupling in piezo thin film (PVDF) • charge leakage • high output impedance
Magnetostrictive	• ultra-high coupling coefficient >0.9 • no depolarization problem • high flexibility • suited to high frequency vibration	• non-linear effect • pick-up coil • may need bias magnets • difficult to integrate with MEMS

1.4 Objective and Scope

The first objective of this study is to develop a new vibration energy harvester based MsM for powering a wireless sensor, WISP, developed by North Carolina State University (Liu, 2006). As mentioned in Session 1.3.3, almost all of the current energy harvesting techniques are based on piezoelectric materials and operated at low frequency, less than 100 Hz (Beeby *et al.*, 2006). The second objective is to provide an alternate scheme for energy harvesting which overcomes the drawbacks of piezo-based harvesters and operates at higher frequency range up to 1 kHz, available in the vibration in aircrafts.

In Chapter 2, the material background of MsMs is reviewed and the physics origin of magnetostriction is also discussed to illustrate not only the Joule and Villari effects, but other magnetostrictive effects as well. At last, the procedure of transverse field annealing for Metglas 2605SC are investigated to enhance magnetomechanical coupling and thus alleviate the need of bias magnetic field.

Chapter 3 proposes a prototype of the MsM vibration energy harvester. The advantages of utilizing MsM-based harvester over PZTs are emphasized. Then a linearized constitutive equation for MsM in material level is reviewed. To model the harvesting device in structure level, an energy approach in conjunction with normal mode superposition method based on Euler-Bernoulli beam theory is developed. In addition, the proposed model is also extended to a more practical case of a cantilever beam element with a tip mass. The model is valid over a wide frequency range not limited to below the fundamental frequency. At last, the model resulting in achievable output performances of the harvester powering a resistive load and charging a capacitive energy storage device, respectively, is quantitatively derived.

In Chapter 4, a bimetallic cantilever beam method is proposed to measure magnetostriction for thin ribbon types of Metglas 2605SC, and then the piezomagnetic constant of Metglas 2605SC is determined experimentally. An energy harvesting circuit, which powers a wireless sensor, stores harvested energy in an ultracapacitor, is designed on a PCB. The circuit consists of a voltage quadrupler, a 3F ultracapacitor, and a smart regulator. In experiments, the maximum output power on a resistive load and charging the ultracapacitor can achieve 200 μW and 576 μW, respectively.

Chapter 5 summarizes the contributions and conclusions of this study and also proposes some perspective topics for the future research.

2 Principle of MsM

In this chapter, the material background of MsMs is reviewed in detail. Meanwhile the advantages of using Metglas over PZT are stressed. The physics origin of magnetostriction is also discussed to illustrate the Joule and Villari effects, the latter being utilized in harvesting vibration energy. In addition, other magnetostrictive effects are introduced as well. At last, the background and procedure of transverse field annealing for Metglas 2605SC are investigated to enhance magnetomechanical coupling and alleviate the need of bias magnetic field.

2.1 Materials Overview

MsMs are a class of metallic compounds which deform when exposed to magnetic fields. These deformations are a manifestation of the magnetoelastic coupling and corresponding dependency of magnetic moment orientation with interatomic spacing. With the development of giant MsM and metallic glass in the last decade, MsM has been increasingly applied in a wide variety of smart structures and SHM systems as actuators and sensors utilizing Joule and Villari effects, respectively. However, only a few attempts to introduce MsMs in energy harvesting have been made recently (Huang *et al.*, 2003).

2.1.1 Giant MsM

All ferromagnetic materials exhibit magnetostriction; however, their magnitudes are too low to be of consequence. The first breakthrough in MsM occurred in the early 1960's when Clark and his fellow researchers at The Naval Ordnance Laboratory (NOL, now NSWC) discovered the largest-known magnetostriction in the rare-earth elements terbium and dysprosium at an extremely low temperature close to absolute zero. During

the next two decades, they found that this giant magnetostrictive behavior exists at room temperature in terbium–iron ($TbFe_2$) and the magnetic anisotropic compensated alloy $Tb_xDy_{1-x}Fe_{1.9}$ (or Terfenol-D where x = 0.3) for further temperature stability. This MsM was then referred to as GMM (Giant MsM) that produces magnetostriction of more than several thousands μ (Engdahl, 2000). GMMs are currently available in a variety of forms including thin films, powder composites, and monolithic solid samples as shown in Figure 2.1 (ETREMA Products, 2007).

(a) (b)

Figure 2.1 Commercial products of Terfenol-D in: (a) solids and (b) powders

GMMs have been mainly applied as actuators in smart structures, sonar transducers, hydrophones, and ultrasonic devices. The response speed of GMMs is very fast, in the order of μs. Meanwhile GMM actuators exhibit an excellent response in extremely low (or quasi-static) frequency range; however this frequency range is inapplicable to PZTs because of the charge leakage. GMMs can produce strain up to 2000 μ and sustain external loads as large as 500-600 MPa; while the PZTs only generate 100μ ~ 600μ strains and can not tolerate large external load due to brittleness of ceramics. Furthermore, low impedance of GMMs enables a low drive voltage for actuator applications, while PZTs requires high actuation voltage which is not applicable in

inflammable atmospheres. Although there are some drawbacks in GMMs including expensive material cost, rather poor corrosion resistance, heat generation by driving coil, and eddy currents at high frequency excitation, fairly stable and robust performance can be obtained by choosing driving conditions according to the applications to be used. In addition, bias coils or permanent magnets are needed to obtain linear and polarity response of GMM actuators, so they are more bulky than PZT actuators and incompatible with MEMS. Like PZTs, hysteresis also exists in GMM and should be taken into account when GMM actuators are employed into precision positioning devices. GMMs can be applied as dynamic sensors such as accelerometers, force sensors, position sensors, and non-contact torque sensors via Villari effect which converts dynamic mechanical energy into time-varying magnetic energy (Schwartz, 2002). Since a pick-up coil is required to convert the time-varying magnetization to electric signals based on Faraday's law, GMM-based sensors can not measure static displacement.

As discussed in Session 1.3.4, a few researchers have attempted to introduce Terfenol-D into vibration energy harvesting through two approaches. One is to directly use Terfenol-D as a material for energy convension; the other is to build Terfenol-D/PZT/Terfenol-D laminate in which Terfenol-D layers produce large strains onto the PZT layer by Joule magnetostriction effect and the PZT layer converts strain energy to electrical energy. According to current state of literature, the former approach is not applicable to actual WSN (Staley and Flatau, 2005). The second approach can be an alternate scheme of PZT-based energy harvesting. However, two coupling mechanisms and load transfer between interlayer would further reduce the conversion efficiency, this

approach is still facing the similar limitations of PZT-based harvesters (Bayrashev *et al.*, 2004).

2.1.2 Metallic glass

In 1978 Clark and his co-workers invented a second new class of MsM based on amorphous metal, which was obtained by rapid quenching of magnetic alloys consisting of iron, nickel, and cobalt together with one or more of the following elements: silicon, boron, and phosphorus (Hernando *et al.*, 1988; Savage and Spano, 1982). Since the crystallization is fully prevented by the rapid quenching, these alloys are known as metallic glass, or commercially referred to as Metglas, which are commonly produced in thin ribbon geometries as shown in Figure 2.2 (Metglas, 2007).

Figure 2.2 Commercial product of Metglas 2605SC ribbon (Metglas, 2007).

As compared with crystalline materials, atomic disorder somewhat reduces the value of the elastic constants, but the high homogeneity of metallic glass with neither grain boundaries nor dislocations or similar defects. Besides high tensile strength and excellent ductility, other good magnetic properties include high permeability, low coercivity, low eddy current and hysteresis losses due to amorphous state which

eliminates the magneto-crystalline anisotropy enhancing the facility of magnetization rotation. Two general expressions have been employed to describe the non-crystalline structure: *metallic glass* refers to non-crystalline metals produced by undercooling from the melt, while the term *amorphous metal* is used when they are obtained by atomic condensation. In both cases, the non-crystalline state corresponds to a thermodynamically metastable one, not only with respect to a crystal, but also it can be structurally relaxed towards more stable states when subjected to thermal treatments before crystallization occurs (Hernando *et al.*, 1988).

Because of fast magnetization reversal with minimal magnetic losses, Metglas is originally applied in transformers, motors, telecommunications equipments and pulse power devices. However, it has recently been discovered that certain of these alloys exhibits ultra-high coupling coefficients > 0.90 after suitable anneal with a strong magnetic field. This makes Metglas as a competitive candidate for sensing applications in which externally applied magnetic field or mechanical stress converts into inductance changes of a coil having the Metglas as core element; on the other hand, the coupling coefficient of unannealed (or as-quenched) Metglas, which is normally provided by manufacture, is only about 0.23 (Modzelewski *et al.*, 1981). The anneal treatment for Metglas will be further discussed in Session 2.3. In addition, it is feasible to deposit Metglas as a thin-film on a host structure to form an *in-situ* sensor by DC magnetron sputtering (Lu and Nathan, 1997), which is a compatible with MEMS applications.

To the author's best knowledge, Metglas has been routinely employed as power transformers and current transducers (Metglas, 2007); however its ultra-high magnetomechanical coupling for energy conversion has not been exploited for energy

harvesting applications. Table 2.1 lists nominal material properties of several MsMs. The linear magnetomechanical coupling coefficient k quantifies the ratio of input energy which is available as output energy. Other properties include the elastic modulus E, saturation induction B_s, Curie temperature T_c, relative permeability μ_r, density ρ, and saturation magnetostriction λ_s and piezomagnetic constant d.

Table 2.1 Magnetoelastic properties of some MsMs. Unless otherwise specified, all measurements where performed at room temperature (Dapino, 2004; Du Trâemolet de Lacheisserie, 1993; Meeks and Hill, 1983)

Material	Saturation magnetostriction λ_s ($\times 10^6$)	ρ (kg/m^3)	μ_r	B_s (T)	T_c (°C)	E (GPa)	d ($\times 10^{-9}$ m/A)	k
Fe	-9.3	7880	>1000	2.15	770	285		
Ni	-33	8900	600	0.61	358	210		0.31
Co	-62	8900		1.79	1120	210		
50%Co-50%Fe	58	8250		2.45	500			0.35
50%Ni-50%Fe	13			1.6	500			
$TbFe_2$	1735 polycristal 475, amorphous	9100		1.1	425, amorphous 711, polycristal	360		0.35
Tb	2000 (-196 °C)	8330			-48	55.7		
Dy	4000 (-196 °C)	856			-184	61.4		
Terfenol-D	2000	9250	3-10	1.0	380	25-35	5-15	0.7-0.8
$Tb_{0.6}Dy_{0.4}$	4000							
Metglas 2605SC	40	7320	$>4\times10^4$ (as-cast); 3×10^5 (anneal)	1.65	370	25-200	400	0.97

Table 2.2 Comparison of Metglas and PZT

Metglas	PZT
Inductive devices • low impedance • moderate voltage (less than 100V to 200V) at moderate currents(mA to A) for force output • negligible eddy currents and hysteresis	Capacitor devices • high impedance • voltage (on the order of 1000V) at low currents(μA) for force output • leakage current
Ultra-high coupling coefficient k >0.9	Relatively low coupling coefficient k = 0.3~0.4
magnetostriction strain up to 40 μ	strain capabilities (up to 100μ)
Inherent property, not degrade with time	Depolarization and aging problems
High flexibility	High brittleness
Fast response speed, 10^{-6}s	Fast response speed
Nonlinear behavior, hard to model	Moderately nonlinear behavior, easy to model
Pick-up coil is required DC magnetic bias may be needed	Simple configuration
Commercially mature	Commercially mature
Poor corrosion resistance	High corrosion resistance
Cost-effective	Low material cost

2.2 Magnetostrictive Effects

Magnetostrictive effects, including Joule and Villari effects, are inherent material properties of all ferromagnetic materials. The magnetic property of a material originates from the motion of electrons. In the internal structure of an atom, the electron revolves about the nucleus and spins by itself, which generates orbital magnetic moment and spin magnetic moment, respectively, as shown in Figure 2.3. The atomic magnetic moment is the superposition of orbital magnetic moment and spin magnetic moment. When the spin moment rotates to align with the external field *H*, the orbital moment rotates along with it and produces considerable lattice deformation.

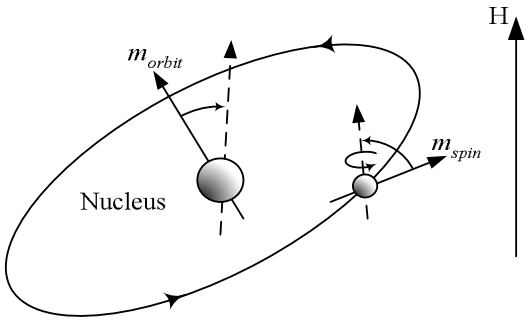

Figure 2.3 The motion of electron generates magnetic moment (Schwartz, 2002)

Magnetic domain is a small region contains 10^9~10^{15} atoms, in which the orientations of all atomic magnetic moments are the same because of the spontaneous magnetization. The ferromagnet does not exhibit magnetism on macroscopic view unless it has been magnetized by external magnetic field. This fact indicates (1) the orientation of spontaneous magnetization of each domain is random. (2) ferromagnet is composed of different magnetic domains interfaced by domain walls, as shown in Figure 2.4(a).

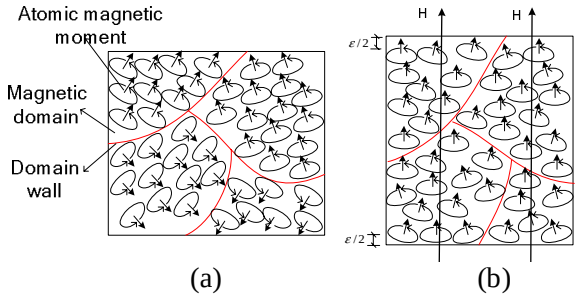

Figure 2.4 (a) spontaneous magnetism and random orientation of magnetic moments without external field (b) the alignment of moments under an external magnetic field (Du Trâemolet de Lacheisserie, 1993)

2.2.1 Joule effect

The Joule effect first discovered by J. P. Joule in 1840s refers to any change in the dimensions of a magnetic material due to a change in its magnetic state. Magnetostriction is mainly caused by spin-orbit coupling, which refers to a kind of interaction between the spin and orbital motions of each electron. This type of coupling is also responsible for crystal anisotropy. As illustrated in Figure 2.3, when an external magnetic field is applied and an electron spin tends to align with it, the orbit of that electron also inclines to reorient. Spin-orbit coupling is weak in most ferromagnetic materials, while such coupling in rare-earth metals is much stronger by about an order of magnitude. When a magnetic field rotates the spins and the orbital moment, considerable deformation, hence magnetostriction, is induced (Cullity, 1972). The stronger the field is, the more moments become aligned. When all the magnetic domains are perfectly aligned, saturation magnetostriction M_s is reached. During the course of the rotation of magnetic moment, the domain walls also disappear. In other words, the motion of domain walls and the rotation of magnetic moments result in the Joule effect, as illustrated in Figure 2.4 (b).

It is noted that if the magnetostriction is positive, the material elongates irrespective of the direction of rotation of the magnetic moments, and the transverse dimension is reduced such that the volume remains constant, for example Terfenol-D and Metglas. If the magnetostriction is negative, the sample length decreases and the diameter or thickness increases such as nickel, iron.

2.2.2 Villari effect

Due to the reciprocal nature, the changes in magnetization that an MsM undergoes when subjected to an applied uniaxial stress is called Villari effect, also known

as the magnetomechanical effect. This effect pertains to the transduction of energy from elastic to the magnetic state, and as such is the inverse of the Joule magnetostriction. Because the change in magnetic field can be further converted into electrical energy by Faraday's law, the Villari effect of MsMs can be applicable in energy harvesting with an indispensable pick-up coil.

2.2.3 Other magnetostrictive effects

Joule and Villari effects are two of several manifestations of a more general phenomenon, which is the coupling between magnetic and elastic regimes in an MsM. Other effects are briefly discussed as below and summarized in Table 2.3.

Wiedemann effect

A current-carrying MsM wire will generate a circular magnetic field in a plane perpendicular to the wire and the moments will align predominantly in the circumferential direction. When an axial magnetic field is applied, some of the moments align in a helical fashion generating a helical magnetic field. The twist observed in the wire is referred to as Wiedemann effect. The inverse Wiedemann effect, known as the Matteuci effect, is the change in axial magnetization of the current carrying wire when it is twisted (Du Trâemolet de Lacheisserie, 1993).

Magnetovolume effect

While the volume of an MsM remains virtually unchanged during normal operation, in certain extreme regimes the volume of the materials may change in response to magnetic field. This anomalous volume change is called the volume magnetostriction or Barret effect, which is most evident near the Curie temperature. However, the effect is negligible compared to other effects. For example, while the magnetostriction of nickel

rapidly reaches -35μ at only 10 kA/m, the fractional volume change is only 0.1μ at much stronger field of 80 kA/m (Dapino, 2004). The inverse of the Barret effect, the Nagaoka-Honda effect, is the change in magnetic state due to a volume change (Du Trâemolet de Lacheisserie, 1993).

ΔE effect

The elasticity of MsM comprises two separate but related attributes, namely the conventional stress-strain elasticity due to inter-atomic forces and the magnetoelastic contribution caused by the rotation of magnetic moments and ensuing strain which occurs when a stress is applied. This is known as the ΔE effect and is determined by $\Delta E = (E_s - E_0)/E_0$, where E_0 is the minimum elastic modulus E_s is the elastic modulus at magnetic saturation. Because the strain produced by magnetic moment rotation adds to the non-magnetic strain, the material becomes softer when the moments are free to rotate. Contrarily, the material becomes increasingly stiffer as saturation is approached and magnetic moment mobility decreases (Du Trâemolet de Lacheisserie, 1993).

Table 2.3 Summary of magnetostrictive effects

Direct effects	Inverse effects
Joule effect Change in sample dimensions in the direction of the applied field	**Villari effect** Change in magnetization caused by applied stress
Wiedemann effect Torque induced by helical anisotropy	**Matteuci effect** Helical anisotropy and e.m.f. induced by a torque
Magnetovolume effect Volume change due to magnetization, most evident near the Curie temperature	**Nagao-ka-Honda effect** Change in the magnetic state due to a change in the volume
***ΔE* effect** magnetoelastic contribution to magneto-crystalline anisotropy	Magnetically induced changes in the elasticity

2.3 Annealing Treatment

The value of magnetomechanical coupling depends upon the ease of rotation of the magnetization. In other words, a mainly rotational magnetization offers a large coupling. Therefore, induction of a homogeneous magnetic anisotropy is very important to maximize the magnetomechanical coupling of Metglas (Modzelewski *et al.*, 1981).

As-quenched, or unannealed, Metglas ribbons exhibit magnetically and mechanically isotropy. As illustrated in Figure 2.5(a) the magnetic moments are randomly oriented, so the magnetic anisotropy is trivial and easy axis is not well defined. When the unannealed ribbon is stressed along length direction as shown in Figure 2.5(b), the entirely rotation of magnetization is impossible to achieve. On the contrary, transverse field annealing in width direction preferentially orients the local easy anisotropy axes perpendicular to the long axis of the ribbon as shown in Figure 2.5(c). When subjected to the axial stress in length direction, the annealed ribbon produces an almost entirely rotational magnetization process as illustrated in Figure 2.5(d). This entirely rotational magnetization yields the ultra-high magnetomechanical coupling.

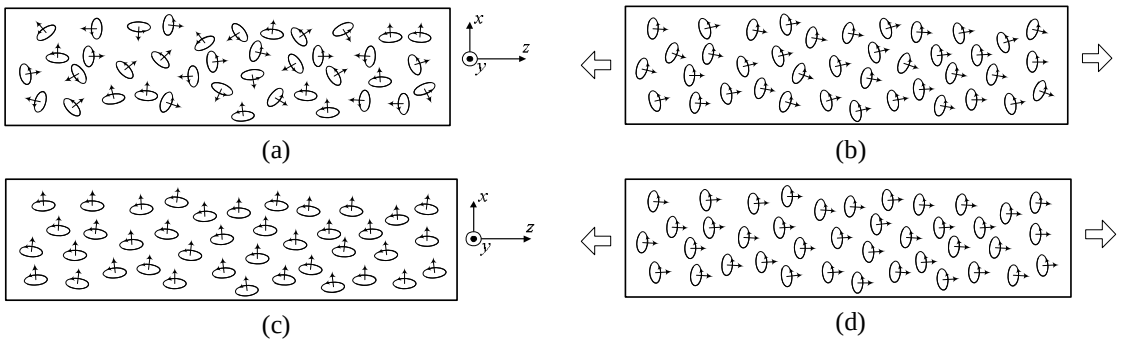

Figure 2.5 Illustrations of magnetic moments in unannealed and transverse field annealed Metgals ribbon: (a) unannealed ribbon with external load (b) unannealed ribbon under axial strain load; (c)annealed ribbon without external load; (d) annealed ribbon under axial load

According to Table 2.1, nickel has been considered as a material of choice for magnetomechanical transducers with a value of k = 0.31. Terfenol-D has k = 0.7, which compares very favorably with piezoelectric transducer materials (Dapino, 2004). Metglas 2605SC, amorphous metallic alloys, has shown k = 0.97 after annealing treatment under transverse field in the width direction, the largest value ever found (Hernando *et al.*, 1988). From Figure 2.6 the coupling coefficient of as-quenched Metglas 2605SC samples is about 0.23, that is, the transversely annealing can remarkably increase coupling coefficient of a raw Metglas 2605SC by a factor of four (Modzelewski *et al.*, 1981).

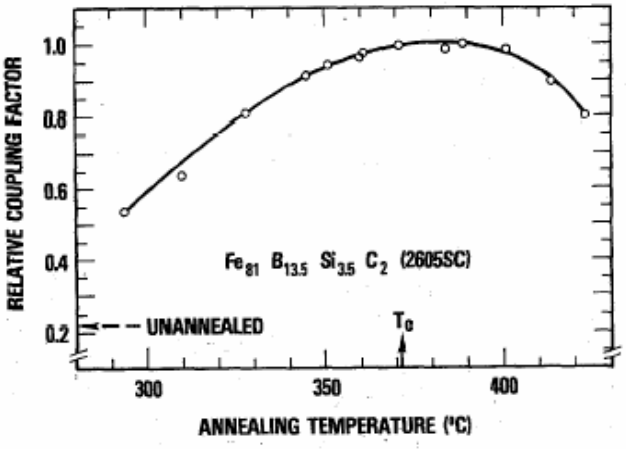

Figure 2.6 Relative coupling coefficient of Metglas 2605SC, $k(T_a)/k(389°C)$, versus annealing temperature, T_a (Modzelewski *et al.*, 1981)

The transverse field annealing process can be summarized as below (Meeks and Hill, 1983; Spano *et al.*, 1982):

(1) Place a Metglas 2605SC ribbon into a strong magnetic field, at least larger than 1000 Oe (typically 5000 Oe), which is perpendicular to the length of the ribbon but in the plane of the ribbon.

(2) Heat the ribbon for 10 minutes in a argon atmosphere at preselected annealing temperature T_a = 386°C~389°C, which is higher than its Curie temperature T_c = 370°C but still lower than its crystallization temperature 480°C (Modzelewski *et al.*, 1981). Therefore, after the annealing, the sample is still amorphous rather than crystalline. From Figure 2.6, it may be seen that the largest coupling factor occurs at T_a = 389°C just above its Curie temperature. It is worth noting that T_a is very critical and should be lower than crystallization temperature; otherwise the ribbon transits from amorphous to crystalline state. Accordingly an implicit requirement for annealing the Metglas ribbon to increase coupling coefficient is its Curie temperature must be lower than its crystallization temperatures.

(3) After 10 minutes of annealing in an argon atmosphere at the desired annealing temperature, the heating is turned off and the ribbon is allowed to cool to ambient with the magnetic field still applied (Meeks and Hill, 1983; Spano *et al.*, 1982).

In addition to high magnetomechanical coupling, the other major advantage of transverse field annealed Metglas is that it does not require external bias magnets, which are necessary in Terfenol-D based energy harvester (Staley, 2005), and can remarkably reduce the dimension of the MsM energy harvester.

3 Modeling of MsM-based Energy Harvesting

A prototype of the MsM harvesting device is proposed with Metglas 2605SC laminate bonded on a cantilever copper substrate and a pick-up coil. The advantages of utilizing MsM-based harvester over PZTs are emphasized. Then a linearized constitutive equation for MsM is reviewed. To model the harvesting device, governing equations in closed-form are developed via an energy approach in conjunction with normal mode superposition method based on Euler-Bernoulli beam theory. Then a generalized electrical-mechanical circuit mode is obtained correspondingly. In addition, the proposed model is also extended to a practical case of a cantilever beam element with a tip mass. The importance of this formulation is its validation over a wide frequency range up to any desirable high natural frequency. At last, the model resulting in achievable output performances of the harvester powering a resistive load and charging a capacitive energy storage device, respectively, is quantitatively derived.

3.1 Prototype of the MsM Harvesting Device

This study presents a new class of energy harvester module based on MsM. It has two units: a harvesting device comprising a giant MsM (Metglas 2605SC) bonded on a copper substrate and a pick-up coil as shown in Figure 3.1(a), and an energy harvesting circuit discussed in Session 4.2. Due to the thin thickness 18 μm of the standard Metglas 2605SC ribbon, several MsM ribbons are laminated as shown in Figure 3.1(b) to enhance energy harvesting capability. The MsM laminate utilizes Villari or sensing effect of magnetostriction, where vibration-induced strains caused by bending produces a change in the magnetization of the MsM laminate. Upon dynamic or cyclic loading, this change

in magnetization is converted into electrical energy using a pick-up coil surrounding the MsM laminate according to Faraday's law. Note that one drawback of another giant MsM Terfenol-D for energy harvesting is the requirement of bias magnetic field and this leads to bulky dimension. In this study, a strong transverse magnetic field is introduced to anneal Metglas such that it could alleviate the usage of bias magnetic field and reduce the harvester's footprint (Meeks and Hill, 1983; Modzelewski *et al.*, 1981).

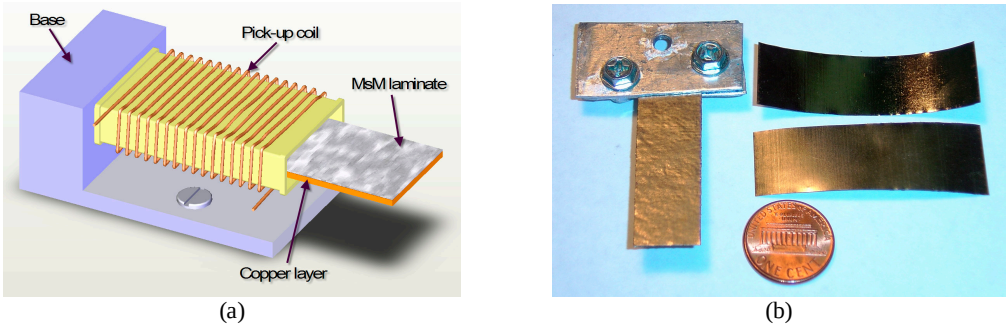

(a) (b)

Figure 3.1 (a) Prototype of MsM energy harvesting device, (b) MsM layer (Metglas 2065SC) and laminate

3.2 Linearized Material Constitutive Equation

The magnetic and mechanical behavior of magnetostriction with neglect of thermal effects are given in tensor expression

$$\varepsilon_{ij} = s^{H}_{ijkl}\sigma_{kl} + d_{kij}H_k + m_{klij}H_kH_l \tag{3-1a}$$

$$B_j = d^{*}_{jkl}\sigma_{kl} + \mu^{T}_{jk}H_k \tag{3-1b}$$

where ε and σ are mechanical strain and stress, respectively; H and B are magnetic field intensity and flux density, repetitively; s^H is the elastic compliance under constant magnetic field, and μ^T is the permeability under constant stress.

The above nonlinear relation in one dimension can be linearized using two equations that are very similar to the two coupled equations which describe linearized uniaxial piezoelectric materials (IEEE Standard, 1991)

$$\begin{Bmatrix} \varepsilon \\ B \end{Bmatrix} = \begin{bmatrix} s^H & d \\ d^* & \mu^T \end{bmatrix} \begin{Bmatrix} \sigma \\ H \end{Bmatrix} \tag{3-2}$$

where the two magnetomechanical coefficients are defined experimentally by the following two equations, where subscripts σ and H refer to measurements at constant stress and constant applied magnetic field, respectively.

$$d = \left.\frac{\partial \varepsilon}{\partial H}\right|_{\sigma} \tag{3-3a}$$

$$d^* = \left.\frac{\partial B}{\partial \sigma}\right|_{H} \tag{3-3b}$$

For small strains, d and d^* can be considered to be equal.

The constitutive Eq. (3-2) can be rearranged as (IEEE Standard, 1991)

$$\begin{Bmatrix} \sigma \\ B \end{Bmatrix} = \begin{bmatrix} E^H & -e \\ e^* & \mu^S \end{bmatrix} \begin{Bmatrix} \varepsilon \\ H \end{Bmatrix} \tag{3-4}$$

where E^H is the Young's modulus of the MsM under constant magnetic field, μ^S is the permeability under constant strain, constants e and e^* are defined as

$$e = E^H d \tag{3-5a}$$

$$e^* = E^H d^* \tag{3-5b}$$

Based on the coordinate convention (Du Trâemolet de Lacheisserie, 1993; Savage and Spano, 1982), axes *3* and *1* are in the length and width direction of the laminate, respectively. When the material bent in *2*-axis, both induced axial strain and

magnetization are in *3*-axis. Accordingly, the Metglas laminate operates in "*33*" mode. In the following, the subscript *33* is omitted (Du Trâemolet de Lacheisserie, 1993; Engdahl, 2000).

Assuming linearized relationship between *B*, *H*, ε, and σ, the internal energy is given by

$$\mathcal{E} = \frac{1}{2}\varepsilon\sigma + \frac{1}{2}HB \tag{3-6}$$

Substitution of ε and *B* into Eq. (3-6) by Eq. (3-2) yields

$$\begin{aligned}\mathcal{E} &= \frac{1}{2}\sigma s^H \sigma + \frac{1}{2}\sigma dH + \frac{1}{2}Hd^*\sigma + \frac{1}{2}H\mu^T H \\ &= \mathcal{E}_m + \mathcal{E}_{\mathrm{mM}} + \mathcal{E}_{\mathrm{Mm}} + \mathcal{E}_M = \mathcal{E}_{\mathrm{m}} + 2\mathcal{E}_{\mathrm{mM}} + \mathcal{E}_M\end{aligned} \tag{3-7}$$

where subscripts *m*, *M* and *mM* (or *Mm*) indicate the mechanical, magnetic, mutual magnetoelastic energy, respectively.

An important figure of merit for MsM is the material coupling coefficient, *k*, which is defined as the ratio of the mutual magnetoelastic energy to the geometric mean of the mechanical and magnetic energy (Du Trâemolet de Lacheisserie, 1993; Engdahl, 2000)

$$k = \frac{\mathcal{E}_{\mathrm{mM}}}{\sqrt{\mathcal{E}_{\mathrm{m}}\mathcal{E}_{\mathrm{M}}}} \tag{3-8}$$

Inserting Eq. (3-7) into Eq. (3-8) gives

$$k^2 = \frac{d^2}{\mu^T s^H} \tag{3-9}$$

3.3 Modeling the MsM Harvesting Device

The constitutive Eq. (3-2) should be extended to model macro-behavior of the MsM harvesting device with a cantilever unimorph and a pick-up coil. Figure 3.2(a) shows the geometry of the beam element of MsM harvesting device in side view, where *x* and *z* are in horizontal and transverse directions, respectively. The beam configuration is a unimorph structure. Assume both copper substrate and Metglas laminate have the same width *b* and length *l*. An equivalent 1-DOF mass-spring-damper approximation model as shown in Figure 3.2(b) was derived based on average strain (Roundy *et al.*, 2004). However this model is only valid in frequency range up to the fundamental natural frequency. Since the MsM harvesting device may vibrate at higher frequencies, rigorous models need to be investigated.

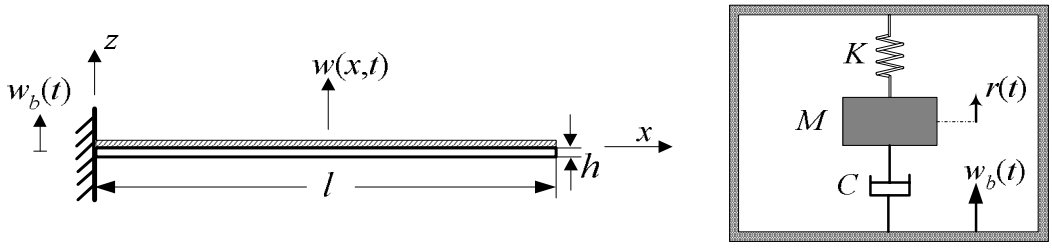

(a) (b)

Figure 3.2 (a) Geometry of the beam element in side view, (b) equivalent 1-DOF mass-spring-damper element model

3.3.1 Energy approach modeling of governing equations

In this study, an energy approach based on Hamilton's Principle is developed to model the vibration of the harvesting device. To derive equations of motion, the principle of virtual work based on Hamilton's Principle can be written as

$$\int_{t_1}^{t_2}[\delta(T-U+W_M)+\delta W]dt=0 \tag{3-10}$$

where all variations vanish over any time interval from t_1 to t_2; the kinetic energy T, strain energy U , and magnetic energy W_M are defined as

$$T=\frac{1}{2}\int_{V_s}\rho_s\dot{\mathbf{u}}^T\dot{\mathbf{u}}dV_s+\frac{1}{2}\int_{V_M}\rho_M\dot{\mathbf{u}}^T\dot{\mathbf{u}}dV_M \tag{3-11a}$$

$$U=\frac{1}{2}\int_{V_s}\boldsymbol{\varepsilon}^T\boldsymbol{\sigma}dV_s+\frac{1}{2}\int_{V_M}\boldsymbol{\varepsilon}^T\boldsymbol{\sigma}dV_M \tag{3-11b}$$

$$W_M=\frac{1}{2}\int_{V_M}BHdV_M \tag{3-11c}$$

where superscript T denotes transpose operation, subscripts s and M indicate the copper substrate and MsM layer, respectively. The mechanical displacement is $\mathbf{u}(x,t)$, and ρ is the mass density. Since Eq. (3-10) does not include electrical energy on an external electrical load, the formulation derived here is in short circuit condition for the pick-up coil.

Considering N_f discretely applied external point forces $\mathbf{f}_k(t)$, at positions x_k, the external work W is given by

$$\delta W=\sum_{k=1}^{N_f}\delta\mathbf{u}_k\mathbf{f}_k(t) \tag{3-12}$$

With consideration of the above definitions and the constitutive relations of Eq. (3-4), Eq. (3-10) is rewritten as

$$\begin{aligned}\int_{t_1}^{t_2}\Big[&\int_{V_s}\rho_s\delta\dot{\mathbf{u}}^T\dot{\mathbf{u}}dV_s+\int_{V_M}\rho_M\delta\dot{\mathbf{u}}^T\dot{\mathbf{u}}dV_M-\int_{V_s}E_s\delta\boldsymbol{\varepsilon}^T\boldsymbol{\varepsilon}dV_s-\int_{V_M}E^H\delta\boldsymbol{\varepsilon}^T\boldsymbol{\varepsilon}dV_M\\&+\int_{V_M}e\delta\boldsymbol{\varepsilon}^THdV_M+\int_{V_M}e^*\delta H\boldsymbol{\varepsilon}dV_M+\int_{V_M}\mu^S\delta HHdV_M+\sum_{k=1}^{N_f}\delta\mathbf{u}_k\mathbf{f}_k(t)\Big]dt=0\end{aligned} \tag{3-13}$$

where E_s is the Young's modulus of the copper substrate.

In order to deduce the equations of motion from Eq. (3-13), some assumptions must be made. The first assumption follows the Rayleigh-Ritz procedure, which states the displacement of a structure can be expressed as the superposition of N_r individual modes $\phi_i(x)$, multiplied by a generalized coordinate $r_i(t)$ (Inman, 2001; Thomson and Dahleh, 1998). Second, only the transverse displacement is considered for a beam in bending and the mode shape $\phi_i(x)$ is a function of the axial position $x \in [0, l]$, such that $\mathbf{u}(x,t)=(0, 0, w(x,t))$. Third, the base excitation is assumed to be only in the transverse direction, i.e. *z*-axis. The last assumption is to apply the Euler-Bernoulli beam theory that the bending strain ε in the beam is a product of the distance from the neutral axis and the second derivative of displacement with respect to the position along the beam.

$$w(x,t) = \sum_{r=1}^{N_r} \phi_r(x) r_r(t) = \boldsymbol{\phi}(x)\mathbf{r}(t) \tag{3-14}$$

$$\varepsilon = -z \frac{\partial^2 w(x,t)}{\partial x^2} = -z\boldsymbol{\phi}''(x)\mathbf{r}(t) \tag{3-15}$$

where $\boldsymbol{\phi} = [\phi_1(x), \cdots, \phi_{N_r}(x)]$ is modal vector, $\mathbf{r}(t) = [r_1(t), \cdots, r_{N_r}(t)]^T$ is generalized coordinate vector, and the prime indicates the derivative to the axial position *x*. Thus, the cantilever beam structure with infinite DOFs is approximated by finite N_r modes.

With an assumption of long solenoid coil and neglecting fringing effects, magnetic field intensity *H* can be expressed by Ampere's law

$$H = \frac{N}{l} i \tag{3-16}$$

where *N* is the number of turns of the pick-up coil, and *i* is the induced current.

The above assumptions can simplify Eq. (3-13) in terms of modal matrices to obtain the equations of motion as follows

$$\mathbf{M}\ddot{\mathbf{r}} + \mathbf{K}\mathbf{r} + \mathbf{G}i = \sum_{k=1}^{N_f} \boldsymbol{\phi}^T(x_k) f_k(t) \tag{3-17a}$$

$$\mathbf{G}^T\mathbf{r} - Li = 0 \tag{3-17b}$$

where modal mass matrix **M** and modal stiffness matrix **K** are given respectively by

$$\mathbf{M} = \int_{V_s} \rho_s \boldsymbol{\phi}^T(x)\boldsymbol{\phi}(x)dV_s + \int_{V_M} \rho_M \boldsymbol{\phi}^T(x)\boldsymbol{\phi}(x)dV_M \tag{3-18a}$$

$$\mathbf{K} = \int_{V_s} E_s \boldsymbol{\phi}''^T(x)\boldsymbol{\phi}''(x)z^2 dV_s + \int_{V_M} E^H \boldsymbol{\phi}''^T(x)\boldsymbol{\phi}''(x)z^2 dV_M \tag{3-18b}$$

$$\mathbf{G} = \frac{N d^* E^H A_M h_M}{l} \int_0^l \boldsymbol{\phi}''^T(x)dx \tag{3-18c}$$

$$L = \frac{\mu^S N^2 A_M}{l} \tag{3-18d}$$

where $A_M = bt_M$ is the cross sectional area of the Metglas laminate, h_M is the distance from the centroid of the Metglas laminate to the neutral axis, and L is the equivalent inductor associated with the coil wound around the Metglas laminate. Note that **G** is a function of mode shapes, but the inductor L is not.

Next step is to obtain the equivalent input force from vibration of the host structure, referred to as the base excitation. The cantilever beam is discretized into N_f elements of length $(\Delta x)_{N_f}$ and the local inertial load is applied on the kth element, or $f_k = -m_k(\Delta x)_k \ddot{w}_B$ where m_k is the element mass per length and w_B is the known base displacement. This leads to N_f point loads. The loading is summated over all the elements. With the limit of $(\Delta x)_k \rightarrow dx$, the summation reduces to the integral over the beam length. For simplicity it has been assumed that the beam is uniform in the axial direction such that $m(x)=m$=const. Substitution of the forcing function into the right hand side of Eq. (3-17a) yields a so called modal forcing vector **F** (duToit *et al.*, 2005)

$$\mathbf{F} = -\ddot{w}_B \int_0^l m(x)\boldsymbol{\phi}^T(x)dx = -\ddot{w}_B m \int_0^l \boldsymbol{\phi}^T(x)dx \tag{3-19}$$

where $m = (\rho_s t_s + \rho_M t_M)b$, t_s and t_M are the thickness of the substrate and the Metglas laminate, respectively.

Mechanical damping is added through a Rayleigh damping matrix **C** to Eq. (3-17a). When multiple modes are considered, a proportional damping scheme is employed here to ensure uncoupling of the equations in the modal analysis (Inman, 2001; Thomson and Dahleh, 1998)

$$\mathbf{C} = \alpha\mathbf{M} + \beta\mathbf{K} \tag{3-20}$$

where α and β are determined from:

$$\zeta_i = \frac{\alpha}{2\omega_i} + \frac{\beta\omega_i}{2}, \quad i = 1, 2, \cdots, N_r \tag{3-21}$$

where ζ_i is the damping ratio experimentally obtained from the frequency response of the beam structure. After experimental measuring the damping ratios of the first two modes, α and β can be solved from the above equations (Inman, 2001).

Inserting Eqs. (3-19) and (3-20) back into Eq. (3-17a), the equations of motion for the harvesting device with electrical-mechanical coupling can be rearranged as

$$\mathbf{M}\ddot{\mathbf{r}} + \mathbf{C}\dot{\mathbf{r}} + \mathbf{K}\mathbf{r} + \mathbf{G}i = \mathbf{F} \tag{3-22a}$$

$$v = \mathbf{G}^T\dot{\mathbf{r}} - L\dot{i} \tag{3-22b}$$

where **M**, **K**, and **C** are $N_r \times N_r$ square matrices, **G**, **F**, and **r** are $N_r \times 1$ column vectors, and v is the output voltage on an electrical load. In addition, **G** can be considered as an equivalent gyrator converting mechanical velocity $\dot{\mathbf{r}}(t)$ into voltage.

From Eqs. (3-22), a generalized electromechanical circuit model is established for analyzing the MsM harvesting device as shown in Figure 3.3, where mechanical modal

matrices **M, C**, and $\mathbf{K}^{-1}$ are equivalent to electrical inductor, resistor, and capacitor, respectively, excitation force **F** and generalized velocity $\dot{\mathbf{r}}$ are equivalent to the voltage and current, respectively.

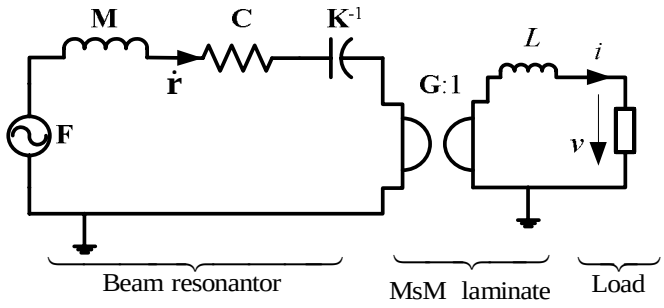

Figure 3.3 Equivalent circuit model of the MsM harvesting device

Eq. (3-17b) is derived from the short-circuit condition of the pick-up coil, thus the right hand side is zero. While Eq. (3-22b) includes a practical case of the pick-up coil driving an electrical load with output voltage of *v*. Eq.(3-22b) can be also derived by another approach described in Appendix A.1, which reveals its physical significance. Thus the behavior of the coil wound around the Metglas laminate along its length direction can be described as an electro-mechanical gyrator in series with the inductor. Due to the equivalent inductance *L*, MsM-based harvesters can be considered as inductive devices with characteristic of high current and low voltage. On the contrary, piezo-based harvesters are modeled as an electro-mechanical transformer in parallel connected with an equivalent capacitor, thus piezo-based harvesters can be regarded as capacitive devices with high voltage and low current (Elvin *et al.*, 2001; Roundy and Wright, 2004).

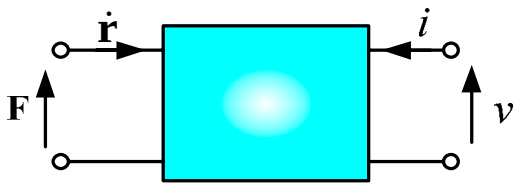

Figure 3.4 A generalized four-terminal, two-port system for a vibration energy harvester

According to Figure 3.3 or Eqs. (3-22), a vibration energy harvesting device, not limited to the MsM harvester, can be considered as a generalized four-terminal, two-port system as shown in Figure 3.4. Generally speaking, the forcing vector **F** and electrical voltage v are viewed as *across variables*, which change magnitude between port terminals. While the velocity $\dot{\mathbf{r}}$ and electrical current i can be regarded as *through variables*, which flow through the port. The coupling term **G** in Eq. (3-22a), converting the through variables into across variables (e.g. $\dot{\mathbf{r}}$ and i into v and **F**, respectively), is analog to an electromechanical gyrator. In addition, Appendix A.2 will discuss the equivalent circuit model of piezoelectric vibration energy harvesters based on the Hamilton's Principle.

3.3.2 Modal analysis of the cantilever beam element

For the cantilever beam, the displacement mode shape function ϕ_i is solved under the assumption of Euler-Bernoulli beam theory (Thomson and Dahleh, 1998)

$$EI\frac{\partial^4 w}{\partial x^4} + m\frac{\partial^2 w}{\partial t^2} = 0 \tag{3-23}$$

where EI is the equivalent weighted moment inertia of the substrate and Metglas laminate

$$EI = E_s(I_s + A_s h_s^2) + E^H(I_M + A_M h_M^2) \tag{3-24}$$

where subscripts *s* and *M* indicate the copper substrate and Metglas laminate respectively, *I* is area moment of inertia, *h* is the distance from the centroidal axis of each sub-beam to the neutral axis as follows

$$h_s = \frac{E_M t_M (t_M + t_s)}{2(E_M t_M + E_s t_s)} \tag{3-25a}$$

$$h_M = \frac{E_s t_s (t_M + t_s)}{2(E_M t_M + E_s t_s)} \tag{3-25b}$$

The solution of Eq. (3-23) is taken the following form for separation of variables

$$w(x,t) = \sum_{r=1}^{N_r} \phi_r(x) e^{j\omega_r t} \tag{3-26}$$

Then Eq. (3-23) can be rewritten in terms of normal mode shape function ϕ_i

$$\frac{d^4 \phi_i(x)}{dx^4} - (\frac{\lambda_i}{l})^4 \phi_i(x) = 0 \tag{3-27}$$

where $(\lambda_i/l)^4 = m\omega_i^2/EI$.

Considering the boundary conditions of the cantilever beam

at the clamped end: $\phi\big|_{x=0} = 0, \quad \phi'\big|_{x=0} = 0$ (3-28a)

at the free end: $\phi''\big|_{x=l} = 0, \quad \phi'''\big|_{x=l} = 0$ (3-28b)

The general solution of Eq. (3-27) is given by

$$\phi_i = \eta_{i1} \cosh \lambda_i \frac{x}{l} + \eta_{i2} \sinh \lambda_i \frac{x}{l} + \eta_{i3} \cos \lambda_i \frac{x}{l} + \eta_{i4} \sin \lambda_i \frac{x}{l} \tag{3-29}$$

where the arbitrary constants, η_{ij}, $j = 1, \cdots, 4$, are determined from the boundary conditions in Eq. (3-28):

$$\eta_{i1} = -\eta_{i3}, \ \eta_{i2} = -\eta_{i4} \tag{3-30a}$$

and
$$\begin{bmatrix} \cosh\lambda_i + \cos\lambda_i & \sinh\lambda_i + \sin\lambda_i \\ \sinh\lambda_i - \sin\lambda_i & \cosh\lambda_i + \cos\lambda_i \end{bmatrix} \begin{Bmatrix} \eta_{i1} \\ \eta_{i2} \end{Bmatrix} = 0 \tag{3-30b}$$

For nontrivial solution of η_{ij}, vanishing the determinant in Eq. (3-30b) leads to

$$\cosh\lambda_i \cos\lambda_i + 1 = 0 \tag{3-31}$$

By numerically solving the above transcendental equation, successive values of λ_i correspond to the modes of the beam and the natural frequency of the i^{th} mode can be calculated as

$$\omega_i = \lambda_i^2 \sqrt{EI/ml^4} \tag{3-32}$$

The normal mode shape function of solution Eq. (3-29) can be rewritten as

$$\phi_i = \cosh\lambda_i \frac{x}{l} - \cos\lambda_i \frac{x}{l} - \eta_i \left(\sinh\lambda_i \frac{x}{l} - \sin\lambda_i \frac{x}{l} \right) \tag{3-33}$$

where $\eta_i = \eta_{i2}/\eta_{i1} = (\cosh\lambda_i + \cos\lambda_i)/(\sinh\lambda_i + \sin\lambda_i)$. Table 3.1 lists the mode shape constants of λ_i and η_i for a cantilever beam from the handbook (Blevins, 1995). Figure 3.5 displays first five mode shapes of a cantilever beam.

Table 3.1 Mode shape constants of λ_i and η_i for a cantilever beam

Mode No. i	λ_i	η_i
1	1.87510407	0.734095514
2	4.69409113	1.018467319
3	7.85475744	0.999224497
4	10.99554073	1.000033553
5	14.13716839	0.999998550
>5	$(2i\text{-}1)\pi/2$	≈1.0

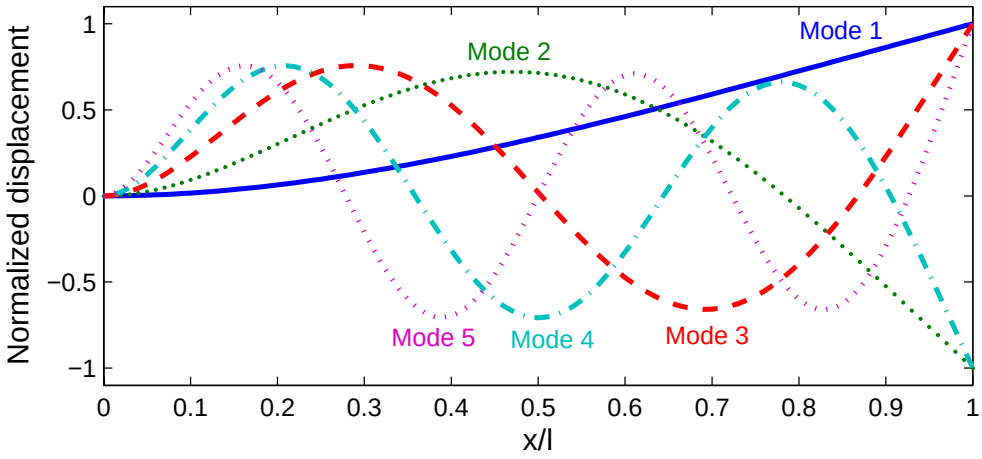

Figure 3.5 First five mode shapes of a cantilever beam

3.3.3 Governing equations of the MsM harvesting device

By taking mode shape function of Eq. (3-33) and using integral formulas containing ϕ_i from the handbook (Blevins, 1995), the closed-form of modal matrices can be further simplified as

$$\begin{aligned}\mathbf{M} &= [M_{ij}] = \left[\int_{V_s} \rho_s \phi_i \phi_j dV_s + \int_{V_M} \rho_M \phi_i \phi_j dV_M\right] \\ &= < M_s + M_M > \; = \; < M >\end{aligned} \tag{3-34a}$$

$$\begin{aligned}\mathbf{K} &= [K_{ij}] = \left[\int_{V_s} E_s \phi_i'' \phi_j'' z^2 dV_s + \int_{V_M} E^H \phi_i'' \phi_j'' z^2 dV_M\right] \\ &= \frac{EI}{l^3} < \lambda_i^4 >\end{aligned} \tag{3-34b}$$

$$\mathbf{C} = \alpha < M > + \frac{\beta EI}{l^3} < \lambda_i^4 > \tag{3-34c}$$

$$\begin{aligned}\mathbf{G} &= \{G_i\} = \frac{zNd^* E^H A_M}{l} \left\{\int_0^l \phi_i''^T(x) dx\right\} \\ &= \frac{2Nd^* E^H A_M h_M}{l^2} \left\{(-1)^{i+1} \eta_i \lambda_i\right\}^T\end{aligned} \tag{3-34d}$$

$$\mathbf{F} = \{F_i\} = \left\{ -\ddot{w}_B m \int_0^l \phi_i^T(x)dx \right\} = -2M\ddot{w}_B \{\eta_i / \lambda_i\}^T \tag{3-34e}$$

where [ ] and < > indicate square and diagonal matrices, respectively, { } denotes row vector, M is the total mass of the copper substrate and Metglas laminate, EI is given by Eq. (3-24).

The following conclusions can be drawn from Eq. (3-34):

1. Except **M**, all the other closed-forms of modal parameters including **K**, **C**, **G**, and **F** of the MsM harvesting are functions of mode shape constants λ_i and η_i associated with the i^{th} individual normal mode.
2. Because the mechanical displacement is decomposed into N_r generalized coordinates $\mathbf{r}(t)$, the normal mode transformation enables to change the set of coupled N_r-DOF equations of motion into a set of N_r uncoupled 1-DOF equations of motion.
3. The governing Eq. (3-22) is valid not only below the fundamental natural frequency, but also in a wide frequency range up to any high natural frequency ω_{N_r}. The natural frequency matrix from Eq. (3-34) can be calculated as $[\omega_i] = \sqrt{\mathbf{K}\mathbf{M}^{-1}} = < \lambda_i^2 \sqrt{EI/Ml^3} >$, which is identical to Eq. (3-32).

Eq.(3-22) can be expressed in frequency domain as

$$-\omega^2 \mathbf{M}\tilde{\mathbf{r}} + j\omega \mathbf{C}\tilde{\mathbf{r}} + \mathbf{K}\tilde{\mathbf{r}} + \mathbf{G}\tilde{i} = \tilde{\mathbf{F}} \tag{3-35a}$$

$$\tilde{v} = j\omega \mathbf{G}^T \tilde{\mathbf{r}} - j\omega L \tilde{i} \tag{3-35b}$$

where ~ indicates Fourier transform of the parameter.

Following the procedure in Session 3.2, the total internal energy of the MsM harvesting device is given by

$$\mathcal{E} = \tilde{\mathbf{r}}^T \tilde{\mathbf{F}} + \frac{1}{j\omega} \tilde{v} \tilde{i} \tag{3-36}$$

Substitution of $\tilde{\mathbf{F}}$ and $\tilde{v}$ by Eq. (3-35) yields

$$\begin{aligned} \mathcal{E} &= \tilde{\mathbf{r}}^T (\mathbf{K} - \omega^2 \mathbf{M} + j\omega \mathbf{C}) \tilde{\mathbf{r}} + \tilde{\mathbf{r}}^T \mathbf{G} \tilde{i} + \mathbf{G}^T \tilde{\mathbf{r}} \tilde{i} - L \tilde{i}^2 \\ &= \mathcal{E}_m + \mathcal{E}_{\text{me}} + \mathcal{E}_{\text{em}} + \mathcal{E}_e \end{aligned} \tag{3-36}$$

where subscripts *m*, *e* and *me* (or *em*) indicate the mechanical, electrical, mutual electromechanical energy, respectively. Note that the negative sign in Eq. (3-36) indicates 180° phase delay of electrical energy contained by the equivalent inductance of the coil.

Then a global electromechanical coupling coefficient k_g of the harvesting device can be introduced as

$$k_g^2 = \frac{\mathcal{E}_{\text{me}} \mathcal{E}_{\text{em}}}{\mathcal{E}_m \mathcal{E}_e} = \frac{\tilde{\mathbf{r}}^T \mathbf{G} \mathbf{G}^T \tilde{\mathbf{r}}}{L \tilde{\mathbf{r}}^T (\mathbf{K} - \omega^2 \mathbf{M} + j\omega \mathbf{C}) \tilde{\mathbf{r}}} \tag{3-37}$$

Because the MsM harvesting device is operated at its individual natural frequency ω_i, Eq. (3-22) can be reduced to 1-DOF system associated with the i^{th} normal mode.

$$M_i \ddot{r}_i + C_i \dot{r}_i + K_i r_i + G_i i_i = F_i \tag{3-38a}$$

$$v_i = G_i \dot{r}_i - L \dot{i}_i \tag{3-38b}$$

To further simplify Eq (3-37) for a given mode, Eq. (3-38) can be grouped in the Laplace domain as

$$\begin{Bmatrix} \overline{F}_i \\ \overline{V}_i \end{Bmatrix} = \begin{bmatrix} Z_m & G_i \\ G_i & -sL \end{bmatrix} \begin{Bmatrix} \overline{U}_i \\ \bar{I}_i \end{Bmatrix} \tag{3-39}$$

where the overbar indicates the variable in Laplace domain, *s* is the Laplace variable, $Z_m = M_i s + C_i + K_i / s$ is the mechanical impedance, $\overline{V}_i$ and $\bar{I}_i$ are the unknown output voltage and current, $\overline{U}_i$ is the unknown relative velocity of $\dot{r}_i$ in Laplace domain, and

$\overline{F} = 2s^2 M w_B \eta_i / \lambda_i$ is the base excitation force with the known base displacement w_B. Therefore Eq. (3-39) has two equations for three unknowns: $\overline{V_i}$, $\bar{I}_i$, and $\overline{U_i}$. To obtain the unique solution, another relation needs to be introduced.

The global electromechanical coupling coefficient k_g for the i^{th} vibration mode is derived from Eq. (3-37)

$$k_g = \frac{\mathcal{E}_{\text{mM}}}{\sqrt{\mathcal{E}_{\text{m}} \mathcal{E}_{\text{M}}}} = \frac{G}{\sqrt{sLZ_m}} \tag{3-40}$$

At resonance frequency ω_i, it can be further reduced via Eqs. (3-18d) and (3-34d):

$$k_g^2 = \frac{4\sqrt{M}\, E^H A_M h_M^2}{C_i \sqrt{EI \cdot l^3}} \eta_i^2 k^2 \tag{3-41}$$

From Eq. (3-41), several useful guidelines for designing MsM harvesting devices can be concluded:

1. The energy conversion efficiency for the MsM harvester is proportional to k_g^2. Meanwhile, the global electromechanical coupling coefficient k_g is linearly proportional to material coupling coefficient k.
2. Although k_g is not an explicit function of frequency ω_i, it is proportional to the value of mode shape constant η_i. According to Table 3.1, this result implies that for the same device the fundamental vibration mode offers the lowest k_g. On the other hand, the influence of η_i on k_g is not significant because of $\eta_i \approx 1.0, \quad i \geq 2$.
3. k_g is independent of the number of turns of the pick-up coil, N. However, N should not be too small in the actual design; otherwise the induced voltage in the coil will be too small to be rectified by the electronic circuit. Furthermore, a large

number of N can guarantee the accuracy of (3-16) due to the assumption of long solenoid coil.

4. The thicker Metglas layer is, the higher k_g results.

3.3.4 Model extension for a cantilever beam with a tip mass

Because the ambient vibrations from the surroundings are usually at low frequencies, it is necessary to add a tip mass at the free end of the MsM harvesting device to reduce its fundamental natural frequency. Another advantage of using the tip mass is to increase the bending stress, leading to greater harvested energy. The model derived in Session 3.3.1 for usual cantilever beam needs to be further extended or modified. The analysis with the additional tip mass is covered briefly based on the previous work (Bhat and Wagner, 1976; duToit *et al.*, 2005; Oguamanam, 2003).

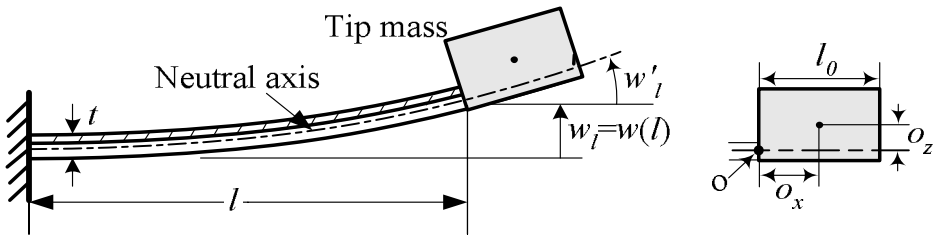

Figure 3.6 Uniform cantilever beam with a tip mass

As illustrated in Figure 3.6, the mass center of a tip mass M_0 with small length of l_0 does not coincide with that of the free end of the beam, O. The Euler-Bernoulli beam theory and the normal mode superposition can still be employed to determine the transverse displacement $w(x,t)$, thus both Eqs. (3-23) and (3-29) governing the beam $0 \le x \le l$ are still valid and not repeated here. However, the arbitrary constants η_{ij}, $j = 1, \cdots, 4$,

are solved from the modified boundary conditions with the rigid tip mass. Assume that both the beam and the tip mass are uniform in the axial direction with mass per length of m and m_0, respectively. The boundary conditions at the clamped end are the same as Eq. (3-28a), so Eq. (3-30a) is valid for this case. In addition, the boundary conditions at the point where the beam end and the tip mass are connected are obtained by a variational method as

$$EIw_l'' = \omega^2 I_0 w_l' + \omega^2 S_0 w_l \tag{3-42a}$$

$$EIw_l''' = -\omega^2 M_0 w_l - \omega^2 S_0 w_l' \tag{3-42b}$$

where $M_0 = m_0 l_0$, $S_0 = M_0 o_x$, $I_0 = J + M_0(o_x^2 + o_z^2)$, and $J = M_0(l_0^2 + t_0^2)/12$ is the mass moment of inertia of the tip mass around its mass center, t_0 and l_0 are the thickness and length of the tip mass, respectively. By introducing the nondimensional ratios $\hat{M}_0 = M_0/ml$, $\hat{S}_0 = S_0/ml^2$, and $\hat{I}_0 = I_0/ml^3$, the boundary conditions of Eq. (3-42) yield the following matrix equation

$$\begin{bmatrix} a_{11} & a_{12} \\ a_{21} & a_{22} \end{bmatrix} \begin{Bmatrix} \eta_{i3} \\ \eta_{i4} \end{Bmatrix} = 0 \tag{3-43}$$

where

$$a_{11} = (\cosh\lambda_i + \cos\lambda_i) + \lambda_i^3 \hat{I}_0(-\sinh\lambda_i - \sin\lambda_i) + \lambda_i^2 \hat{S}_0(-\cosh\lambda_i + \cos\lambda_i) \tag{3-44a}$$

$$a_{12} = (\sinh\lambda_i + \sin\lambda_i) + \lambda_i^3 \hat{I}_0(-\cosh\lambda_i + \cos\lambda_i) + \lambda_i^2 \hat{S}_0(-\sinh\lambda_i + \sin\lambda_i) \tag{3-44b}$$

$$a_{21} = (\sinh\lambda_i - \sin\lambda_i) + \lambda_i \hat{M}_0(\cosh\lambda_i - \cos\lambda_i) + \lambda_i^2 \hat{S}_0(\sinh\lambda_i + \sin\lambda_i) \tag{3-44c}$$

$$a_{22} = (\cosh\lambda_i + \cos\lambda_i) + \lambda_i \hat{M}_0(\sinh\lambda_i - \sin\lambda_i) + \lambda_i^2 \hat{S}_0(\cosh\lambda_i - \cos\lambda_i) \tag{3-44d}$$

λ_i can be numerically solved by vanishing the determinant of the matrix in Eq.(3-43). Then the expressions of natural frequencies in Eq. (3-32) and normal mode shapes in Eq. (3-33) are updated as

$$\omega_i = \lambda_i^2 \sqrt{EI/ml^4} \tag{3-45}$$

$$\phi_i = \cosh\lambda_i \frac{x}{l} - \cos\lambda_i \frac{x}{l} - \eta_i \left(\sinh\lambda_i \frac{x}{l} - \sin\lambda_i \frac{x}{l} \right) \tag{3-46}$$

where $\eta_i = a_{11}/a_{12}$. If there is no tip mass attached at the free end, i.e. $\hat{M}_0$, $\hat{S}_0$, and $\hat{I}_0$ are all zero, Eq. (3-43) is degraded to Eq. (3-30b).

A numerical example is illustrated the effects of tip-mass-to-beam-mass ratio $\hat{M}_0$ on the mode shapes and structural natural frequencies as shown in Figure 3.7 and Figure 3.8, respectively. The parameters in the simulation are chosen as $o_x = 0.1l$, $o_z = 0.066l$, $l_0 = 2o_x$, $t_0 = 2o_x$, and $\hat{M}_0$ varies in a range of [0, 10]. From Figure 3.7, especially the last three plots, it can be seen that the larger $\hat{M}_0$ leads to a longer effective wavelength of the mode shapes; on the other hand the amplitude at the connection point of tip mass and beam end approaches zero when mass ratio $\hat{M}_0$ increases, because infinite $\hat{M}_0$ leads to a clamp end boundary condition. The dependency of natural frequencies on the ratio of tip mass to beam mass is shown in Figure 3.8, where the frequency of each mode is normalized by the natural frequencies of the cantilever beam without tip mass, i.e. at the condition of $\hat{M}_0 = 0$. It can be seen that (1) mass ratio $\hat{M}_0$ remarkably reduces the structural natural frequencies and it steeply decays in the range of $\hat{M}_0 < 0.5$; (2) in the

range of $\hat{M}_0$ beyond 0.5, the lower modes, the larger influence and a flat region can be observed in the forth and fifth modes.

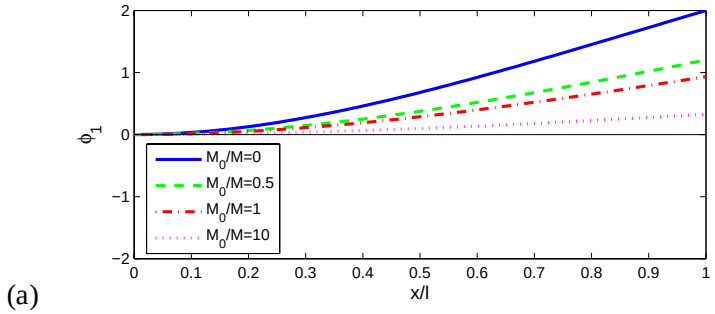

(a)

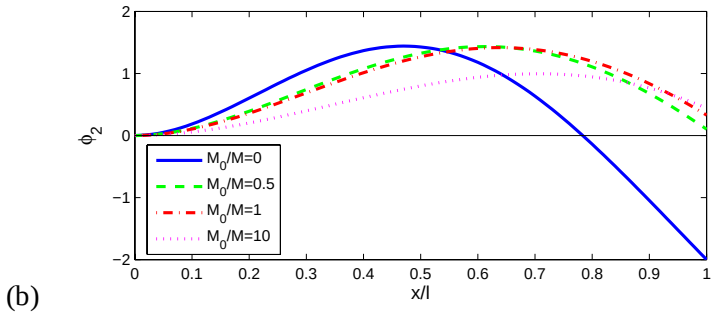

(b)

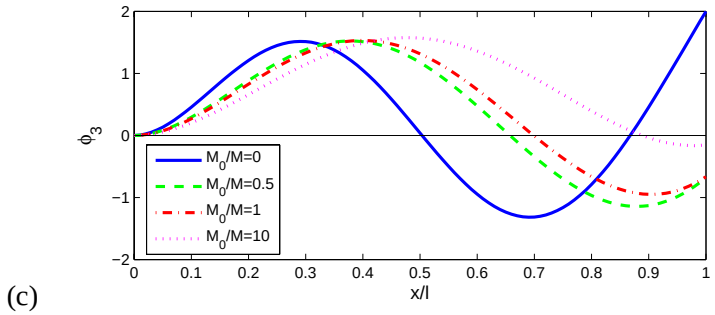

(c)

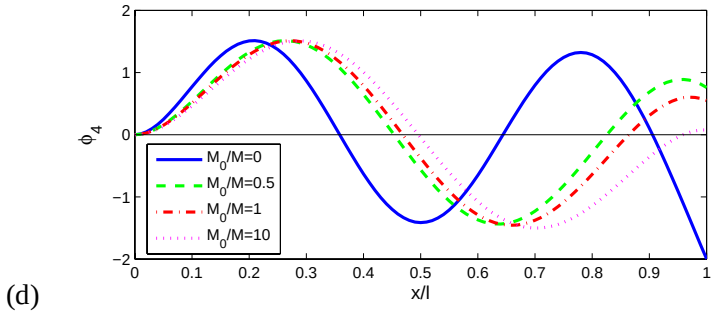

(d)

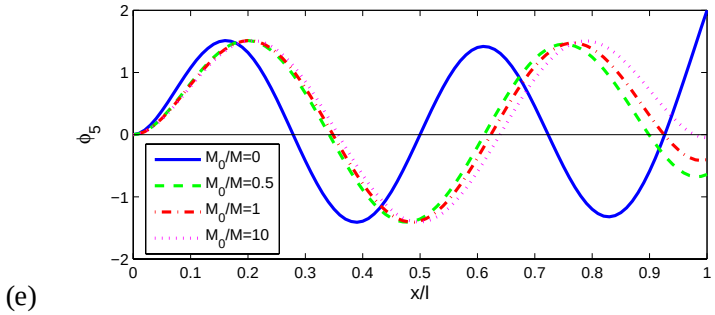

(e)

Figure 3.7 First five mode shapes of a cantilever beam with different tip-to-beam mass ratios

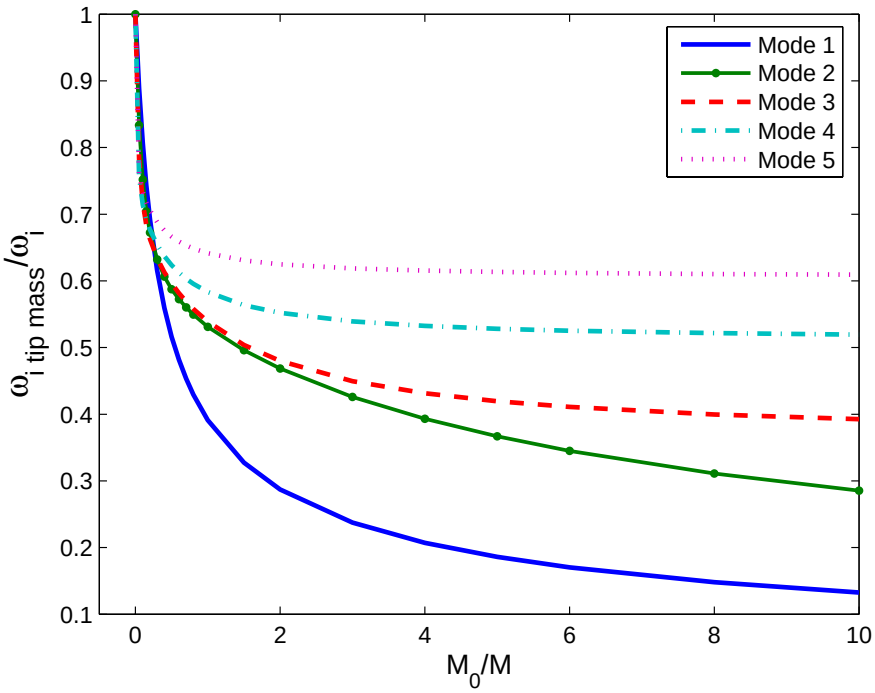

Figure 3.8 Effect of tip-to-beam mass ratio, M_0/M, on the structural natural frequencies

The effective mass of the beam can be obtained from a similar variational approach discussed in Session 3.3.1. The modal mass matrix Eq.(3-18a) should be replaced by the following equation when a tip mass is attached to the cantilever beam

$$\mathbf{M} = \int_{V_s} \rho_s \boldsymbol{\phi}^T(x)\boldsymbol{\phi}(x)dV_s + \int_{V_M} \rho_M \boldsymbol{\phi}^T(x)\boldsymbol{\phi}(x)dV_M + M_0\boldsymbol{\phi}^T(l)\boldsymbol{\phi}(l) + 2S_0\boldsymbol{\phi}^T(l)\boldsymbol{\phi}'(l) + I_0\boldsymbol{\phi}'^T(l)\boldsymbol{\phi}'(l) \tag{3-47}$$

The effective stiffness matrix **K** has the same expression as Eq.(3-18b) except for the mode shape function.

At last, the external work term should be re-evaluated to include the inertial loading due to the tip mass. Eq.(3-19) needs to be updated by taking the contribution of both uniform cantilever beam and the tip mass. The displacement of the tip mass is calculated in terms of the displacement and rotation of the tip of the beam.

$$\mathbf{F} = -\ddot{w}_B \left[m\int_0^l \boldsymbol{\phi}^T(x)dx + m_0 \int_l^{l+l_0} \boldsymbol{\phi}^T(l)dx + m_0 \int_l^{l+l_0} x\boldsymbol{\phi}'^T(l)dx \right] \tag{3-48}$$

According to Figure 3.8, Eq. (3-47), and (3-48), it has been theoretically proved that the tip mass produces two major effects. First, it significantly reduces the natural frequencies of the beam, in other words it is feasible to change the natural frequencies by adjusting the tip mass. Second, the tip mass induces additional excitation force under the same base excitation.

3.4 Power Analysis

Because Eq. (3-39) has two equations for three unknowns, another relation associated with characteristic of an electrical load is required to obtain a unique solution. A pure resistive load is unable to contain the converted energy but dissipates into Joule heat. In general, the power is analyzed at the steady-state for a resistive load. This analysis is conveniently performed in the Laplace, or frequency domain. On the contrary, a capacitive load, or storage device, can collect the converted energy. Thus charging storage device is in transient state and it should be modeled by original ODEs (ordinary differential equations) in the time domain. Although the following formulation is established for the harvesting device vibrating around its individual natural frequency ω_i, it can be extended for general non-resonance frequency by using the corresponding parameters in Eq. (3-34).

3.4.1 Power analysis for a resistive load

Eliminating velocity $\overline{U}_i$ in Eq. (3-39) gives the volt-ampere characteristic of the harvesting device as shown in Figure 3.9.

$$\overline{V_i} = -(sL + G_i^2 / Z_m)\bar{I}_i + G_i \overline{F_i} / Z_m \tag{3-49}$$

The open-circuit voltage and short-circuit current can be obtained from Eq. (3-49) by setting $\bar{I}_i = 0$ and $\overline{V_i} = 0$, respectively

$$\overline{V}_{open} = G_i \overline{F}_i / Z_m \tag{3-50a}$$

and

$$\bar{I}_{short} = G_i \overline{F}_i / (sLZ_m + G_i^2) \tag{3-50b}$$

In Figure 3.9, the dotted area under the volt-ampere characteristic line is associated with converted electrical power:

$$P_{el} = \frac{1}{2}\overline{V}_{open}\bar{I}_{short} = \frac{G_i^2 \overline{F}_i^2}{2Z_m(sLZ_m + G_i^2)} \tag{3-51}$$

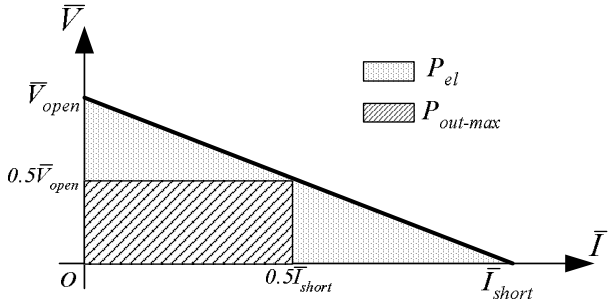

Figure 3.9 The volt-ampere characteristic of the harvesting device

For a resistive load *R*, all the above equations are valid in steady-state. The maximum output power from the harvesting device can be easily obtained by maximizing the rectangular in the slashed region in Figure 3.9.

$$P_{out-\max} = \frac{\overline{V}_{open}\bar{I}_{short}}{4} = \frac{G_i^2 \overline{F}_i^2}{4Z_m(sLZ_m + G_i^2)} \tag{3-52}$$

and the corresponding optimized load is the slope of the line connecting the origin and ($0.5\bar{I}_{short}$, $0.5\bar{V}_{open}$) in Figure 3.9

$$R_{\text{op}} = \frac{\bar{V}_{open}}{\bar{I}_{short}} = (sLZ_m + G_i^2)/Z_m \tag{3-53}$$

To compute the general frequency response, Eq. (3-35) can be expressed in frequency domain as

$$-\omega^2\mathbf{M}\tilde{\mathbf{r}} + j\omega\mathbf{C}\tilde{\mathbf{r}} + \mathbf{K}\tilde{\mathbf{r}} + \mathbf{G}\tilde{i} = \tilde{\mathbf{F}} \tag{3-54a}$$

$$R\tilde{i} = j\omega\mathbf{G}^T\tilde{\mathbf{r}} - j\omega L\tilde{i} \tag{3-54b}$$

Solving the above equations, the frequency response of the transverse displacement can be obtained

$$\tilde{w}(x,\omega) = \boldsymbol{\phi}(x)\tilde{\mathbf{r}}(\omega) \tag{3-55}$$

where $\tilde{\mathbf{r}}$ is solved from Eq. (3-54)

$$\tilde{\mathbf{r}} = \left[\mathbf{K} - \omega^2\mathbf{M} + j\omega\mathbf{C} + \frac{j\omega}{R + j\omega L}\mathbf{G}\mathbf{G}^T\right]^{-1}\tilde{\mathbf{F}} \tag{3-56}$$

For completeness, the transient response in time domain can be obtained by solving the following ODEs in state-space form derived from Eq. (3-22)

$$\begin{Bmatrix}\dot{\mathbf{r}}\\ \ddot{\mathbf{r}}\\ \dot{i}\end{Bmatrix} = \begin{bmatrix}0 & \mathbf{I} & 0\\ -\mathbf{M}^{-1}\mathbf{K} & -\mathbf{M}^{-1}\mathbf{C} & -\mathbf{M}^{-1}\mathbf{G}\\ 0 & \mathbf{G}^T/L & R/L\end{bmatrix}\begin{Bmatrix}\mathbf{r}\\ \dot{\mathbf{r}}\\ i\end{Bmatrix} + \begin{bmatrix}0\\ -\mathbf{M}^{-1}\mathbf{F}\\ 0\end{bmatrix} \tag{3-57}$$

where **I** is $N_r \times N_r$ identity matrix. After solving $\mathbf{r}(t)$, the transverse displacement $w(x,t)$ of the cantilever beam can be determined from Eq. (3-14). Since the general matrix forms of

modal parameters are employed, Eqs. (3-54)- (3-57) are valid in frequency range up to ω_i and not limited on each natural frequency.

3.4.2 Charging performance for a capacitive load

Eq. (3-52) is not desirable in actual energy harvesting because all scavenged electrical power is dissipated on the resistor *R*. Examining a capacitive load *C*, the energy storage device, is of importance for assessing MsM's charging capability. Due to the transient state of charging the energy storage *C*, the original ODEs in time domain are employed in modeling

$$\begin{cases} F_i = M_i\ddot{r}_i + C_i\dot{r}_i + K_i r_i + G_i i_i \\ v_i = G_i\dot{r}_i - L\dot{i}_i \\ i_i = C\dot{v}_i \end{cases} \tag{3-58}$$

where $F = 2M\eta_i\omega_i^2 w_B \sin\omega_i t/\lambda_i$ is the equivalent input force from the base. Then Eq. (3-58) can be rearranged as a set of first-order ODEs in terms of matrix form in state-space

$$\begin{Bmatrix} \dot{r}_i \\ \ddot{r}_i \\ \dot{v}_i \\ \ddot{v}_i \end{Bmatrix} = \begin{bmatrix} 0 & 1 & 0 & 0 \\ \dfrac{-K_i}{M_i} & \dfrac{-C_i}{M_i} & 0 & \dfrac{-G_i C}{M_i} \\ 0 & 0 & 0 & 1 \\ 0 & & \dfrac{-1}{LC} & \dfrac{G_i}{LC} \end{bmatrix} \begin{Bmatrix} r_i \\ \dot{r}_i \\ v_i \\ \dot{v}_i \end{Bmatrix} + \begin{Bmatrix} 0 \\ \dfrac{2\eta_i\omega_i^2 w_B}{\lambda_i}\sin\omega_i t \\ 0 \\ 0 \end{Bmatrix} \tag{3-59}$$

with initial conditions

$$r(0) = \dot{r}(0) = 0 \text{ and } v(0) = \dot{v}(0) = 0 \tag{3-60}$$

Generally the closed-form solution of *v* from the Eq. (3-60) is unlikely to obtain, but numerical solution can be simply computed by finite difference algorithms such as

Runge-Kutta method. The ideal rectification without loss and forward voltage drop can be considered by substituting $\sin \omega_i t$ with its absolute values in Eq. (3-59).

4 Experimental Studies

Chapter 4 discusses the energy harvesting circuit design, experimental setup for testing, and compares the harvested energy from experiments with theoretical prediction. The Joule magnetostrictive effect is measured via a bimetallic beam method, and then the piezomagnetic constant of Metglas 2605SC is determined from the linear region of λ-H curve. In the circuit design, a voltage quadrupler is introduced to achieve two functions: rectifying the output AC voltage from the pick-up coil and increasing the DC voltage level. Due to the desirable features mentioned in Chapter 1, an ultracapacitor is used as an energy storage device. In addition, the circuit contains a smart voltage regulator with a DC-DC converter IC to clamp the output voltage level for driving the external wireless electronics. All the functionalities are built in a compact PCB. In the experiments, a shaker is employed to simulate ambient harmonic vibration, and then the harvester converts the vibration to electrical energy and then stores the electrical energy. The experimental results are also compared with the theoretical prediction. The maximum output power on a resistive load and charging the ultracapacitor can achieve 200 μW and 576 μW, respectively.

4.1 Joule Effect Measurement

Unlike Terfenol-D, Metglas is in a form of ribbon with 10~30 μm thickness and 10^{-2}~18cm width (Meeks and Hill, 1983). To measure the magnetostriction of the thin ribbon, an approach utilizing bending deformation of a cantilever beam induced from magneto-mechanical coupling of the Metglas is proposed based on the concept described by Klokholm (1976). A Metglas ribbon is bonded on one side of the substrate. Upon

application of a DC magnetic field in the length direction, an elastic magnetostriction strain λ is induced. In order to satisfy continuous displacement along the bonded surface, the beam bending deformation is induced. A detailed formulation of bimetallic beam based on the Euler-Bernoulli theory is developed.

Figure 4.1 illustrates the geometry of the bimetallic cantilever beam. Assume the beam with length *l*, thickness *t*, width *b*, cross sectional area *A* and isotropic with Young's modulus *E*, whereas subscripts *1* and *2* indicate the Metglas ribbon and aluminum substrate, respectively. Suppose that *x*-axis is along the length direction with its origin at the left end and *z*-axis is in the transverse direction with its origin at the neutral axis. $w(x)$ is the deflection along *x*-axis of the beam.

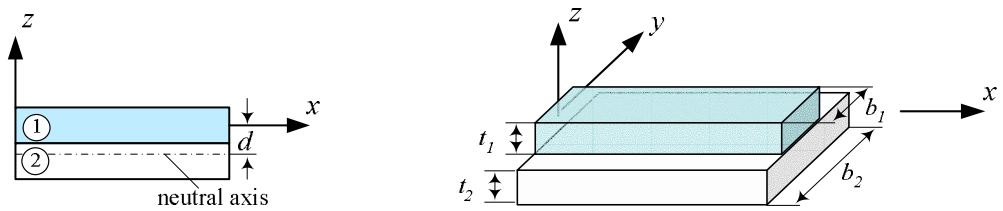

(a) (b)

Figure 4.1 Bimetallic cantilever beam consisting of aluminum substrate and Metglas ribbon

The strains in the Metglas ribbon and the aluminum substrate are given by

$$\varepsilon_1 = -z\frac{d^2w}{dx^2} - \lambda \text{ and } \varepsilon_2 = -z\frac{d^2w}{dx^2} \tag{4-1}$$

From Hooke's law and Eq. (4-1), the stress-strain relation at each layer based on the Euler-Bernoulli beam theory can be expressed

$$\sigma_1 = -E_1 z\frac{d^2w}{dx^2} - E_1\lambda \text{ and } \sigma_2 = -E_2 z\frac{d^2w}{dx^2} \tag{4-2}$$

For the beam in self-equilibrium static, first the axial force equilibrium along the *x*-axis leads to

$$\int_{A_1} \sigma_1 dA + \int_{A_2} \sigma_2 dA = 0 \tag{4-3}$$

Substituting Eq. (4-2) into Eq. (4-3) yields

$$\int_{-d}^{t_1-d} b_1(-E_1 z \frac{d^2w}{dx^2} - E_1\lambda)dz + \int_{-t_2-d}^{-d} -b_2 E_2 z \frac{d^2w}{dx^2} dz = 0 \tag{4-4}$$

where *d* is distance from the neutral axis to the interface of two materials. By integrating, Eq. (4-4) can be reduced to

$$\frac{d^2w}{dx^2}\left[\frac{\beta b_1 h_1^2 - b_2 h_2^2}{2} - d\left(\beta h_1 b_1 + h_2 b_2\right)\right] + \beta b_1 h_1 \lambda = 0 \tag{4-5}$$

where $\beta = E_1/E_2$.

Second, the equilibrium of bending moment $M(x)$ at a given section is

$$M(x) = \int_{A_1} \sigma_1 z dA + \int_{A_2} \sigma_2 z dA = 0 \tag{4-6}$$

Substituting Eq. (4-2) into Eq. (4-6)

$$\int_{-d}^{t_1-d} b_1(-E_1 z^2 \frac{d^2w}{dx^2} - E_1\lambda z)dz + \int_{-t_2-d}^{-d} -b_2 E_2 z^2 \frac{d^2w}{dx^2} dz = 0 \tag{4-7}$$

Integrating the above equation yields

$$\frac{d^2w}{dx^2}\left[d^2\left(\beta t_1 b_1 + t_2 b_2\right) + d\left(b_2 t_2^2 - \beta b_1 t_1^2\right) + \frac{\beta b_1 t_1^3 + b_2 t_2^3}{3}\right] - \beta d b_1 t_1 \lambda + \frac{\beta b_1 t_1^2 \lambda}{2} = 0 \tag{4-8}$$

Substituting value of *d* from Eq. (4-5) into Eq. (4-8), the final expression of the bimetallic beam with magnetostriction on the top layer can be written as

$$w(x) = \frac{-6\beta b_1 b_2 t_1 t_2 (t_1 + t_2)\lambda}{\beta^2 b_1^2 t_1^4 + b_2^2 t_2^4 + \beta b_1 b_2 t_1 t_2 (6 t_1 t_2 + 4 t_1^2 + 4 t_2^2)} x^2 \tag{4-9}$$

where negative sign indicates the free end of the bimetallic cantilever is bent downwards when the Metglas ribbon is subjected to positive magnetostriction.

If the tip deflection δ of the free end can be measured from an experiment, the magnetostriction λ of the ribbon can be easily calculated from Eq. (4-9)

$$\lambda = \frac{\beta^2 b_1^2 t_1^4 + b_2^2 t_2^4 + \beta b_1 b_2 t_1 t_2 (6t_1 t_2 + 4t_1^2 + 4t_2^2)}{-6\beta b_1 b_2 t_1 t_2 (t_1 + t_2) l^2} \delta \tag{4-10}$$

Eq. (4-10) can be further simplified, if the Metglas and its substrate have the same width, $b_1 = b_2 = b$

$$\lambda = \frac{\beta^2 t_1^4 + t_2^4 + \beta t_1 t_2 (6t_1 t_2 + 4t_1^2 + 4t_2^2)}{-6\beta t_1 t_2 (t_1 + t_2) l^2} \delta \tag{4-11}$$

Therefore the Joule magnetostriction can be experimentally determined by measuring the tip deflection of the bimetallic beam with known the materials properties and the thicknesses.

As shown in Figure 4.2, the cantilever unimorph comprising a transversely annealed Metglas 2605SC ribbon and a thin aluminum 6061-T6 substrate is located in the center of a bias coil driven by an adjustable DC voltage source from an IDL-800 electrical bread board. The bias coil generates a controllable magnetic field and causes magnetostriction effect into the Metglas ribbon. The magnetic field from the coil is measured by Magnetic Instrumentation 912 Gauss meter whose Hall probe is put into the center of the coil. The tip deflection δ at the free end of the unimorph is measured by a laser displacement sensor (Micron-Epsilon optoNCDT1607).

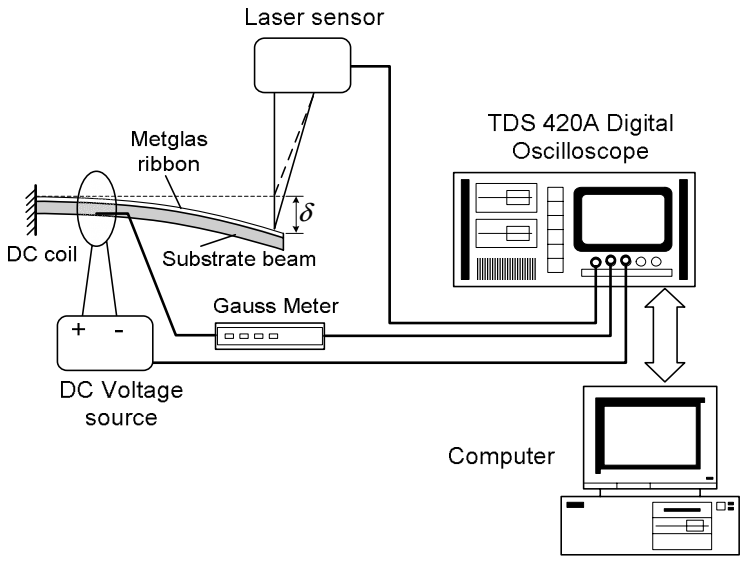

Figure 4.2 Experimental set-up for measuring magnetostriction of Metglas

Furthermore, a digital oscilloscope (Tektronix TDS420A) records the variation of the deflection δ corresponding to the applied DC voltage as shown in Figure 4.3 where discontinuities of applied voltage result from manual adjustment. Because the applied voltage varies slowly, the bending deformation can be considered as quasi-static and the voltage is regarded as DC at each time instant. After measuring the tip deflection δ, the magnetostrictive strain in Metglas ribbon can be determined by Eq. (4-11). Form Figure 4.3, it is evident that the magnetostriction of Metglas always induces elongation of the ribbon and does not depend on the polarity of the DC voltage. The slope of magnetostriction λ-H curve decreases gradually with the increase of magnetic field and reaches its saturation state. Although the hysteresis exists in the magnetostriction λ-H curve, it can be neglected.

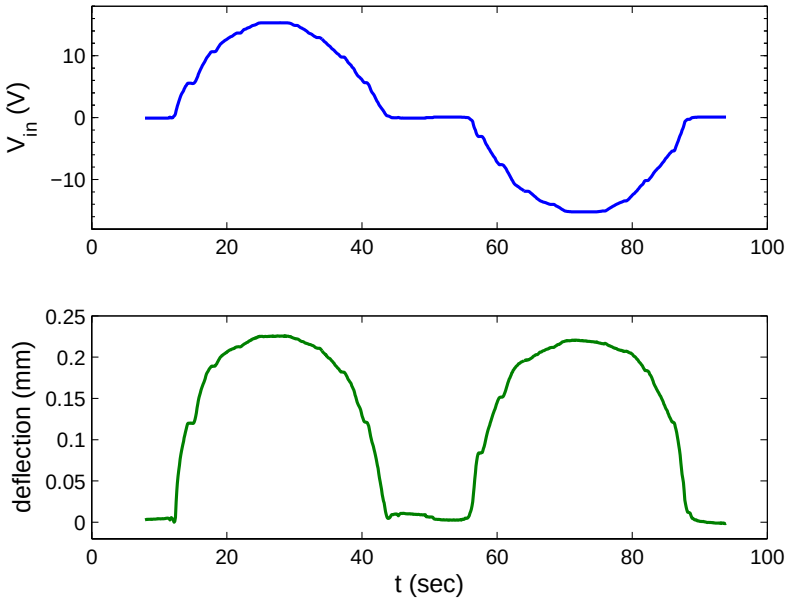

Figure 4.3 Experimental waveforms of the DC voltage and the deflection of the bimetallic beam

As shown in Figure 4.4, a linear region marked as red dashed lines can be observed in the λ-H curve where the magnetostrictive strain is less than 12μ. The slope of such linear region is 380 nm/A, corresponding to the piezomagnetic constant d of Metglas 2605SC.

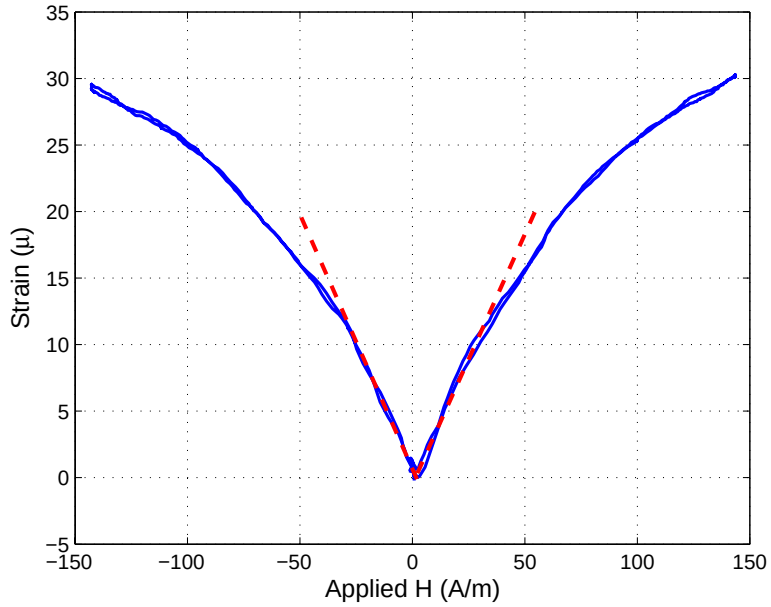

Figure 4.4 λ-H magnetostriction curves of annealed Metglas 2605SC

4.2 Circuit Design

As shown in Figure 4.5, the electrical circuit for the MsM harvester consists of three parts: a voltage quadrupler, a 3F ultracapacitor C_5 for energy storage, and a smart regulator. The functionalities of each part will be discussed in the following sub-sessions.

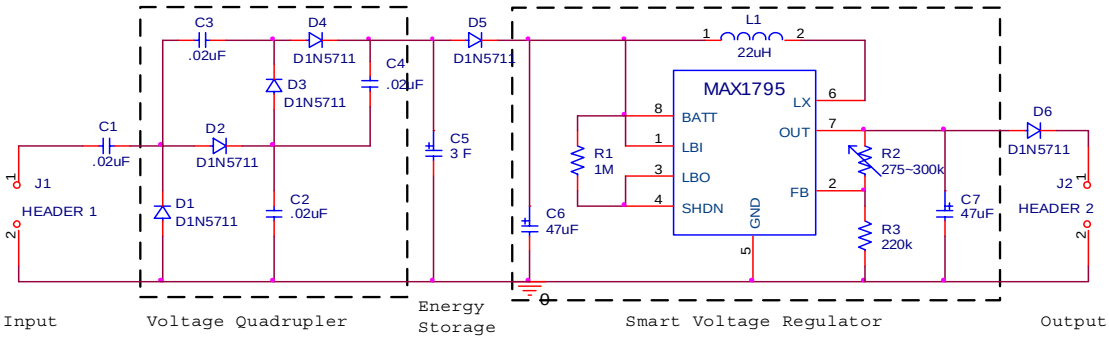

Figure 4.5 Energy harvesting circuit

4.2.1 Voltage quadrupler

The AC voltage generated from the pick-up coil is normally less than 1V, which is insufficient to charge the storage device. Note that for energy storage voltage rectification is indispensable. Although conventional half-wave or full-wave diode bridges can rectify AC to DC voltage, the resulting DC voltage becomes even lower because of the voltage drops of each diode.

To overcome such challenge, a voltage multiplication circuit is introduced as shown in Figure 4.6. It not only rectifies AC to DC voltage, but also increases the DC output voltage level by some multiples of the peak AC voltage. Figure 4.6(a) shows a voltage doubler based on a half-wave rectifier. When the AC voltage is in negative polarity, diodes D_1 and D_2 are in on and off state, respectively; then capacitor C_1 is charged up to virtually the peak voltage V_{ac}. When the polarity changes to positive, C_1 is unable to discharge via D_1; D_2 is on so the voltage on C_1 is added to that of the supply AC voltage, charging C_2 to twice the peak value. Thus, it tends to hold the DC voltage $2V_{ac}$. In practice, due to inevitable forward voltage drop on each diode and discharging of C_2 through an electrical load, C_2 is never quite charged to the ideal value of $2V_{ac}$, but will come very close. During the following positive half-period, any discharge to the electrical load is replenished *via* C_1 from the voltage of C_2 at the start of the half-cycle halfway up to $2V_{ac}$; in this respect C_2 behaves like a smoothing capacitance, which acts like a rectifier filter reducing ripples in the output voltage. Therefore a voltage multiplication circuit can achieve the purposes of AC-DC rectification, filtering, and increasing the DC voltage level simultaneously (Howatson, 1996).

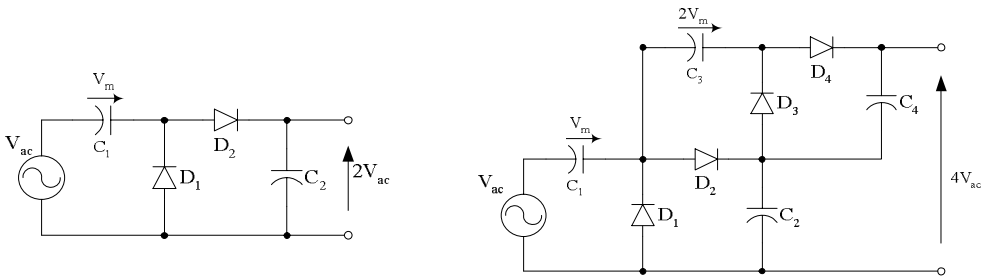

(a) (b)

Figure 4.6 Voltage multiplication: (a) doubler; (b) quadrupler

As shown in Figure 4.6(b), two voltage doublers can be assembled to form a so-called voltage quadrupler, which has the similar principle as mentioned above. Theoretically, the DC voltage may be increased by arbitrary multiples. However, because the power is conserved, the corresponding output current of this circuit decrease reciprocally. Furthermore, the more diodes are used the lower efficiency results because of their forward voltage drops and internal resistance. Therefore, the voltage quadrupler is adopted to enhance the voltage up to at least 2.0V in this study.

Using PSpice, Figure 4.7 displays simulated results of open circuit voltages from doubler and quadrupler circuits. Assume the AC input has a peak value 1.0V with 800 Hz frequency, respectively. 0.02 μF capacitors and Schottky diodes D1N5711 are used in the circuits. Since the forward voltage drop of each diode is considered in PSpice, $V_{doubler}$ and $V_{quadupler}$ approach 1.75 V and 3.5V, respectively, at steady state rather than the values of 2 V and 4 V, respectively.

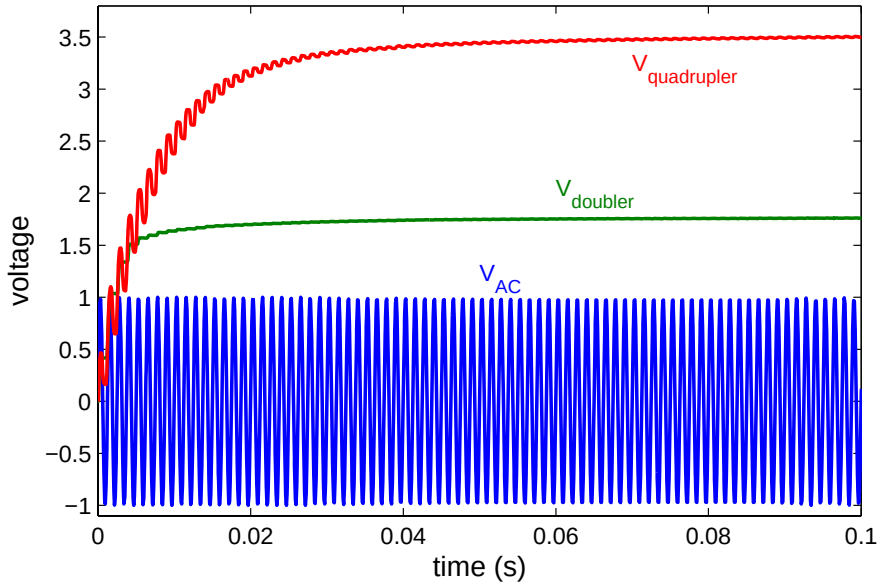

Figure 4.7 AC input voltage, output voltages from doubler and quadrupler simulated by PSpice.

4.2.2 Smart voltage regulator

When the ultracapacitor discharges, its voltage will drop correspondingly. Therefore, a voltage regulator is required to clamp the output voltage. The key IC used in this study is MAX1795, a high efficiency step-up DC-DC converter intended for small portable hand-held devices. It features Maxim's True-Shutdown™ circuitry, which fully disconnects the output from the input in shutdown, improves efficiency, and eliminates costly external components. MAX1795 only consumes 25µA quiescent current and 2µA shut-down current. It was reported by the manufacturer that its conversion efficiency could reach up to 95%. For additional in-system flexibility, a battery monitoring comparator (LBI/LBO) remains active even when the DC-DC converter is in the shutdown mode. Figure 4.8 and Table 4.1 provide pin configuration and functions of MAX1795/1796/1797 series, respectively.

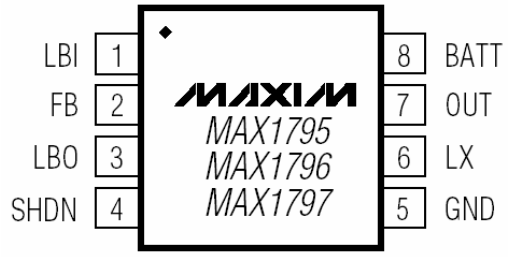

Figure 4.8 Pin configuration of step-up DC-DC converter MAX1795/1796/1797

Table 4.1 Pin functions of MAX1795/1796/1797

Pin	Name	Function
1	LBI	Low-Battery Comparator Input. Internally set to trip at +0.85V. This function remains operational in shutdown.
2	FB	Dual-Mode™ Feedback Input. Connect to GND for preset 5.0V output. Connect to OUT for preset 3.3V output. Connect a resistive voltage-divider from OUT to GND to adjust the output voltage from 2V to 5.5V.
3	LBO	Low-Battery Comparator Output, Open-Drain Output. LBO is low when VLBI < 0.85V. This function remains operational in shutdown.
4	SHD	Shutdown Input. If SHDN is high, the device is in shutdown mode, OUT is high impedance, and LBI/LBO are still operational. Connect shutdown to GND for normal operation.
5	GND	Ground
6	LX	External Inductor Connection
7	OUT	Power Output. OUT provides bootstrap power to the IC.
8	BATT	Battery input and damping switch connection

The input voltage range is +0.7V to V_{OUT}, where V_{OUT} can be set from +2.0V to +5.5V. Self-startup is guaranteed from +0.85V. The MAX1795 has a preset, pin-selectable 5V or 3.3V output. The output can also be adjusted to other voltages, using two external resistors. The current limit of MAX1795 is 0.25A. For higher current limits, MAX1796 and 1797 can stand 0.5A and 1A, respectively (Maxim Integrated Products, 2000). Accordingly, the advantage of higher efficiency, low startup voltage, adjustable

output, and compact size make MAX1795 suitable for DC-DC conversion of the proposed MsM harvester.

By designing peripheral circuit as shown in Figure 4.5, the output voltage level from MAX1795 can be adjusted and the variable resistor R_1 is determined by

$$R_1 = R_2\left(\frac{V_{out}}{V_{FB}} - 1\right) \tag{4-12}$$

where V_{FB} = +1.245V, and V_{OUT} may vary from +2V to +5.5V. R_2 should be chosen less than 250 kΩ. On the other hand, V_{OUT} can be fixed to 3.3V or 5.0V by directly connecting the FB pin to OUT or GND, respectively.

Connecting BATT to LBI, the lowest startup voltage can be guaranteed from +0.85V. In other words, MAX1795 is operating when the voltage level on pin BATT is higher than +0.85V. By connecting pin LBO to SHDN, the MAX1795 can be automatically shut down when the input voltage drops below a preset threshold +0.85V. Shottky diodes D_5 and D_6 prevent the reverse current. C_6 and C_7 are input and output filter capacitors, respectively, to remove unwanted ripples. L_1 is the external inductor for MAX1795 (Maxim Integrated Products, 2000).

4.2.3 PCB design for energy harvesting circuit

Layout design for the PCB is critical for minimizing ground bounce and noise. The gaps between MAX1795's GND pin and the ground leads of the input and output filter capacitors should be kept less than 5mm apart. In addition, all connections to the FB and LX pins should be as short as possible. In particular, when external feedback resistors are used, they would be better located as close to FB pin as possible. To maximize output power and efficiency and minimize output ripple voltage, a ground plane is employed and

the MAX1795's GND pin is directly soldered to the ground plane (Maxim Integrated Products, 2000). With all the considerations above, the layout of PCB is carefully designed by ORCAD 10.5® and the actual PCB has a compact dimension 25mm×35mm as shown in Figure 4.9. All the surface mounted electrical components for the PCB are listed in Table 4.2.

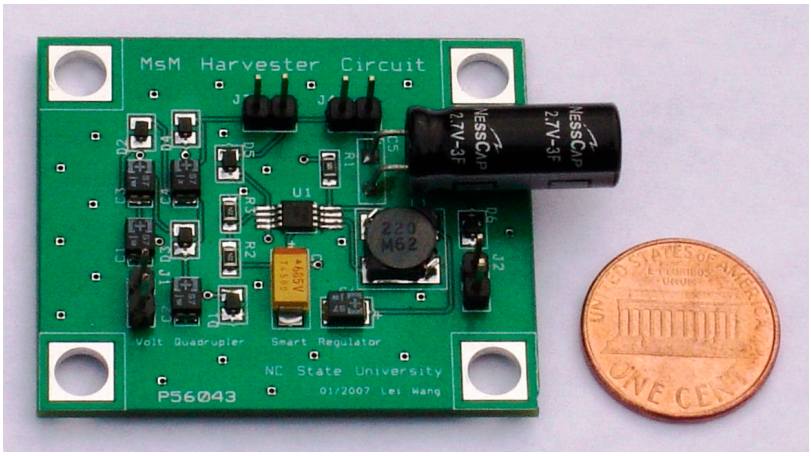

Figure 4.9 Actual PCB of the MsM harvesting circuit

Table 4.2 Electrical components on the PCB

Component	Value	Vender	Manufacture part No.
L_1	22 µH	Sumida Co.	CDRH6D28NP-220NC
C_1~C_4	0.22 µF	AVX Co.	12065C224KAT2A
C_5	3 F	NessCap Co.	ESHSR-0003C0-002R7
C_6	47 µF	Sanyo Co.	POSCAP 6TPB47M
C_7	10 µF	AVX Co.	TPSD106K035R0125
D_1~D_6	N/A	Diodes Inc.	BAT54WS-7-F
R_1	1 MΩ	Panasonic - ECG	ERJ-P06J105V
R_2	330 kΩ~3 MΩ	Panasonic - ECG	EVM-7JSX30BY5
R_3	220 kΩ	Panasonic - ECG	ERJ-6GEYJ224V

4.3 Experimental Setup

To verify the theoretical prediction and test the outputs from the MsM energy harvester, the instruments for the experiments are set up as shown in Figure 4.10. An Angilent 3220A function harvester excites sinusoidal signal. Then the signal is sent to a TDS420A oscilloscope and a K-H7602 amplifier to drive the LDS V201 vibration shaker. The MsM harvesting device with a 100-turned pick-up coil is screwed on the top of LDS V201 shaker. Meanwhile a Micro-Epsilon optoNCDT 1607 laser sensor measures the time-varying displacement of the MsM harvester. The voltage signals of the laser sensor are recorded by the digital oscilloscope.

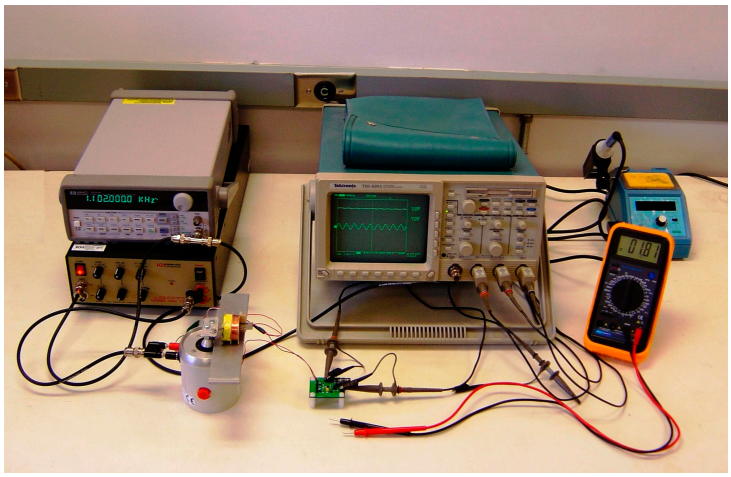

Figure 4.10 Experimental set-up

4.4 Experimental Results

4.4.1 Powering a resistive load

In the resistive load test, six layers of Metglas 2605SC (total thickness of 0.3 mm including adhesive) without the copper substrate are laminated by 3M® DP-810 adhesive

and a seismic mass is attached at the free end of the cantilever beam such that the fundamental resonance frequency is as low as 58 Hz. Rectification is not required and the harvesting circuit does not need. The output voltage and power on external resistive loads are shown in Figure 4.11 and Figure 4.12, respectively, where the solid line represents theoretical prediction and dots indicate experimental results. From Figure 4.12, it can be seen that the maximum output voltage is about 0.15V and the maximum output power reaches 200 μW and corresponding power density is 900 $\mu W/cm^3$, which is higher than that of most piezo-based harvesters (Beeby *et al.*, 2006), typically about 3 times higher than that reported by Roundy *et al.* (2004). The voltage is, however, lower than the forward voltage drop of diodes; thus it is not practical in actual applications. Increasing the resonance frequency and using voltage multiplier can be viable solution. The discrepancy of maximum power between theory prediction and experimental measurement may result from the measured equivalent damper coefficient. It should be noted that unlike peizo-based harvester the MsM harvester of this design is not well suited to drive high resistive load; because the MsM harvester has inductive characteristic, as opposed to capacitive characteristic for the peizo-based harvesters.

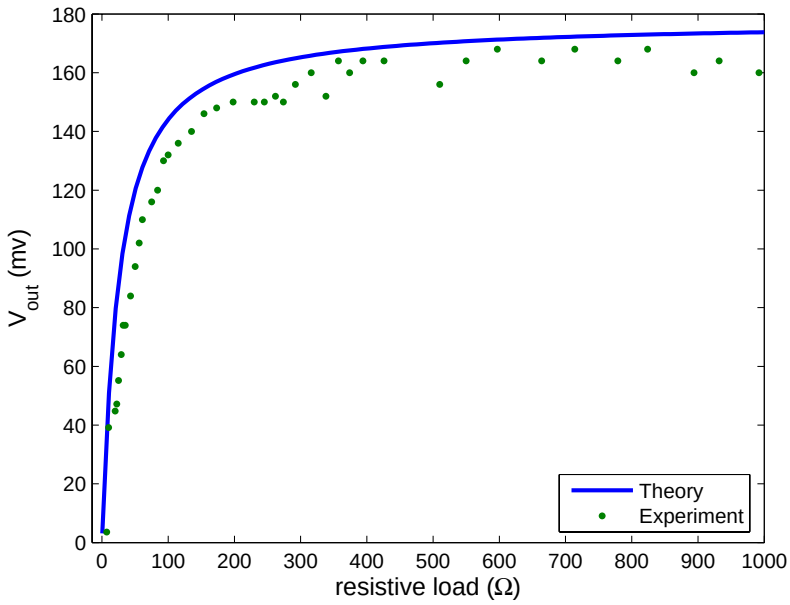

Figure 4.11 Comparison of theoretical and experimental results on output voltage under 58.1 Hz and 1g acceleration

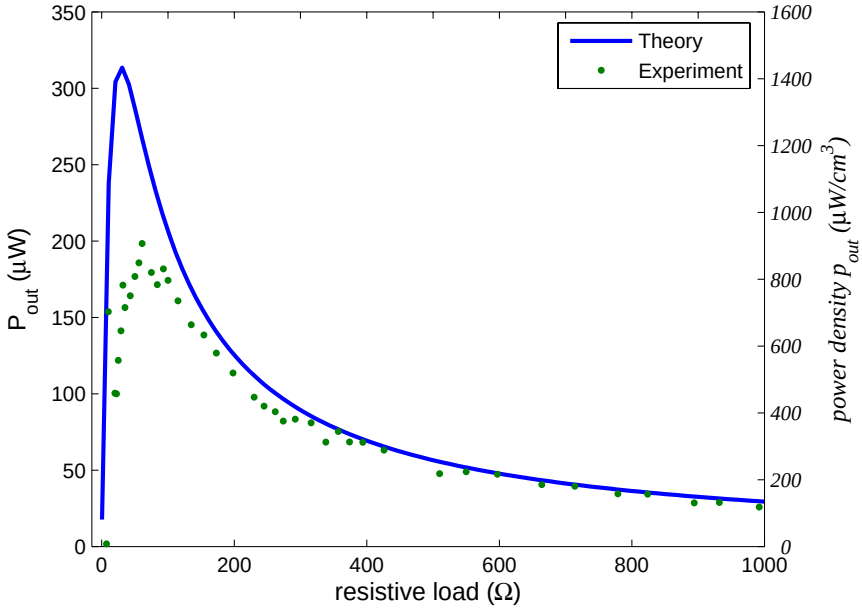

Figure 4.12 Comparison of theoretical and experimental results on output power under 58.1 Hz and 1g acceleration

4.4.2 Charging the ultracapacitor

The aim of conducting the second test is to assess the charging ability of the MsM harvester on the ultracapacitor at relative high frequency (~1 kHz). An eight-layered Metglas 2605SC laminate (total volume of 0.95cm^3) without the seismic mass is bonded on a copper substrate (0.4mm thickness). The output from the pick-up coil is connected to the energy harvesting circuit for storage and regulation.

Figure 4.13 shows the experimental waveforms of the tip displacement of the harvester, AC voltage from the pick-up coil and DC output from the voltage quadrupler circuit. Under a vibration with resonance frequency of 1.1 kHz and peak acceleration of 8.06m/s^2 (or, 0.82g), the amplitude of tip displacement, measured by Micro-Epsilon optoNCDT 1607 laser sensor, is about 0.05mm as shown in the top plot; and the induced AC voltage from the pick-up coil has the amplitude of 0.7V represent by a dashed line. Theoretically, the DC output from the voltage quadrupler should be 2.8V. However, due to forward voltage drop of each BAT54WS diode, the actual DC voltage level can reach 2.3V.

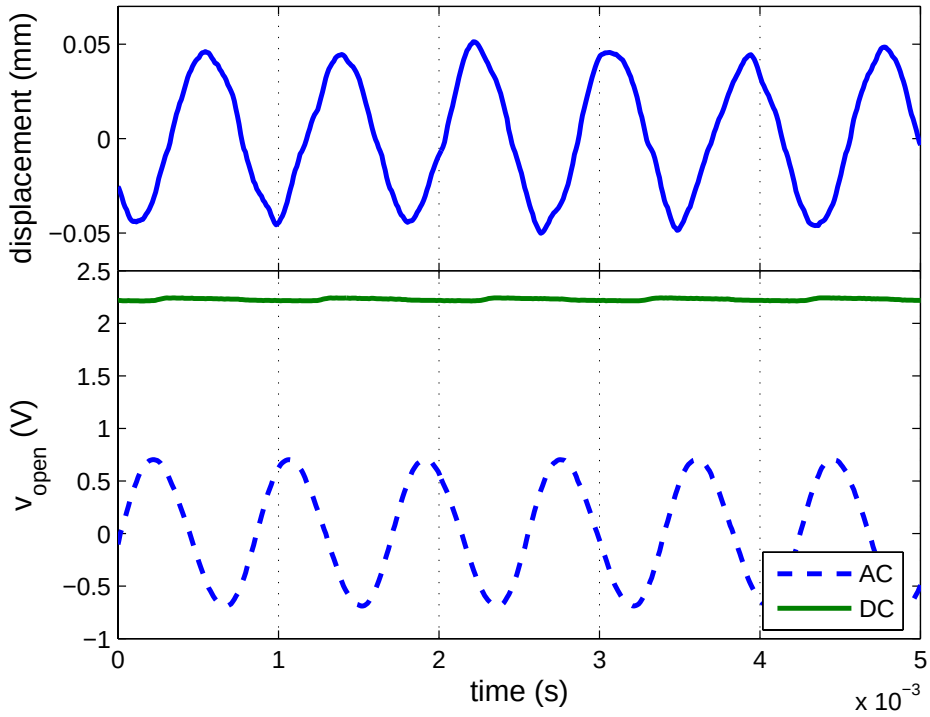

Figure 4.13 Tip displacement of the MsM harvester, AC voltage from pick-up coil and DC output from the voltage quadrupler

The last experiment is to evaluate the MsM harvester's charging capability on the ultracapacitor and test the performance of the smart voltage regulator. After the voltage on ultracapacitor C_5 reaches 2.3V, a 1 kΩ resistive load is connected to the smart regulator for measuring discharging history of C_5 and the output voltage level. Figure 4.14 shows the experimental voltage history on C_5 in the upper plot and the recorded DC voltage output from the voltage regulator in the lower plot. From the upper plot of Figure 4.14, it is evident that the voltage on C_5 contains one exponentially charging cycle and one discharging cycle with almost linear decay rate. When the voltage on C_5 is higher than 0.9V, the smart regulator can self-startup and the output voltage is clamped at 3.3V as shown in the lower plot. On the other hand, if the voltage on C_5 is less than threshold

value of 0.9V, the smart regulator will shut-down by itself to reduce dissipated energy. The voltage on the ultracapacitor may fluctuate, but the output voltage level from the smart voltage regulator is fixed at a certain constant value until the voltage on the ultracapacitor is less than 0.9V. Because the harvested power from the vibration is small, it takes about 3.5 hours to fully charge the 3F ultracapacitor. Correspondingly, the average power and the average power density for charging the capacitive energy storage can achieve 576 μW and 606 μW/cm^3, respectively, which are higher than those of most piezo-based harvesters (Beeby *et al.*, 2006), typically about 2 times higher than Ref (Roundy *et al.*, 2004). Note that the volume of Metglas laminate is used in calculating the power density.

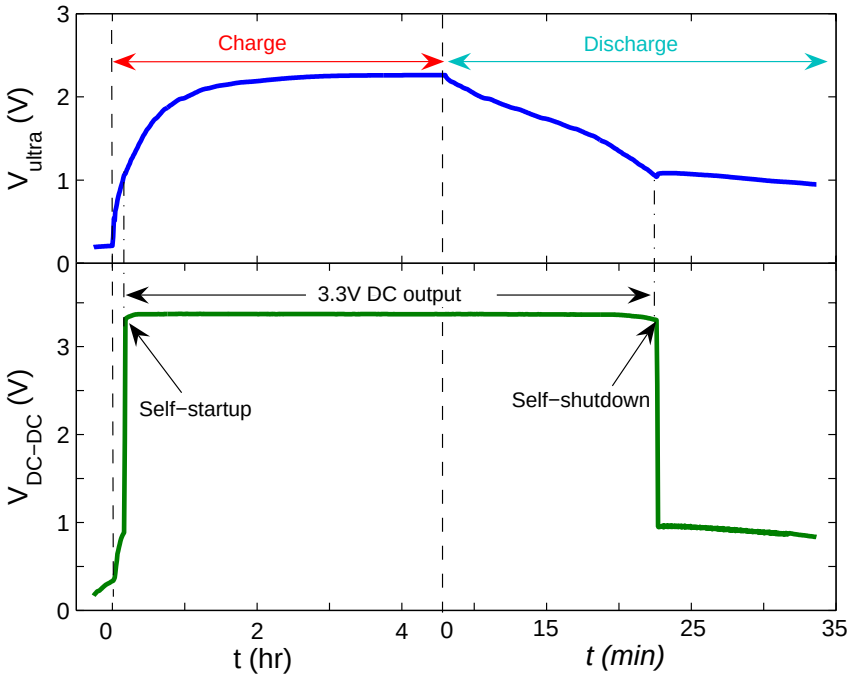

Figure 4.14 Experimental results of the charging/discharging of the ultracapacitor and output performance of the smart voltage regulator

5 Conclusions

5.1 Conclusions

In this study, energy harvesting techniques have been reviewed. Three common vibration energy harvesting techniques are compared and the advantages of MsM-based energy harvesting over PZT approach are emphasized. Then the principle of MsM including Joule and Villari effects is discussed in detail from physics origin. A working prototype of a new class of energy harvester based on MsM has been designed, developed, and tested. It has been shown experimentally that the MsM vibration energy harvester holds a promise as an alternate scheme of energy harvesting apart from the common piezoelectric vibration energy harvesting approaches.

Specific contributions of this study to vibration energy harvesting are summarized as follows:

(a) A general architecture of energy harvesting-based wireless sensors is proposed and this architecture provides a useful design guideline for other types of energy harvesters as well.

(b) A closed-form of governing equations of motion for the MsM harvesting device is derived by the Hamilton's Principle in conjunction with normal mode superposition method based on the Euler-Bernoulli beam theory. Then the effect of a tip mass attached to the beam element on the modal frequencies and mode shapes is also modeled. This formulation is valid in a wide frequency range up to any higher natural frequency.

(c) A bimetallic cantilever method is proposed to measure the Joule magnetostriction λ-H curve and the piezomagnetic constant is experimentally obtained from the linear regime of the curve.

(d) To enhance the coupling coefficient (k >0.9), Metglas 2605SC is transversely annealed by a strong magnetic field in the width direction of the ribbon. The annealed ribbon does not require bias magnetic field, thereby reducing the harvester size.

(e) A 3F ultracapacitor with volume of 1 cm^3 is adopted as energy storage device to achieve real-time charging and semi-permanent life cycle.

(f) An energy harvesting circuit is designed and fabricated in PCB with a plane dimension of 25mm×35mm. It consists of a voltage quadrupler, an ultracapacitor, and a smart voltage regulator. The output DC voltage level is adjustable in a range of 2.0~5.5V which is compatible with most wireless sensor electronics.

(g) In the experiment, under the vibration with resonance frequency 1.1 kHz and peak acceleration of 8.06m/s^2 (or, 0.82g) the average power and power density during charging the ultracapacitor achieves 576 μW and 606 $\mu W/cm^3$, respectively, which is compete favorably with the piezoelectric vibration energy harvesters. Note that the volume of Metglas laminate is used in calculating the power density.

5.2 Future Work

Future work may focus on the following issues to further improve the performance of the current design. First, the MsM-based harvester needs to be integrated into the WISP. Not only should the PCB of energy harvesting circuit be resized to match dimension of the WISP, but also the power switching and power management

components together with built-in algorithms need to be added into the WISP according to the general architecture discussed in Session 1.1.2.

Second, the frequency bandwidth of the harvesting device should be widened to absorb more ambient vibrations. Because of the resonant type of the device, the current design has very narrow frequency band around its natural frequencies. On the other hand, the actual ambient vibrations are rather wide-band, sometimes random. Therefore, other vibration mechanism is worth of investigating to achieve wide-band frequency response.

Third, the dimension of the pick-up coils needs to be shrunk. Compared to piezoelectric harvesters, this is also the main limitation of the MsM harvester. The recently developed printed tape coils by MEMS technique is a possible solution (Kruusing *et al.*, 1999).

At last, as mentioned in Session 1.1.4, the thin film rechargeable battery (with electrolyte film) may be a better energy storage device than the ultracapacitor. Although both devices share similar operation principle, thin film rechargeable batteries have much lower leakage than ultracapacitors. Furthermore, they are very flexible and easy to be tailored into arbitrary shape. The thin film battery may be attached to the back of the PCB or the housing wall of the harvester for further reducing the harvester size.

6 References

Amirtharajah, R., and Chandrakasan, A. P. (1998). "Self-powered signal processing using vibration-based power generation." *IEEE Journal of Solid-State Circuits*, 33(5), 687-695.

Arms, S. W., Townsend, C. P., Churchill, D. L., Galbreath, J. H., and Mundell, S. W. (2005). "Power management for energy harvesting wireless sensors." *Proceedings of SPIE*, 5763, 274-82.

Badel, A., Benayad, A., Lefeuvre, E., Lebrun, L., Richard, C., and Guyomar, D. (2006a). "Single crystals and nonlinear process for outstanding vibration-powered electrical generators." *IEEE Transactions on Ultrasonics Ferroelectrics and Frequency Control*, 53(4), 673-684.

Badel, A., Guyomar, D., Lefeuvre, E., and Richard, C. (2005). "Efficiency enhancement of a piezoelectric energy harvesting device in pulsed operation by synchronous charge inversion." *Journal of Intelligent Material Systems and Structures*, 16(10), 889-901.

Badel, A., Guyomar, D., Lefeuvre, E., and Richard, C. (2006b). "Piezoelectric energy harvesting using a synchronized switch technique." *Journal of Intelligent Material Systems and Structures*, 17(8-9), 831-839.

Bayrashev, A., Robbins, W. P., and Ziaie, B. (2004). "Low frequency wireless powering of microsystems using piezoelectric-magnetostrictive laminate composites." *Sensors and Actuators A: Physical*, 114(2-3), 244-249.

Beeby, S. P., Tudor, M. J., and White, N. M. (2006). "Energy harvesting vibration sources for microsystems applications." *Measurement Science & Technology*, 17(12), R175-R195.

Blevins, R. D. (1995). *Formulas for natural frequency and mode shape*, Krieger Pub., Malabar, Fla.

Briles, S. D., Neagley, D. L., Coates, D. M., and Freund, S. M. (2004). "Remote down-hole well telemetry." US Patent 6766141.

BTnode Project. (2005). "SNM-The sensor network museum™." http://www.btnode.ethz.ch/Projects/SensorNetworkMuseum.

Bulusu, N., and Jha, S. (2005). *Wireless sensor networks*, Artech House, Boston, MA.

Ching, N. N. H., Wong, H. Y., Li, W. J., Leong, P. H. W., and Wen, Z. Y. (2002). "A laser-micromachined multi-modal resonating power transducer for wireless sensing systems." *Sensors and Actuators A-Physical*, 97-8, 685-690.

Choi, S. H., Song, K. D., Golembiewskii, W., Chu, S. H., and King, G. C. (2004). "Microwave power for smart material actuators." *Smart Materials & Structures*, 13(1), 38-48.

Cullity, B. D. (1972). *Introduction to magnetic materials*, Addison-Wesley Pub. Co., Reading, Mass.,.

Cymbet™, Co. "Thin film lithium Ion cells." http://www.cymbet.com/features.php.

Dapino, M. J. (2004). "On magnetostrictive materials and their use in adaptive structures." *Structural Engineering and Mechanics*, 17(3-4), 303-329.

Du Trâemolet de Lacheisserie, E. (1993). *Magnetostriction: theory and applications of magnetoelasticity*, CRC Press, Boca Raton.

duToit, N. E., Wardle, B. L., and Kim, S. G. (2005). "Design considerations for MEMS-scale piezoelectric mechanical vibration energy harvesters." *Integrated Ferroelectrics*, 71, 121-160.

Elvin, N. G., Elvin, A. A., and Spector, M. (2001). "A self-powered mechanical strain energy sensor." *Smart Materials & Structures*, 10(2), 293-299.

Engdahl, G. (2000). *Handbook of giant magnetostrictive materials*, Academic, San Diego, Calif.

ETREMA Products, Inc. (2007). "Terfenol-D." http://www.etrema-usa.com/products/terfenol/.

Gao, R. X., and Cui, Y. (2005). "Vibration-based energy extraction for sensor powering: Design, analysis, and experimental evaluation." *Proceedings of SPIE*, 5765, 794-801.

Glosch, H., Ashauer, M., Pfeiffer, U., and Lang, W. (1999). "A thermoelectric converter for energy supply." *Sensors and Actuators a-Physical*, 74(1-3), 246-250.

Glynne-Jones, P., Tudor, M. J., Beeby, S. P., and White, N. M. (2004). "An electromagnetic, vibration-powered generator for intelligent sensor systems." *Sensors and Actuators a-Physical*, 110(1-3), 344-349.

Harrist, D. W. (2004). "Wireless battery charging system using radio frequency energy harvesting," M.S. Thesis, University of Pittsburgh.

Hernando, A., Vazquez, M., and Barandiaran, J. M. (1988). "Metallic glasses and sensing applications." *Journal of Physics E-Scientific Instruments*, 21(12), 1129-1139.

Heylen, W., Lammens, S., and Sas, P. (1998). *Modal analysis theory and testing*, Katholieke Universiteit Leuven, Belgium.

Hi-Z Technology, Inc. (2005). "HZ-2 thermoelectric module, produces 2.5 Watts at 3.3 Volts at matched load, uses Bismuth Telluride based semiconductors." http://www.hi-z.com/websit02.htm.

Howatson, A. M. (1996). *Electrical circuits and systems : an introduction for engineers and physical scientists*, Oxford University Press, Oxford ; New York.

Huang, J., O'Handley, R. C., and Bono, D. (2003). "New, high-sensitivity, hybrid magnetostrictive/electroactive magnetic field sensors." *Proceedings of SPIE*, 5050, 229-237.

IEEE Standard. (1991). "IEEE standard on magnetostrictive materials: piezomagnetic nomenclature." *IEEE STD 319-1990*.

IEEE Standard Board. (1991). "IEEE standard on magnetostrictive materials: piezomagnetic nomenclature." *IEEE STD 319-1990*.

Infinite Power Solutions, Inc. (2006). "LiTE*STAR Product Family." http://www.infinitepowersolutions.com/.

Inman, D. J. (2001). *Engineering vibration*, Prentice Hall, Upper Saddle River, N.J.

Kim, Y. (2003). "Ultracapacitor technology powers electronic circuits." *Power Electronics Technology*, 29(10), 34-9.

Kimura, M. (1998). "Piezo-electricity generation device." US Patent 5801475.

Klokholm, E. (1976). "Measurement of magnetostriction in ferromagnetic thin-films." *IEEE Transactions on Magnetics*, 12(6), 819-821.

Kruusing, A., Leppavuori, S., and Uusimaki, A. (1999). "Printed solenoid windings for miniature electromagnetic devices." *Journal of Micromechanics and Microengineering*, 9(2), 166-169.

Kymissis, J., Kendall, C., Paradiso, J., and Gershenfeld, N. "Parasitic power harvesting in shoes." *the 2nd International Symposium on Wearable Computers*, Pittsburgh, PA, USA, 132-9.

Lee, J. B., Chen, Z. Z., Allen, M. G., Rohatgi, A., and Arya, R. (1995). "A miniaturized high-voltage solar-cell array as an electrostatic MEMS power-supply." *Journal of Microelectromechanical Systems*, 4(3), 102-108.

Lefeuvre, E., Badel, A., Richard, C., and Guyomar, D. (2005). "Piezoelectric energy harvesting device optimization by synchronous electric charge extraction." *Journal of Intelligent Material Systems and Structures*, 16(10), 865-876.

Liu, L. (2006). "Wireless networks in structural health monitoring," Ph.D. thesis, North Carolina State University, Raleigh.

Lu, Y., and Nathan, A. (1997). "Metglas thin film with as-deposited domain alignment for smart sensor and actuator applications." *Applied Physics Letters*, 70(4), 526-528.

Makihara, K., Onoda, J., and Miyakawa, T. (2006). "Low energy dissipation electric circuit for energy harvesting." *Smart Materials & Structures*, 15(5), 1493-1498.

Mascarenas, D. L. (2006). "Development of an impedance-based wireless sensor node for monitoring of bolted joint preload," M.S. Thesis, University of California, San Diego.

Maxim Integrated Products, Inc. (2000). "MAX1795, MAX1796, MAX1797 low-supply current, step-Up DC-DC converters with true shutdown."

Maxwell Technologies, Inc. (2006). http://www.maxwell.com/ultracapacitors/index.asp.

Meeks, S. W., and Hill, J. C. (1983). "Piezomagnetic and elastic properties of metallic-glass alloys $Fe_{67}Co_{18}B_{14}Si_1$ and $Fe_{81}B_{13.5}Si_{3.5}C_2$." *Journal of Applied Physics*, 54(11), 6584-6593.

Meninger, S., Mur-Miranda, J. O., Amirtharajah, R., Chandrakasan, A. P., and Lang, J. H. (2001). "Vibration-to-electric energy conversion." *IEEE Transactions on Very Large Scale Integration (Vlsi) Systems*, 9(1), 64-76.

Metglas, Inc. (2007). "Magnetic alloy 2605SC (Iron-based)."

MIL-STD-810F. (2000). "Environmental engineering considerations and laboratory tests." Department of Defense.

Modzelewski, C., Savage, H. T., Kabacoff, L. T., and Clark, A. E. (1981). "Magnetomechanical coupling and permeability in transversely annealed Metglas 2605 alloys." *IEEE Transactions on Magnetics*, 17(6), 2837-2839.

NEC Co. (2006). http://www.nec-tokin.com/english/product/supercapacitor/index.html.

NESSCAP Co. (2006). http://www.nesscap.com.

Ottman, G. K., Hofmann, H. F., Bhatt, A. C., and Lesieutre, G. A. (2002). "Adaptive piezoelectric energy harvesting circuit for wireless remote power supply." *IEEE Transactions on Power Electronics*, 17(5), 669-676.

Paradiso, J. A., and Starner, T. (2005). "Energy scavenging for mobile and wireless electronics." *IEEE Pervasive Computing*, 4(1), 18-27.

Pescovitz, D. (2002). "The power of small tech." *Smalltimes*, 2(1).

Pfeifer, K. B., Leming, S. K., and Rumpf, A. N. (2001). "Embedded self-powered microsensors for monitoring the surety of critical buildings and infrastructures." *SAND2001-3619*, Sandia National Laboratories.

Roundy, S., and Wright, P. K. (2004). "A piezoelectric vibration based generator for wireless electronics." *Smart Materials & Structures*, 13(5), 1131-1142.

Roundy, S., Wright, P. K., and Rabaey, J. M. (2004). *Energy scavenging for wireless sensor networks: with special focus on vibrations*, Kluwer Academic, Boston.

Savage, H. T., and Spano, M. L. (1982). "Theory and application of highly magnetoelastic Metglas 2605SC." *Journal of Applied Physics*, 53(11), 8092-8097.

Schwartz, M. M. (2002). *Encyclopedia of smart materials*, J. Wiley, New York.

Shenck, N. S., and Paradiso, J. A. (2001). "Energy scavenging with shoe-mounted piezoelectrics." *IEEE Micro*, 21(3), 30-42.

Solicore, Inc. (2005). "Solicore's Flexion line of lithium polymer batteries." http://www.solicore.com/product.html.

Spano, M. L., Hathaway, K. B., and Savage, H. T. (1982). "Magnetostriction and magnetic-anisotropy of field annealed Metglas 2605 alloys Via DC M-H Loop Measurements under Stress." *Journal of Applied Physics*, 53(3), 2667-2669.

Staley, M. E. (2005). "Development of a prototype magnetostrictive energy harvesting device," M.S. Thesis, University of Maryland, College Park.

Staley, M. E., and Flatau, A. B. (2005). "Characterization of energy harvesting potential of Terfenol-D and Galfenol." *Proceedings of SPIE*, 5764, 630-40.

Starner, T. (1996). "Human-powered wearable computing." *Ibm Systems Journal*, 35(3-4), 618-629.

Stordeur, M., and Stark, I. "Low power thermoelectric generator - self-sufficient energy supply for micro systems." *Proceedings of the 1997 16th International Conference on Thermoelectrics*, pp.575-577.

Thomson, W. T., and Dahleh, M. D. (1998). *Theory of vibration with applications*, Prentice Hall, Upper Saddle River, N.J.

Timoshenko, S. (1930). *Strength of materials*, D. Van Nostrand Co., New York,.

Torah, R. (2005). "Cantilever generator." University of Southampton. School of Electronics and Computer Science, http:www.ecs.soton.ac.uk/~rnt/Cantilever_Gen_eire_v6.ppt

Umeda, M., Nakamura, K., and Ueha, S. (1996). "Analysis of the transformation of mechanical impact energy to electric energy using piezoelectric vibrator." *Japanese Journal of Applied Physics Part 1-Regular Papers Short Notes & Review Papers*, 35(5B), 3267-3273.

van der Woerd, A. C., Bais, M. A., de Jong, L. P., and Van Roermund, A. H. M. "A highly efficient micro-power converter between a solar cell and a rechargeable lithium-ion battery." Proceedings of SPIE 3328, San Diego, CA, USA, 315-25.

Vandevoorde, G., and Puers, R. (2001). "Wireless energy transfer for stand-alone systems: a comparison between low and high power applicability." *Sensors and Actuators a-Physical*, 92(1-3), 305-311.

VanSchuylenbergh, K., and Puers, R. (1996). "Self-tuning inductive powering for implantable telemetric monitoring systems." *Sensors and Actuators a-Physical*, 52(1-3), 1-7.

Wang, L., and Yuan, F. G. (2006). "Structural vibration energy harvesting by magnetostrictive materials (MsM)." The 4th China-Japan-US Symposium on Structural Control and Monitoring, Zhejiang University Press, Hangzhou, China, 147-152.

Williams, C. B., Shearwood, C., Harradine, M. A., Mellor, P. H., Birch, T. S., and Yates, R. B. (2001). "Development of an electromagnetic micro-generator." *IEEE Proceedings-Circuits Devices and Systems*, 148(6), 337-342.

Williams, C. B., and Yates, R. B. (1996). "Analysis of a micro-electric generator for microsystems." *Sensors and Actuators a-Physical*, 52(1-3), 8-11.

Yi, J., Henao-Sepulveda, J., and Toledo-Quinones, M. (2004). "Wireless temperature sensor for bearing health monitoring." *Proceedings of SPIE*, 5391, 368-76.

Zorpette, G. (2005). "Super charged." *IEEE Spectrum*, 42(1), 32-37.

Amirtharajah, R., and Chandrakasan, A. P. (1998). "Self-powered signal processing using vibration-based power generation." *IEEE Journal of Solid-State Circuits*, 33(5), 687-695.

Arms, S. W., Townsend, C. P., Churchill, D. L., Galbreath, J. H., and Mundell, S. W. (2005). "Power management for energy harvesting wireless sensors." *Proceedings of SPIE*, 5763, 274-82.

Badel, A., Benayad, A., Lefeuvre, E., Lebrun, L., Richard, C., and Guyomar, D. (2006a). "Single crystals and nonlinear process for outstanding vibration-powered electrical generators." *IEEE Transactions on Ultrasonics Ferroelectrics and Frequency Control*, 53(4), 673-684.

Badel, A., Guyomar, D., Lefeuvre, E., and Richard, C. (2005). "Efficiency enhancement of a piezoelectric energy harvesting device in pulsed operation by synchronous charge inversion." *Journal of Intelligent Material Systems and Structures*, 16(10), 889-901.

Badel, A., Guyomar, D., Lefeuvre, E., and Richard, C. (2006b). "Piezoelectric energy harvesting using a synchronized switch technique." *Journal of Intelligent Material Systems and Structures*, 17(8-9), 831-839.

Bayrashev, A., Robbins, W. P., and Ziaie, B. (2004). "Low frequency wireless powering of microsystems using piezoelectric-magnetostrictive laminate composites." *Sensors and Actuators A: Physical*, 114(2-3), 244-249.

Beeby, S. P., Tudor, M. J., and White, N. M. (2006). "Energy harvesting vibration sources for microsystems applications." *Measurement Science & Technology*, 17(12), R175-R195.

Bhat, B. R., and Wagner, H. (1976). "Natural Frequencies of a Uniform Cantilever with a Tip Mass Slender in Axial Direction." *Journal of Sound and Vibration*, 45(2), 304-307.

Blevins, R. D. (1995). *Formulas for natural frequency and mode shape*, Krieger Pub., Malabar, Fla.

Briles, S. D., Neagley, D. L., Coates, D. M., and Freund, S. M. (2004). "Remote down-hole well telemetry." US Patent 6766141.

BTnode Project. (2005). "SNM-The sensor network museum™." http://www.btnode.ethz.ch/Projects/SensorNetworkMuseum.

Bulusu, N., and Jha, S. (2005). *Wireless sensor networks*, Artech House, Boston, MA.

Ching, N. N. H., Wong, H. Y., Li, W. J., Leong, P. H. W., and Wen, Z. Y. (2002). "A laser-micromachined multi-modal resonating power transducer for wireless sensing systems." *Sensors and Actuators A-Physical*, 97-8, 685-690.

Choi, S. H., Song, K. D., Golembiewskii, W., Chu, S. H., and King, G. C. (2004). "Microwave power for smart material actuators." *Smart Materials & Structures*, 13(1), 38-48.

Cullity, B. D. (1972). *Introduction to magnetic materials*, Addison-Wesley Pub. Co., Reading, Mass.,.

Cymbet™, Co. (2006). "Thin film lithium Ion cells." http://www.cymbet.com/features.php.

Dapino, M. J. (2004). "On magnetostrictive materials and their use in adaptive structures." *Structural Engineering and Mechanics*, 17(3-4), 303-329.

du Plessis, A. J., Huigsloot, M. J., and Discenzo, F. D. "Resonant packaged piezoelectric power harvester for machinery health monitoring." San Diego, CA, USA, 224-35.

Du Trâemolet de Lacheisserie, E. (1993). *Magnetostriction: theory and applications of magnetoelasticity*, CRC Press, Boca Raton.

duToit, N. E., Wardle, B. L., and Kim, S. G. (2005). "Design considerations for MEMS-scale piezoelectric mechanical vibration energy harvesters." *Integrated Ferroelectrics*, 71, 121-160.

Elvin, N. G., Elvin, A. A., and Spector, M. (2001). "A self-powered mechanical strain energy sensor." *Smart Materials & Structures*, 10(2), 293-299.

Engdahl, G. (2000). *Handbook of giant magnetostrictive materials*, Academic, San Diego, Calif.

ETREMA Products, Inc. (2007). "Terfenol-D." http://www.etrema-usa.com/products/terfenol/.

Gao, R. X., and Cui, Y. (2005). "Vibration-based energy extraction for sensor powering: Design, analysis, and experimental evaluation." *Proceedings of SPIE*, 5765, 794-801.

Glosch, H., Ashauer, M., Pfeiffer, U., and Lang, W. (1999). "A thermoelectric converter for energy supply." *Sensors and Actuators a-Physical*, 74(1-3), 246-250.

Glynne-Jones, P., Tudor, M. J., Beeby, S. P., and White, N. M. (2004). "An electromagnetic, vibration-powered generator for intelligent sensor systems." *Sensors and Actuators a-Physical*, 110(1-3), 344-349.

Harrist, D. W. (2004). "Wireless battery charging system using radio frequency energy harvesting," M.S. Thesis, University of Pittsburgh.

Hernando, A., Vazquez, M., and Barandiaran, J. M. (1988). "Metallic glasses and sensing applications." *Journal of Physics E-Scientific Instruments*, 21(12), 1129-1139.

Hi-Z Technology, Inc. (2005). "HZ-2 thermoelectric module, produces 2.5 Watts at 3.3 Volts at matched load, uses Bismuth Telluride based semiconductors." http://www.hi-z.com/websit02.htm.

Howatson, A. M. (1996). *Electrical circuits and systems : an introduction for engineers and physical scientists*, Oxford University Press, Oxford ; New York.

Huang, J., O'Handley, R. C., and Bono, D. (2003). "New, high-sensitivity, hybrid magnetostrictive/electroactive magnetic field sensors." *Proceedings of SPIE*, 5050, 229-237.

IEEE Standard. (1991). "IEEE standard on magnetostrictive materials: piezomagnetic nomenclature." *IEEE STD 319-1990*.

Infinite Power Solutions, Inc. (2006). "LiTE*STAR Product Family." http://www.infinitepowersolutions.com/.

Inman, D. J. (2001). *Engineering vibration*, Prentice Hall, Upper Saddle River, N.J.

Kim, Y. (2003). "Ultracapacitor technology powers electronic circuits." *Power Electronics Technology*, 29(10), 34-9.

Kimura, M. (1998). "Piezo-electricity generation device." US Patent 5801475.

Klokholm, E. (1976). "Measurement of magnetostriction in ferromagnetic thin-films." *IEEE Transactions on Magnetics*, 12(6), 819-821.

Kruusing, A., Leppavuori, S., and Uusimaki, A. (1999). "Printed solenoid windings for miniature electromagnetic devices." *Journal of Micromechanics and Microengineering*, 9(2), 166-169.

Kymissis, J., Kendall, C., Paradiso, J., and Gershenfeld, N. "Parasitic power harvesting in shoes." *the 2nd International Symposium on Wearable Computers*, Pittsburgh, PA, USA, 132-9.

Lee, J. B., Chen, Z. Z., Allen, M. G., Rohatgi, A., and Arya, R. (1995). "A miniaturized high-voltage solar-cell array as an electrostatic MEMS power-supply." *Journal of Microelectromechanical Systems*, 4(3), 102-108.

Lefeuvre, E., Badel, A., Richard, C., and Guyomar, D. (2005). "Piezoelectric energy harvesting device optimization by synchronous electric charge extraction." *Journal of Intelligent Material Systems and Structures*, 16(10), 865-876.

Liu, L. (2006). "Wireless networks in structural health monitoring," Ph.D. thesis, North Carolina State University, Raleigh.

Lu, Y., and Nathan, A. (1997). "Metglas thin film with as-deposited domain alignment for smart sensor and actuator applications." *Applied Physics Letters*, 70(4), 526-528.

Makihara, K., Onoda, J., and Miyakawa, T. (2006). "Low energy dissipation electric circuit for energy harvesting." *Smart Materials & Structures*, 15(5), 1493-1498.

Mascarenas, D. L. (2006). "Development of an impedance-based wireless sensor node for monitoring of bolted joint preload," M.S. Thesis, University of California, San Diego.

Maxim Integrated Products, Inc. (2000). "MAX1795, MAX1796, MAX1797 low-supply current, step-Up DC-DC converters with true shutdown."

Maxwell Technologies, Inc. (2006). http://www.maxwell.com/ultracapacitors/index.asp.

Meeks, S. W., and Hill, J. C. (1983). "Piezomagnetic and elastic properties of metallic-glass alloys $Fe_{67}Co_{18}B_{14}Si_1$ and $Fe_{81}B_{13.5}Si_{3.5}C_2$." *Journal of Applied Physics*, 54(11), 6584-6593.

Meninger, S., Mur-Miranda, J. O., Amirtharajah, R., Chandrakasan, A. P., and Lang, J. H. (2001). "Vibration-to-electric energy conversion." *IEEE Transactions on Very Large Scale Integration (Vlsi) Systems*, 9(1), 64-76.

Metglas, Inc. (2007). "Magnetic alloy 2605SC (Iron-based)." http://www.metglas.com/.

MIL-STD-810F. (2000). "Environmental engineering considerations and laboratory tests." Department of Defense.

Modzelewski, C., Savage, H. T., Kabacoff, L. T., and Clark, A. E. (1981). "Magnetomechanical coupling and permeability in transversely annealed Metglas 2605 alloys." *IEEE Transactions on Magnetics*, 17(6), 2837-2839.

NEC Co. (2006). http://www.nec-tokin.com/english/product/supercapacitor/index.html.

NESSCAP Co. (2006). http://www.nesscap.com.

Oguamanam, D. C. D. (2003). "Free vibration of beams with finite mass rigid tip load and flexural-torsional coupling." *International Journal of Mechanical Sciences*, 45(6-7), 963-979.

Ottman, G. K., Hofmann, H. F., Bhatt, A. C., and Lesieutre, G. A. (2002). "Adaptive piezoelectric energy harvesting circuit for wireless remote power supply." *IEEE Transactions on Power Electronics*, 17(5), 669-676.

Paradiso, J. A., and Starner, T. (2005). "Energy scavenging for mobile and wireless electronics." *IEEE Pervasive Computing*, 4(1), 18-27.

Pescovitz, D. (2002). "The power of small tech." *Smalltimes*, 2(1).

Pfeifer, K. B., Leming, S. K., and Rumpf, A. N. (2001). "Embedded self-powered microsensors for monitoring the surety of critical buildings and infrastructures." *SAND2001-3619*, Sandia National Laboratories.

Roundy, S., and Wright, P. K. (2004). "A piezoelectric vibration based generator for wireless electronics." *Smart Materials & Structures*, 13(5), 1131-1142.

Roundy, S., Wright, P. K., and Rabaey, J. M. (2004). *Energy scavenging for wireless sensor networks: with special focus on vibrations*, Kluwer Academic, Boston.

Savage, H. T., and Spano, M. L. (1982). "Theory and application of highly magnetoelastic Metglas 2605SC." *Journal of Applied Physics*, 53(11), 8092-8097.

Schwartz, M. M. (2002). *Encyclopedia of smart materials*, J. Wiley, New York.

Shenck, N. S., and Paradiso, J. A. (2001). "Energy scavenging with shoe-mounted piezoelectrics." *IEEE Micro*, 21(3), 30-42.

Sodano, H. A., Park, G., and Inman, D. J. (2004). "Estimation of electric charge output for piezoelectric energy harvesting." *Strain*, 40(2), 49-58.

Solicore, Inc. (2005). "Solicore's Flexion line of lithium polymer batteries." http://www.solicore.com/product.html.

Spano, M. L., Hathaway, K. B., and Savage, H. T. (1982). "Magnetostriction and magnetic-anisotropy of field annealed Metglas 2605 alloys Via DC M-H Loop Measurements under Stress." *Journal of Applied Physics*, 53(3), 2667-2669.

Staley, M. E. (2005). "Development of a prototype magnetostrictive energy harvesting device," M.S. Thesis, University of Maryland, College Park.

Staley, M. E., and Flatau, A. B. (2005). "Characterization of energy harvesting potential of Terfenol-D and Galfenol." *Proceedings of SPIE*, 5764, 630-40.

Starner, T. (1996). "Human-powered wearable computing." *IBM Systems Journal*, 35(3-4), 618-629.

Stordeur, M., and Stark, I. "Low power thermoelectric generator - self-sufficient energy supply for micro systems." *Proceedings of the 1997 16th International Conference on Thermoelectrics*, pp.575-577.

Thomson, W. T., and Dahleh, M. D. (1998). *Theory of vibration with applications*, Prentice Hall, Upper Saddle River, N.J.

Torah, R. (2005). "Cantilever generator." University of Southampton. School of Electronics and Computer Science, http:www.ecs.soton.ac.uk/~rnt/Cantilever_Gen_eire_v6.ppt

Umeda, M., Nakamura, K., and Ueha, S. (1996). "Analysis of the transformation of mechanical impact energy to electric energy using piezoelectric vibrator." *Japanese Journal of Applied Physics Part 1-Regular Papers Short Notes & Review Papers*, 35(5B), 3267-3273.

van der Woerd, A. C., Bais, M. A., de Jong, L. P., and Van Roermund, A. H. M. "A highly efficient micro-power converter between a solar cell and a rechargeable lithium-ion battery." Proceedings of SPIE 3328, San Diego, CA, USA, 315-25.

Vandevoorde, G., and Puers, R. (2001). "Wireless energy transfer for stand-alone systems: a comparison between low and high power applicability." *Sensors and Actuators a-Physical*, 92(1-3), 305-311.

VanSchuylenbergh, K., and Puers, R. (1996). "Self-tuning inductive powering for implantable telemetric monitoring systems." *Sensors and Actuators a-Physical*, 52(1-3), 1-7.

Wang, L., and Yuan, F. G. (2006). "Structural vibration energy harvesting by magnetostrictive materials (MsM)." The 4th China-Japan-US Symposium on Structural Control and Monitoring, Zhejiang University Press, Hangzhou, China, 147-152.

Wang, L., and Yuan, F. G. (2007). "Energy harvesting by magnetostrictive material (MsM) for powering wireless sensors in SHM." *Proceedings of SPIE*, 6529, 652941.

Williams, C. B., Shearwood, C., Harradine, M. A., Mellor, P. H., Birch, T. S., and Yates, R. B. (2001). "Development of an electromagnetic micro-generator." *IEEE Proceedings-Circuits Devices and Systems*, 148(6), 337-342.

Williams, C. B., and Yates, R. B. (1996). "Analysis of a micro-electric generator for microsystems." *Sensors and Actuators a-Physical*, 52(1-3), 8-11.

Yi, J., Henao-Sepulveda, J., and Toledo-Quinones, M. (2004). "Wireless temperature sensor for bearing health monitoring." *Proceedings of SPIE*, 5391, 368-76.

Zorpette, G. (2005). "Super charged." *IEEE Spectrum*, 42(1), 32-37.

Appendix

A.1 Equivalent Circuit for the Coil Wound around the Metglas Laminate

In addition to the generalized Hamilton's Principle introduced in Session 3.3.1, the governing equation of the Metglas with a pick-up coil as shown in Figure A.1 can be derived from the following three mechanical and electromagnetic relations:

(i) Hooke's law

$$\sigma = E^H \varepsilon \tag{A.1-1}$$

(ii) Ampere's law with an assumption of long solenoid coil and neglecting fringing effect

$$H = \frac{N}{l} i \tag{A.1-2}$$

(iii) Faraday's law relating the voltage to infinitesimal portion Δl of the coil

$$\Delta v = -\Delta l \frac{N}{l} A_M \dot{B} \tag{A.1-3}$$

where $A_M = bt_M$ is the cross section area of the Metglas laminate, v and i are the electrical output voltage and current, respectively.

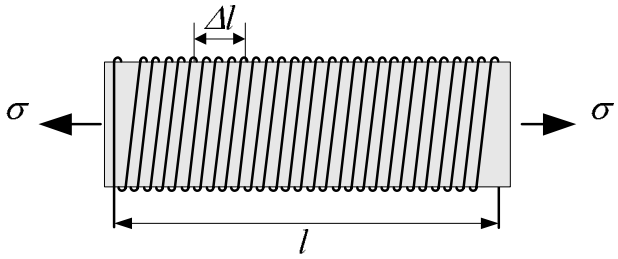

Figure A.1 Top view of Metglas laminate wound by pick-up coil

Inserting Eqs. (A.1-1), (A.1-2), and (A.1-3) into the derivative of the second equation in Eq. (3-2) with respect to time yields

$$-\Delta v = \frac{N d^* E^H A_M}{l}\dot{\varepsilon}\Delta l + \frac{\mu^T N^2 A_M}{l^2}\dot{i}\Delta l \tag{A.1-4}$$

With the limits of $\Delta v \to dv$ and $\Delta l \to dx$, integrating the resulting equation with respect to x yields the total output AC voltage from the pick-up coil as below

$$v = -\frac{N d^* E^H A_M}{l}\int_0^l \dot{\varepsilon}\, dx - \frac{\mu^T N^2 A_M}{l}\dot{i} \tag{A.1-5}$$

The first term on the right hand side of Eq. (A.1-5) signifies an electro-mechanical gyrator converting strain rate into voltage; the second term indicates an equivalent inductor of the pick-up coil.

Inserting Eq. (3-15) into the above equation leads to

$$v = \mathbf{G}^T \dot{\mathbf{r}}(t) - L\dot{i} \tag{A.1-6}$$

where

$$\mathbf{G} = \frac{N d^* E^H A_M h_M}{l}\int_0^l \boldsymbol{\phi}''^T(x)\, dx \tag{A.1-7a}$$

$$L = \frac{\mu^T N^2 A_M}{l} \tag{A.1-7b}$$

Compared Eqs. (3-18c) and (3-18d) with Eq.(A.1-7), both methods reach the exactly same results. Furthermore Eq. (A.1-6), identical to Eq.(3-22), highlights physical significance.

A.2 Governing Equations of Piezoelectric Vibration Energy Harvester

For comparison of MsM harvesters with piezoelectric harvesters, the governing equations of piezoelectric vibration energy harvesters are also derived based on a similar approach as discussed in Session 3.3.1. Assume a piezoelectric unimorph has the same geometry as in Figure 3.2(a) with substitution of a piezoelectric layer for the MsM laminate. Because the piezoelectric materials can directly convert deformation into electrical energy, a pick-up coil is not needed. The following formulation is based on the previous work (du Plessis *et al.*, 2005; duToit *et al.*, 2005; Sodano *et al.*, 2004).

The generalized Hamilton's Principle of Eq.(3-10) can be rewritten as

$$\int_{t_1}^{t_2} [\delta(T - U + W_e) + \delta W] dt = 0 \tag{A.2-1}$$

where the kinetic energy T, strain energy U , internal electrical energy W_e, and external work W are defined as

$$T = \frac{1}{2}\int_{V_s} \rho_s \dot{\mathbf{u}}^T \dot{\mathbf{u}} dV_s + \frac{1}{2}\int_{V_p} \rho_p \dot{\mathbf{u}}^T \dot{\mathbf{u}} dV_p \tag{A.2-2a}$$

$$U = \frac{1}{2}\int_{V_s} \boldsymbol{\varepsilon}^T \boldsymbol{\sigma} dV_s + \frac{1}{2}\int_{V_p} \boldsymbol{\varepsilon}^T \boldsymbol{\sigma} dV_p \tag{A.2-2b}$$

$$W_e = \frac{1}{2}\int_{V_p} ED dV_p \tag{A.2-2c}$$

where subscripts p indicates the piezoelectric layer, E and D are the electric field intensity and electric displacement in the z-axis, respectively. Assume the rest components of the electrical field are zero and the fringing effect at the edges of the piezoelectric layer is neglected.

Considering N_q charges discretely applied at positions x_j, the external work W is given by

$$\delta W = \sum_{k=1}^{N_f} \delta \mathbf{u}_k \mathbf{f}_k(t) + \sum_{j=1}^{N_q} \delta \varphi_j q_j(t) \tag{A.2-3}$$

The piezoelectric constitutive relations can be simplified into 1-DOF, because the piezoelectric harvester is operated in d_{31} mode and the induced electrical field is only along the transverse direction (IEEE Standard, 1991).

$$\begin{Bmatrix} \sigma \\ D \end{Bmatrix} = \begin{bmatrix} c_{11}^E & -e_{31} \\ e_{31}^* & \epsilon_{33}^S \end{bmatrix} \begin{Bmatrix} \varepsilon \\ E \end{Bmatrix} \tag{A.2-4}$$

where c_{11}^E is the Young's modulus in the x-axis of the piezoelectric layer under constant electrical field, ϵ_{33}^S is the permittivity of the piezoelectric layer in the z-axis under constant strain, e_{31} and e_{31}^* are the piezoelectric constants associated with d_{31} mode. Note that $e_{31} = d_{31} c_{11}^E$.

With consideration of the constitutive relations Eq. (A.2-4) and the definitions including Eq. (A.2-2) and Eq. (A.2-3), Eq. (A.2-1) are rewritten as

$$\begin{aligned} \int_{t_1}^{t_2} \Bigg[& \int_{V_s} \rho_s \delta \dot{\mathbf{u}}^T \dot{\mathbf{u}} dV_s + \int_{V_p} \rho_p \delta \dot{\mathbf{u}}^T \dot{\mathbf{u}} dV_p - \int_{V_s} E_s \delta \boldsymbol{\varepsilon}^T \boldsymbol{\varepsilon} dV_s - \int_{V_p} c_{11}^E \delta \boldsymbol{\varepsilon}^T \boldsymbol{\varepsilon} dV_p \\ & + \int_{V_p} e_{31} \delta \boldsymbol{\varepsilon}^T E dV_p + \int_{V_p} e_{31}^* \delta E \boldsymbol{\varepsilon} dV_p + \int_{V_p} \epsilon_{33}^S \delta E E dV_p \\ & + \sum_{k=1}^{N_f} \delta \mathbf{u}_k \mathbf{f}_k(t) + \sum_{j=1}^{N_q} \delta \varphi_j q_j(t) \Bigg] dt = 0 \end{aligned} \tag{A.2-5}$$

In addition to normal mode superposition of Eq. (3-14) and Euler-Bernoulli beam assumption in Eq. (3-15), the electrical potential φ can be written in terms of potential distribution function ψ_j and the generalized electrical coordinate $v_j(t)$

$$\varphi(x,t) = \sum_{j=1}^{N_q} \psi_j(x) v_j(t) = \boldsymbol{\psi}(x)\mathbf{v}(t) \tag{A.2-6}$$

where $\boldsymbol{\psi} = [\psi_1(x), \cdots, \psi_{N_q}(x)]$ is the electrical potential distribution vector, $\mathbf{v}(t) = [v_1(t), \cdots, v_{N_q}(t)]^T$ is generalized electrical coordinate vector. Meanwhile, the electrical field E is the gradient of the electrical potential distribution vector $\boldsymbol{\psi}$

$$E = -\nabla \cdot \boldsymbol{\psi} \tag{A.2-7}$$

The above assumptions can simplify Eq. (A.2-5) in terms of the modal matrices, and the equations of motion are obtained as follows

$$\mathbf{M}\ddot{\mathbf{r}} + \mathbf{K}\mathbf{r} + \boldsymbol{\Theta}\mathbf{v} = \sum_{k=1}^{N_f} \boldsymbol{\phi}^T(x_k) f_k(t) \tag{A.2-8a}$$

$$\boldsymbol{\Theta}^T\mathbf{r} - C_p\mathbf{v} = \sum_{j=1}^{N_q} \psi_j(x) q_j(t) \tag{A.2-8b}$$

where modal matrices are

$$\mathbf{M} = \int_{V_s} \rho_s \boldsymbol{\phi}^T(x)\boldsymbol{\phi}(x) dV_s + \int_{V_p} \rho_p \boldsymbol{\phi}^T(x)\boldsymbol{\phi}(x) dV_p \tag{A.2-9a}$$

$$\mathbf{K} = \int_{V_s} E_s \boldsymbol{\phi}''^T(x)\boldsymbol{\phi}''(x) z^2 dV_s + \int_{V_p} c_{11}^E \boldsymbol{\phi}''^T(x)\boldsymbol{\phi}''(x) z^2 dV_p \tag{A.2-9b}$$

$$\boldsymbol{\Theta} = -\int_{V_p} e_{31}(-h_p \boldsymbol{\phi}'')^T(-\nabla \cdot \boldsymbol{\psi}) dV_p \tag{A.2-9c}$$

$$C_p = \int_{V_p} \epsilon_{33}^S(-\nabla \cdot \boldsymbol{\psi})^T(-\nabla \cdot \boldsymbol{\psi}) dV_p \tag{A.2-9d}$$

where h_p is the distance from the centroid of the piezoelectric layer to the neutral axis. It is worth of recognizing that the derivative of right hand side term in Eq. (A.2-8b) with respective to time yields the output current i (duToit *et al.*, 2005).

It is assumed that the electrical field E is constant in the piezoelectric layer which is produced by the following linear potential distribution function:

$$\psi_1 = \frac{z - d_p}{t_p} \tag{A.2-10}$$

where t_p is the thickness of the piezoelectric layer and d_p is the distance from the origin of *z*-axis , which is located at the neutral axis, to the interface of the substrate and the piezoelectric layer. Since $\boldsymbol{\psi} = [\psi_1]$, the electrical coordinate vector **v**(*t*) becomes the output voltage *v*(*t*).

Considering the forcing vector of Eq. (3-19), mechanical damping of (3-20), and Eq. (A.2-10), the governing equations for the piezoelectric vibration energy harvester can be completed as

$$\mathbf{M}\ddot{\mathbf{r}} + \mathbf{C}\dot{\mathbf{r}} + \mathbf{K}\mathbf{r} + \boldsymbol{\Theta}v = \mathbf{F} \tag{A.2-11a}$$

$$\boldsymbol{\Theta}^T\dot{\mathbf{r}} - C_p\dot{v} = i \tag{A.2-11b}$$

where

$$\boldsymbol{\Theta} = -d_{31}c_{11}^E bh_p \int_0^l \boldsymbol{\phi}''^T(x)dx \tag{A.2-12a}$$

$$C_p = \frac{\epsilon_{33}^S A_p}{t_P} \tag{A.2-12b}$$

in which A_p is the outer surface of the piezoelectric layer, *b* is the width of the beam. Because d_{31} contains a negative sign, the coupling coefficient vector $\boldsymbol{\Theta}$ is positive.

According to Figure 3.4, the coupling term $\boldsymbol{\Theta}$ in Eq. (A.2-11) converts input across variable **F** to output across variable *v* and input through variables $\dot{\mathbf{r}}$ into output through variable *i*; so it resembles an electromechanical transformer. This fact is the major difference between piezoelectric and MsM vibration energy harvesters. It is evident that Eq. (A.2-12b) indicates an equivalent capacitance of the piezoelectric layer. Thus from the electrical current equation, Eq. (A.2-11b), the equivalent circuit model of the

piezoelectric harvester can be established as an electrical-mechanical transformer **Θ** in parallel with a capacitor C_p as shown in Figure A.2.

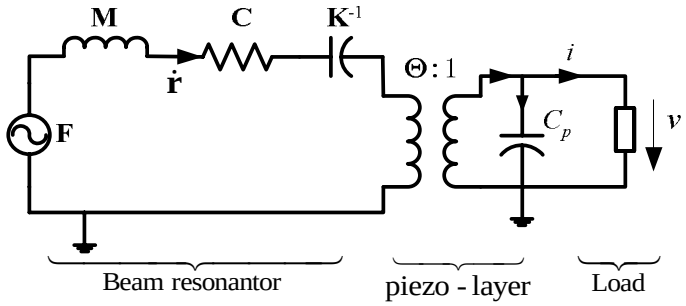

Figure A.2 Equivalent circuit model of the piezoelectric harvester

A.3 List of Publications at NCSU

Journal articles

[1] Wang, L., Yuan, F.G., Active damage localization technique based on energy propagation of Lamb waves. *Smart Structures and Systems* 3(2):201-217, 2007.

[2] Wang, L., Yuan, F.G., Group velocity and characteristic wave curves of Lamb waves in composites: modeling and experiments. *Composites Science and Technology* 67(7-8):1370-1384, 2007.

[3] Wang, L., Yuan, F.G., Damage identification in a composite plate using prestack reverse-time migration technique. *Structural Health Monitoring* 4(3):195-211, 2005.

Conference papers

[4] Wang, L., Yuan, F.G., Vibrational energy harvesting by magnetostrictive material (MsM) for powering wireless sensors. *Proceedings of the 6th International Workshop on Structural Health Monitoring*, Stanford, CA. Sep 11-13, 2007.

[5] Liu, S., Wang, L., and Yuan, F. G. Wireless Sensor Powered by MsM Energy Harvester. *The Word Forum on Smart Materials and Smart Structures Technology*, Chongqing & Nanjing, May 22-27 2007.

[6] Wang, L., Yuan, F.G., Energy harvesting by magnetostrictive material (MsM) for powering wireless sensors in SHM. *Proceedings of SPIE* 6529: 652941, 2007. [Best Student Paper Award]

[7] Wang, L., Yuan, F.G., Lamb wave propagation in composite laminates using a higher-order plate theory. *Proceedings of SPIE* 6531: 65310I, 2007.

[8] Wang, L., Yuan, F.G., Structural vibration energy harvesting by magnetostrictive materials (MsM). *Proceeding of the 4th China-Japan-US Symposium on Structural Control and Monitoring*, Hangzhou, China, Oct.16-17 2006. [Invited Paper]

[9] Wang, L., Yuan, F.G., Experimental study of Lamb wave propagation in composite laminates. *Proceedings of SPIE* 6174:617442, 2006.

[10] Wang, L., Yuan, F.G., Active damage localization in a plate using least-squares method and Lamb waves. *Proceedings of the International Workshop on Integrated Life-Cycle Management of Infrastructures*. Hong Kong, Dec 9-11 2004.

[11] Wang, L., Yuan, F.G., Imaging of multiple damages in a composite plate by prestack reverse-time migration technique. *Proceedings of the 4th International Workshop on Structural Health Monitoring*, Stanford, CA. Sep 15-17, 2003.